Chemical Kinetics for Advanced Combustion Strategies

by

Scott William Wagnon

A dissertation submitted in partial fulfillment
of the requirements for the degree of
Doctor of Philosophy
(Mechanical Engineering)
in the University of Michigan
2014

Doctoral Committee:

Professor Margaret S. Wooldridge
Professor André L. Boehman
Assistant Professor Mirko Gamba
Robert S. Tranter, Argonne National Laboratory
Associate Professor Angela Violi

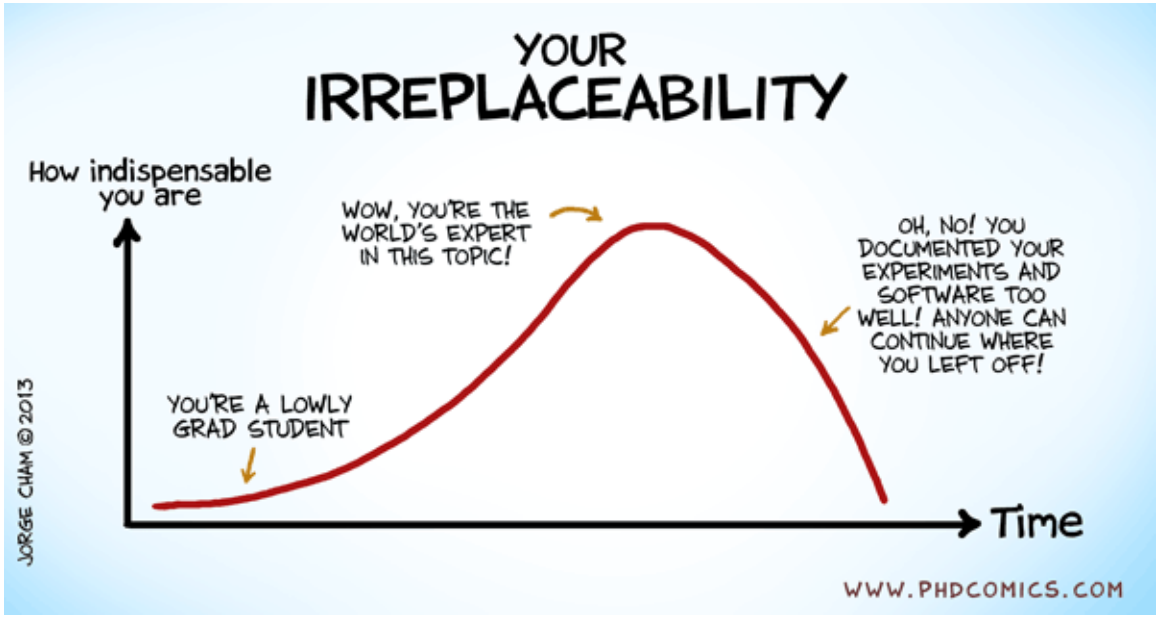

Jorge Cham. Your Irreplaceability. March 20, 2013. Piled Higher and Deeper. Accessed December 6, 2013. <www.phdcomics.com>.

To ideas, moments, and places that inspire and transform us

To the people who fill our journeys with love

Acknowledgements

I am thankful for the encouragement, guidance, and love of the people that have taken this journey with me. My family forms an important foundation for this accomplishment and without them it would certainly have been a more challenging path. To arrive at this point, my insatiable curiosity was nurtured by the sacrifice and wisdom of my parents. My family's love has provided an enormous source of support for which I do not have the words to express my full gratitude, other than to say thank you.

I have been fortunate to meet and maintain three friendships that have weathered the tests of time and distance – Evan Reed, Casey St. Fleur, and Chad Warren. We have shared many experiences as a group in more than a decade together, and this milestone is no different. Thank you for understanding the need to take this journey and I hope the next decade brings us everything we have worked for.

While I am grateful for the roles of many people in my journey over the last five years, my praise for the part Professor Margaret Wooldridge has played is effusive. From providing my first opportunity at Michigan as a graduate student instructor to overseeing this dissertation, Margaret has provided invaluable support and insights. Margaret's open door and discussions on countless topics have fostered an enviable lab group whose quality of research is only matched by the community felt by every member. Thank you Margaret for providing everything I could ask for, and then some, in an advisor.

Thank you to Professor André L. Boehman, Professor Angela Violi, and Professor Mirko Gamba for serving on my committee. Our discussions and your comments are much appreciated in shaping this dissertation.

I would also like to thank two employees of our wonderful National Laboratory network, Dr. Robert S. Tranter and Dr. Charles K. Westbrook. I am indebted to Dr. Tranter for serving on my committee and the use of his laboratory while at Argonne National Laboratory. Dr. Westbrook of Lawrence Livermore National Laboratory for willing shared his extensive knowledge of chemical kinetics in combustion systems and collaboration on many of the studies I participated in, thank you.

You don't embark on the journey that is graduate school without preparation and more than a little forewarning of the challenges ahead (and assurances that there are plenty of great experiences too!). I benefited from building part of my academic and personal foundation at Rowan University with the assistance of Professor Smitesh Bakrania, Professor Krishan Bhatia, Professor Eric Constans, and Professor Paris Von Lockette among others. Professor Bhatia provided engaging lectures that fueled my passion for thermodynamics that, in a way, led me to study combustion. Professor Constans was a constant source of encouragement in preparation and applications for graduate school, thank you for pushing me. I am forever grateful to Professor Von Lockette for my first paid research position, and the relatively large degree of freedom in research that he allowed me. Thank you to Professor Bakrania for his mentoring and his guidance that brought me to Ann Arbor and Margaret.

I have been blessed to call some of the brightest and best people my colleagues, and more importantly friends.

A huge thank you to Dr. Darshan M. A. Karwat – a great friend, colleague, and mentor. I will miss our many hours of NPR/music and the discussions they spawned as we gathered data… when we were not too busy making jokes, at times when they were needed most.

Special recognition is also deserving of Dr. Mohammad Fatouraie, my longtime office neighbor, volleyball cohort, and occasional mind reader. I can't imagine sitting next to a better friend and colleague these past five years.

Thank you to Dimitris Assanis for bringing an unlimited supply of energy, passion, and debate to every day in and out of the lab. I will always appreciate our late night discussions about everything and anything, and still being friends afterwards.

I am grateful to Andrew Mansfield for sharing an apartment and great discussions of sports, politics, and research among many other topics. You're next for a PhD!

I would also like to thank Dr. Christopher J. Annesley, Cesar Barraza-Botet, Eric Bumbalough, Dr. W. Ethan Eagle, Peter Keros, Dr. King (Brian) Y. Lam, Insu Lee, Steven Morris, and Dr. Paul Teini for their friendship and collaboration. Thank you to Anton Rush and Andre Bouldin for being great friends and roommates for much of my time here in Ann Arbor. There are also many others, both academically and personally, that have not made this list and I would like to express my heartfelt gratitude for your role in my journey, thank you!

Table of Contents

List of Figures

List of Tables

List of Appendices

Abstract

Chemical Kinetics for
Advanced Combustion Strategies

by
Scott William Wagnon

Chair: Margaret S. Wooldridge

This dissertation presents new understanding of the role of fuel chemistry on reaction pathways important to fuel oxidation and ignition at conditions relevant to advanced combustion strategies. A deeper and quantitative understanding of fuel chemistry effects on combustion behavior can be used to improve modern combustion strategies that operate at low temperature (<1200 K) conditions using conventional or alternative fuels. A comprehensive understanding of the role of fuel chemistry enables high efficiency and low emissions from combustion technologies.

This work used experimental and computational studies to understand the impact of fuel chemistry at low temperature conditions that are the focus of modern combustion systems. Optically accessible facilities, including a rapid compression machine and a shock tube, were used to study global and detailed combustion chemistry of several important fuel compounds. The results of the computational study on buffer gas composition effects on fuel ignition indicated that ignition phasing is sensitive to composition effects at low pressures, high levels of dilution, and temperatures corresponding to non-Arrhenius or multi-stage conditions. The

results of the work on ignition behavior of methyl *trans*-3-hexenoate highlighted uncertainties in unsaturated methyl ester reaction chemistry, namely the R+O_2 reaction rates and products of smaller unsaturated intermediates. The data presented in the phenyl oxidation study are the first laser schlieren measurements of radical oxidation reactions and the results provide a foundation for further studies which quantify important elementary reaction rates and pathways in oxidation systems, such as phenyl+O_2. In the work with the three linear hexene isomers, the length of the alkyl chain was responsible for changes in reactivity, activation energy, and measured differentiation in the formation of stable intermediates at the conditions studied.

The results of these studies quantify the reactivity of important fuel compounds, which is particularly vital as fuel feed stocks change and the low temperature operating conditions of modern combustion systems become more reaction limited. The results also inform theory on reaction rate rules for elementary reactions and guide the development of detailed, global, and skeletal reaction mechanisms at low temperatures.

Chapter 1
Introduction

Energy utilization across the globe stemming from combustible fuels, primarily fossil fuels (petroleum, coal, and natural gas), has risen demonstrably over the last century and is widely projected to continue increasing [1,2]. In addition to being a significant means of energy conversion, combustion has been a driver of increased local and global levels of compounds (e.g., carbon dioxide, oxides – nitrous and sulfuric, particulate matter) which are often regulated [3,4]. Regulations have been in part motivated by increased awareness of studies that have shown the economic, health, environmental, and societal benefits to reduced consumption and more efficient use of our combustible fuels [5,6,7]. Fundamental and applied studies of combustion continue to significantly influence energy policy decisions made by societies worldwide.

Efforts to increase efficiencies and reduce emissions associated with combustion processes in compliance with regulation have focused on implementing both advanced combustion strategies and alternative fuels. Advanced combustion strategies seek to achieve similar, or better, performance while reducing fuel consumption and emissions regardless of the specific fuel. Proposed advanced combustion strategies include plasma assisted ignition, direct injection (DI), exhaust gas recirculation (EGR), and various types of compression ignition (e.g., homogeneous charge compression ignition and reactivity controlled compression ignition) among others [8,9]. Common features of many advanced combustion strategies include operation at fuel lean equivalence ratios, pre-mixed reactants, high levels of dilution (molar buffer gas to oxygen ratios > 3.76), high pressures (> ~10 atm), and low temperatures (< ~1000 K). There are numerous mechanisms for

these methods to affect combustion behavior including fluidic interactions, heat and mass transfer, and chemical pathways. Often, an advance combustion strategy will affect multiple fundamental parameters and it is vital to understand which of these factors dominate the combustion performance and emissions.

Alternatives to fossil fuels include hydrogen, alcohols (e.g., methanol, ethanol, and butanol), and biofuels (e.g., vegetable oils) among many others. Alternative fuels are cited for their promise to achieve carbon neutral (or negative) lifecycles, in addition to potentially providing similar energy densities and physical properties to current fuels [10,11,12]. Global growth of alternative fuel production is projected to increase from 1.6 million barrels per day to 4.6 million barrels per day over the next 30 years [2]. Alternative fuels can possess vastly different structures to the fuels currently in use, including various degrees of oxygenation, unsaturation, and substitution [10,11,12]. Given the numerous alternative fuel choices, a deeper understanding of combustion chemistry pathways is required to optimize combustion strategies to achieve efficiency and emissions targets.

Combustion chemistry pathways can vary significantly based on the composition and structure of proposed fuels [10,11,12]. An example of the substantial difference between pathways can be seen in fuels exhibiting non-Arrhenius behavior versus those that do not, particularly at conditions relevant to advanced combustion strategies [13,14]. This thesis seeks to understand the role of fuel chemistry on reaction pathways at conditions relevant to advanced combustion strategies. Optically accessible facilities including a rapid compression machine and a shock tube were utilized in the technical approach to study global (e.g., ignition delay times) and detailed (e.g., stable intermediates, reaction rates) combustion chemistry of several important fuel compounds. Experimental facilities and equipment used in this work are described in detail in Chapter 2. The intersection of advanced combustion strategies, fuel structures, and combustion chemistry are discussed and the approaches taken to understand the corresponding combustion chemistry are presented in this document for each of the fuel compounds studied.

The first study undertaken in this work examined the effects of buffer gas composition, such as in EGR, on fuel ignition. Dilution strategies are important tools to achieve high efficiency, low pollutant emissions combustion. There are multiple mechanisms by which EGR can improve combustion performance, including direct cooling or heating, dilution, and potential chemical kinetic interactions through three-body reactions and through trace reactive components in the EGR gases, to name a few. The chemical kinetic and thermal effects of EGR are important as they play significant roles on reaction rates and thereby affect autoignition times and heat release rates. Moreover, thermal, dilution, and chemical kinetic effects are often convolved. For example, thermal effects of buffer gas composition include changes in the specific heat capacity of the fuel/air mixture which affect compression heating and heat transfer losses, and thereby impact chemical reaction rates. Dilution impacts reaction rates (chemical kinetic effects) and heat transfer rates (thermal effects). Chemical kinetic effects also include the impact of third-body collision efficiencies. It is challenging to isolate the effects of EGR composition in internal combustion engine (ICE) studies due to the complexities of the combustion systems and the often limited access for engine diagnostics. Despite these challenges, there have been valuable experimental and computational ICE studies that have investigated some of the thermal and chemical kinetic effects of buffer gases on autoignition, or combustion phasing, and exhaust gas emissions [15,16,17,18,19].

Previous studies have highlighted the value of identifying conditions that are most and least sensitive to buffer gas composition and the mechanisms causing such sensitivity [20,21,22,23]. Isolating, in as much as possible, the chemical kinetic and thermal effects of buffer gas composition on fuel ignition characteristics helps interpret previous results as well as guide future efforts to leverage buffer gas composition as a combustion design tool. The objective of the buffer gas study was to quantify specific chemical kinetic and thermal effects of buffer gas composition using reaction mechanisms that have been well validated and are widely accepted for representing the autoignition chemistry of three important fuels (*iso*-octane, *n*-

heptane, *n*-butanol). Results from the buffer gas study are presented Wagnon and Wooldridge [24] and Chapter 3 of this thesis.

With rising demand for renewable energy, there are concerted efforts to transition to alternative fuels that can deliver higher efficiencies and lower emissions. Biodiesels are promising alternatives to petroleum derived fuels, particularly if they can be economically produced from feed stocks that do not compete with food crops. While much has been learned about the combustion properties of hydrocarbon fuels, much less is known on the combustion chemistry of oxygenated hydrocarbons like the methyl and ethyl esters that are the primary components of biodiesel fuels. The esters in biodiesel fuels are long chain typically C_{18} species, and the majority, typically over 50%, are unsaturated compounds [25,26,27]. While much has been learned from hydrocarbon studies, the structural features of chain length and degree of saturation are not as well understood for esters. Early studies evaluated methyl butanoate and other C_5 esters proposed as the smallest structural unit necessary to represent the chemical kinetics important in biodiesel fuels [28,29,30,31,32,33,34,35,36,37,38,39,40,41,42,43,44,45,46]. These efforts produced key data on reactivity and reaction pathways; however, these works also revealed that longer chain esters are required to accurately represent biodiesel fuel combustion pathways, in particular the negative temperature coefficient behavior observed with real biodiesel fuels [25,47].

Computational and experimental efforts have expanded to evaluate the reaction chemistry of longer chain esters like methyl hexanoate (a saturated C_7) [48], methyl heptanoate (a saturated C_8) [49], methyl decanoate (a saturated C_{11}) [25,50], methyl palmitate (a saturated C_{17}) [51], methyl dec-5-enoate and methyl dec-9-enoate (two unsaturated C_{11} species) [26,52], and methyl oleate (an unsaturated C_{19}) [53]. A recent kinetic model for biodiesel fuels, including both soy and rapeseed methyl ester fuels [54], has pointed to a critical need for better understanding of the kinetics of C=C double bonds that are components of practical biodiesel fuels. Even more recently, Zhang et al. [55] studied the oxidation of methyl *trans*-3-hexenoate/nitrogen mixtures in a jet-stirred reactor at high pressure

(P = 10 atm), for several equivalence ratios (ϕ = 0.6, 1.0, 2.0), and low temperatures (T = 560-1220 K) from which a chemical kinetic mechanism was developed and validated. Zhang et al. [55] concluded lower temperature oxidation was slowed by the presence of the double bond, and higher temperature oxidation resulted in the production of more unsaturated (both mono- and poly-) and oxygenated intermediate species relative to the saturated methyl hexanoate.

Despite this recent progress, there is a clear need for more data and understanding of the effects of ester, allylic, and vinylic structures on combustion kinetics. The work presented in Wagnon et al. [56] and Chapter 4 is the result of an experimental and computational investigation of the autoignition chemistry of methyl *trans*-3-hexenoate (mh3d, $C_7H_{12}O_2$), an unsaturated C_7 ester. The results highlight progress in understanding and remaining uncertainties in unsaturated ester combustion chemistry.

Aromatic oxidation occurs in a wide variety of advanced combustion strategies and fuel types. Regardless of the combustor (e.g., internal combustion engines, burners), injection scheme (e.g., direct, port, swirl), or hydrocarbon based fuel there exists potential for localized fuel rich regions which can promote polycyclic aromatic hydrocarbon pathways (PAH) leading to soot [9] which is a regulated air toxin. Understanding of the pathways involved in PAH formation and oxidation enable more efficient combustor designs and lower emissions. An intermediate that has been commonly investigated is the phenyl radical as it plays a central role in the PAH pathways [57,58,59]. In studying a radical, such as phenyl, it is necessary to generate the targeted species from a stable source, such as phenyl iodide. There have been several studies which have provided valuable insights into the pathways associated with phenyl radicals [60,61], however, few studies have considered the more complex system of phenyl radical oxidation (i.e., phenyl+O_2) at high temperature conditions (>1200 K). Previous work has provided valuable insight and helped the development of the reaction pathways and thermochemistry relevant to the phenyl oxidation system. Frank et al. [62] utilized a shock tube to study phenyl oxidation (i.e., the atomic and molecular oxygen

pathways) via atomic and molecular resonance absorption spectrometry (measuring H, O, I, CO) under high temperature (1000-1500 K) near atmospheric pressure (1.3-2.5 atm) conditions. The cavity ring down technique was employed by Yu et al. [63] in a flow reactor to monitor the formation of $C_6H_5O_2$ from phenyl oxidation by molecular oxygen under low temperature and pressure conditions (T = 297-473 K, P = 20-80 torr). Atomic resonance absorption spectrometry of atomic hydrogen was used in a shock tube by Kumaran et al. [64] to study phenyl oxidation at high temperatures (1068-1403 K) and low pressures (269-421 torr). These studies have provided invaluable information on the reaction rates and branching ratios associated with the phenyl and O_2 reaction.

Elementary reactions have been successfully studied using laser schlieren in pyrolysis experiments conducted in shock tubes [60]. Laser schlieren has also been shown to successfully interrogate the oxidation pathways of a stable species [65]. Cribb et al. [65] utilized laser schlieren to study methanol oxidation (CH_3OH+O_2) at shock heated temperatures (T = 1990-2800 K) and pressures (P = 255-656 torr). A reaction mechanism was developed by Cribb et al. [65] for methanol oxidation and their simulations captured the experimental measurements well. The experimental and computational work of Cribb et al. [65] demonstrate that laser schlieren studies of oxidation reactions are possible if appropriate conditions are met to maintain low levels of exothermicity during measurements. These previous studies provide a basis for the novel application of laser schlieren to the study of radical oxidation elementary reactions.

While these previous studies have provided information on the chemical kinetics of the phenyl oxidation system, questions remain including the influence of secondary reactions and pressure dependence on the phenyl oxidation pathways. Wagnon et al. [66] and Chapter 5 of this thesis present an investigation into the use of the laser schlieren technique for determining reaction rate constants of the phenyl radical oxidation reactions under high temperature (>1200 K) and low pressure conditions (<120 torr). The results highlight the promise and challenges

associated with the application of laser schlieren to radical oxidation in such a complex environment.

Efforts to comply with regulations have benefited from advances in the combustion theory of hydrocarbon fuels. Combustor designs and chemical kinetic models for hydrocarbon fuels (e.g., gasoline, diesel, kerosene, biofuels) are often based on the behavior of surrogate species and their stable intermediates [67,68,69,70]. Alkenes form an important class of species that are critical to accurate predictions of efficiencies and emissions of all hydrocarbon fuels. Historically, studies of alkene features have predominately focused on smaller (< C_5) species, or aromatics (e.g., benzene, toulene) [71,72,73,74,75]. Of larger linear species, investigations have typically concentrated on 1-alkenes (e.g., 1-pentene, 1-hexene, 1-heptene) for their role as stable intermediate species of larger surrogates and real fuels. Previous studies of alkenes have provided invaluable contributions; however, there remain few studies that explore the effect of the double bond position on larger alkenes.

Vanhove et al. [76] completed an experimental study of the linear hexene isomers under stoichiometric, air dilution (buffer gas:O2 = 3.76) conditions, moderate pressures (6.7-8.4 atm), and low temperatures (630-850 K) using a rapid compression machine. The authors concluded that the behavior of the isomers at low temperatures is driven by the position of the double bond, and the double bond position results in competition between the reaction pathways of the component alkyl chains and alkenyl chains. Mehl et al. [77] conducted a computational study of the linear hexene isomers with validation data from Vanhove et al. [76] and 1-hexene data from Yahyaoui et al. [78,79]. Mehl et al. [77] found that at high temperatures internal isomerizations cause the three isomers to produce similar intermediates despite the double bond position. At lower temperatures, Mehl et al. [77] stated that radical additions to the double bond effectively trapped the radicals and prevented low temperature isomerization pathways that increase reactivity. A computational study of the linear hexene and heptene isomers was conducted by Bounaceur et al. [80], and validated against data from Vanhove et al. [76], Yahyaoui

et al. [79], and Tanaka et al. [81]. Bounaceur et al. [80] observed that cis-trans isomers are important in modeling species with a double bond at low temperatures. Alkenes form alkenyl and alkenyl peroxy radicals that can undergo isomerization pathways (involving cis-trans conformations) which can alter reactivity and intermediates according to Bounaceur et al. [80]. Mehl et al. [82] completed an experimental shock tube (ϕ = 1, buffer gas:O2 = 3.7, P = 11 atm, T = 990-1770 K) and computational study of the linear hexene isomers. The authors concluded that at higher temperatures oxidation is driven by initiation and allyl radicals are preferentially formed due to the double bond, while at lower temperatures the length of the alkyl chain determines reactivity.

These previous studies have highlighted the transition in global behavior (i.e. ignition delay time) that occurs in alkenes from low to high temperatures. The study presented in Wagnon and Wooldridge [83] and Chapter 6 provides quantitative understanding of the effects of the double bond at conditions at which this transition occurs and provide new insights into the reaction pathways in the transition region (P = 11 atm, T = 850-1050 K).

The conclusions drawn from the fuel effects on the combustion chemistry of advanced combustion strategies and suggestions for future work are given in Chapter 7.

Chapter 2
Experimental Setup

For the experimental studies presented in this thesis, two facilities were utilized – the University of Michigan rapid compression facility (UM RCF) and the Argonne National Laboratory diaphragmless shock tube (ANL DFST). Ignition delay times and stable intermediate species of fuel surrogates were measured in the UM RCF at low temperature, high pressure state conditions relevant to advanced combustion strategies. Phenyl oxidation reaction rates and pathways were investigated in a novel approach using the ANL DFST and the laser schlieren technique. Brief descriptions and details regarding methodology for the experimental studies are given in this chapter.

2.1 Rapid Compression Facility

Studies on the ignition chemistry of methyl *trans*-3-hexenoate (Chapter 4) and linear hexene isomers (Chapter 6) were performed using the UM RCF

High Speed Imaging

A full description and characterization of the UM RCF can be found in previous literature [84,85,86], and a brief description is provided here. A schematic of the UM RCF is provided in Figure 2-1. The UM RCF can be described in five sections: the driver section, the driven section, the test section, the sabot and nosecone assembly, and the hydraulic globe valve assembly. Mixtures of fuel, oxygen, and buffer gases are prepared manometrically in a dedicated mixing tank with a magnetically driven stirrer. Prepared mixtures are used to fill the evacuated (filled: $<\sim 1.6 \times 10^{-3}$ atm, evacuated: $<\sim 3.3 \times 10^{-4}$ atm) driven section (stainless steel,

2.74 m x 101.2 mm I.D.) after the sabot has been placed adjacent to the globe valve assembly. A sheet of polyester film (< 5.1×10^{-2} mm) is placed between the sabot and globe valve assembly to ensure the integrity of the vacuum and mixture. High pressure air (~10-25 psig) is utilized to fill the driver section and a polycarbonate plate is used to seal the test section while allowing optical access. The sabot (Delrin®) is propelled down the driven section when the globe valve is actuated. During the compression stroke, colder boundary layer gases are trapped via the annular interference fit of the nosecone (ultra high molecular weight polyethylene) and a convergent section that bridges the driven section and the test section. The interference fit also prevents mass transfer from the trapped region and helps stabilize uniform state conditions.

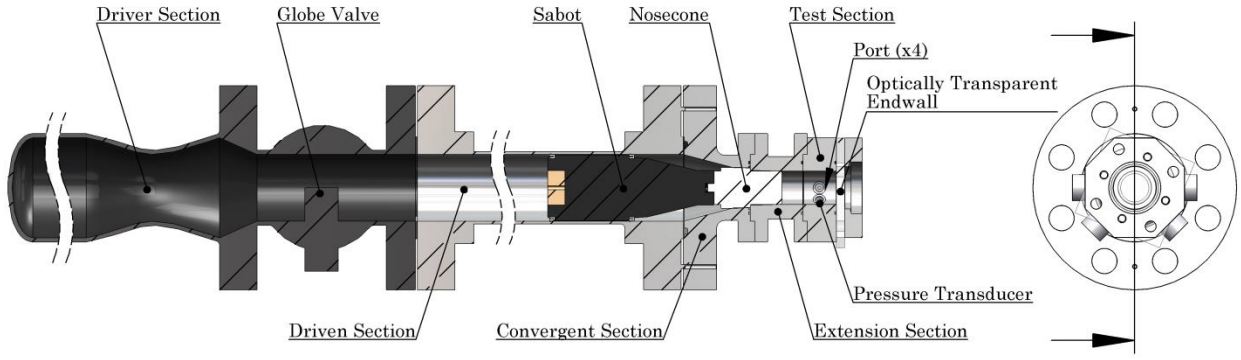

Figure 2-1. Schematic of the UM RCF as configured for high speed imaging.

A piezoelectric transducer (see Chapter 4 and Chapter 6 for details) in series with a charge amplifier (Kistler 5010B) is used to measure the pressure in the test section. Chemiluminescence from ignition is recorded with a high speed digital color camera (see Chapter 4 and Chapter 6 for details). Experiments are recorded with a fixed exposure time of 38 μs and at a rate of 26,000 frames per second. The camera is equipped with a fast 50 mm lens (f/0.95, Navitar) with a c-mount extension tube.

Fast Gas Sampling

A detailed description of the fast gas sampling system and gas chromatography techniques applied in this study are provided in Karwat et al. [86]. As shown in Figure 2-2, for gas sampling experiments, the polycarbonate end plate is replaced with a stainless steel plate to which two independently actuated sampling systems are mounted. Stainless steel tubes extend (10 mm) from the stainless steel plate beyond the cold boundary layer of the test section to sample the reactive mixture. The sampling systems can be described via the following components: a fast sampling valve (Festo MHE3-MS1H-3/26-1/8, stock response 3 ms), a sampling chamber (4.5 ± 0.5 mL), a piezoresistive pressure transducer (Kistler 4045A2) and charge amplifier (Kistler 4618A0), a septum port (VICI Valco, low-bleed), and an isolation valve. The sampling valves are actuated by a trigger signal from a pulse generator (Stanford Research Systems DG535) and have a modified response time of 1.5 ms. Samples are acquired from the higher pressure and temperature test section and quenched upon entering the evacuated sampling chamber. Syringes (Hamilton Gastight #1010, 10 mL) are inserted into the septum port to obtain a gas sample for injection into the gas chromatographs equipped with capillary columns for identifying and quantifying stable intermediates.

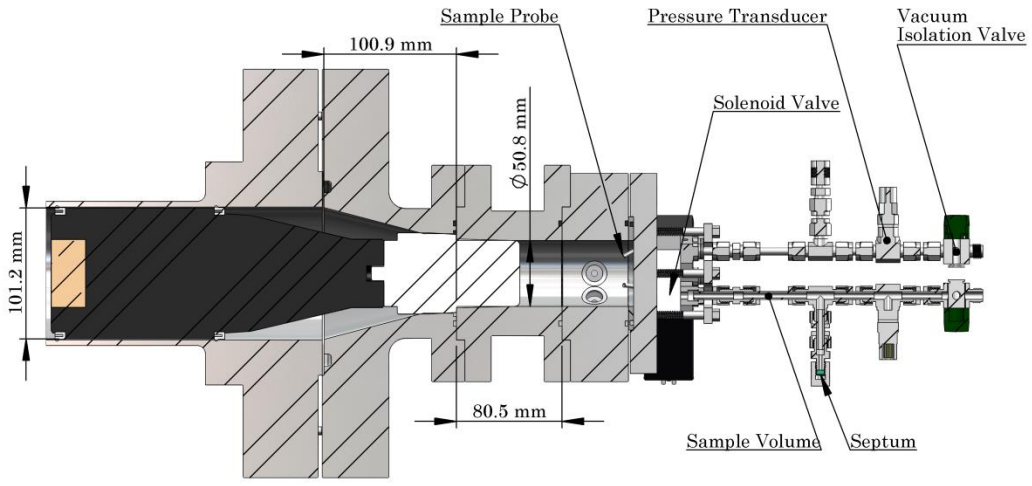

Figure 2-2. Schematic of the UM RCF as configured for fast gas sampling.

2.2 Diaphragmless Shock Tube

The ANL DFST was used for the study presented in Chapter 5 on phenyl oxidation. Full details on the capabilities and characterization of the ANL DFST can be found in Tranter and Giri [87] and Lynch et al. [88]. The ANL DFST consists of three primary parts: the driver section, the driven section, and the fast-acting pneumatic valve. The driver section is composed of a stainless steel tube (58 cm x 22 cm I.D.), and houses the fast-acting pneumatic valve. The fast-acting pneumatic valve consists of a stainless steel bellows connected via a stainless steel rod to an aluminum plate with a circumferential o-ring that seals the driven section from the driver section. A schematic of the bellows is presented in Figure 2-3.

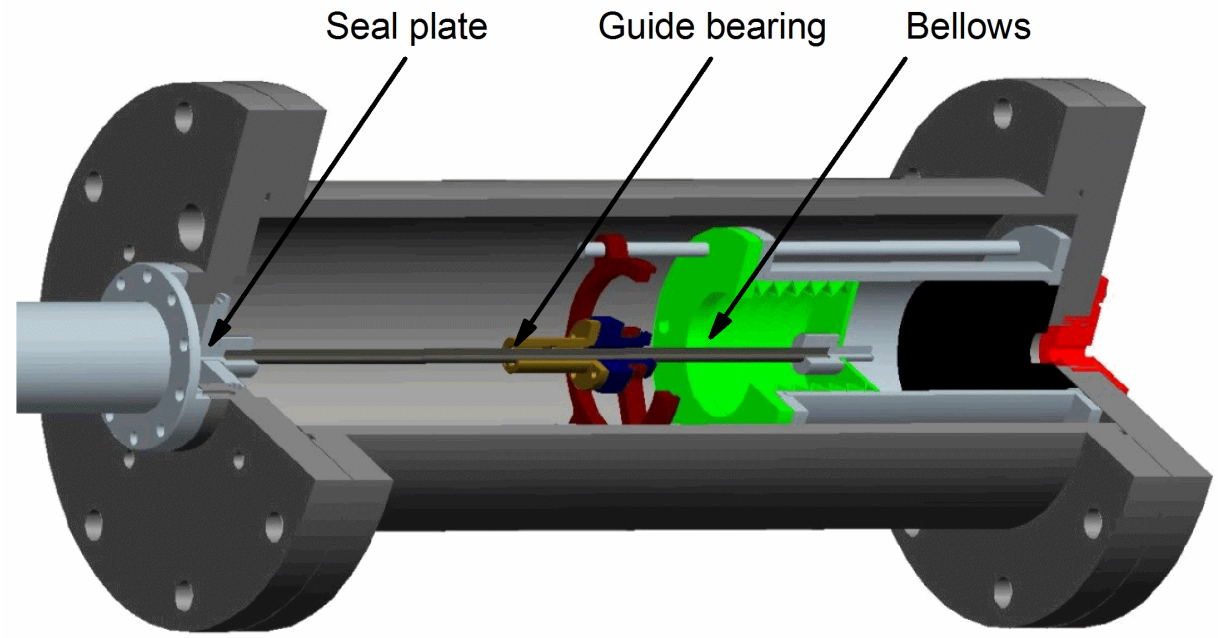

Figure 2-3. Schematic of the ANL DFST fast acting pneumatic valve in the closed position.

The driven section is comprised of a stainless steel tube (6.35 cm I.D.) equipped with optically transparent quarts windows approximately 550 cm from the driver section. The quartz windows are located such that the shock wave has fully developed prior to passing the observation point. Centered on the windows and

spaced 12 cm apart are six pressure transducers (Dynasen piezoelectric) for measurements of the incident shock velocity. Gas phase mixtures are prepared for experiments manometrically in a dedicated glass bulb with a magnetically driven stir bar. Fuel components of mixtures are initially liquid and subjected to several freeze/pump/thaw cycles with liquid nitrogen to ensure removal of impurities and trace components. Experiments are initiated by pressurizing the chamber behind the bellows of the fast-acting pneumatic valve compressing it and forcing the seal plate into the throat of the driven section thereby separating the driven and driver sections. The driver section is then filled with helium to a pressure P_4 and the evacuated driven section is filled with the prepared gas mixture to a pressure P_1. After the driver and driven sections have been pressurized, the bellows are activated releasing the helium into the driven section. A uniform and, due to the diaphragmless nature of the shock tube [87], repeatable shock wave is formed and the desired thermodynamic state conditions are achieved in the driven section. The reaction conditions behind the shock waves are controlled by adjusting P_1 and P_4. One of the benefits of the DFST compared to conventional shock tubes is that the reaction pressure can essentially be fixed while the reaction temperature is varied over a large range with small adjustments to P_1 and P_4.

Laser Schlieren

Laser schlieren is a technique capable of quantifying density gradients over a broad range of thermodynamic conditions, such as those achieved in a shock tube, via deflection of a laser beam in a known medium. In the context of combustion kinetics, density gradient measurements provide valuable information on the progress of a reacting system. The laser schlieren technique has previously been described in detail by Keifer [89,90]. For the experiments in this work, a quadrant photodiode measured the laser (HeNe, <6 mW) deflection across the diameter of the shock tube (i.e., perpendicular to the axis).

A series of reflecting mirrors are used to align the laser to the shock tube and center the beam on the quadrant photodiode prior to deflection. Before each

experiment the photodiode response is recorded as the laser beam is deflected by a rotating mirror at a known angular velocity for a calibration standard. The angular deflection of the laser beam, θ, and photodiode voltage response, V, are linearly proportional for the small deflections observed in shock tube experiments, and the calibration process defines the voltage sensitivity to a change in angular deflection of the laser beam, $dV/d\theta$. The angular deflection during an experiment is then given by Equation 2-1, where G_s is the detector gain and $V(t)$ is the time dependent voltage response of the detector.

$$\theta \propto \frac{V(t)}{G_s}\left(\frac{dV}{d\theta}\right)^{-1} \tag{2-1}$$

The relationship between the measured density gradient, $d\rho/dx$, and the angular deflection is given by Equation 2-2.

$$\frac{dp}{dx} \propto \frac{\theta}{WK_L} \tag{2-2}$$

The measured density gradient in the shock tube is proportional to the angular deflection, the width of the shock tube, W, and the molar refractivity of the mixture, K_L.

Reactions driven by the thermodynamic state conditions achieved by the shock passage, and the incident shock, proportionally affect the measured density gradient. Following the methodology of Kiefer [89], the relationship between the density gradient and the chemical reactions in the shock tube is given by a model that incorporates Equation 2-3 to simulate the system.

$$\frac{d\rho}{dx} \propto \sum_i r_i(\Delta H_i - C_p T \Delta N_i) \tag{2-3}$$

The density gradient is proportional to the rate of reaction, r_i, for reaction i, and the associated heat of reaction, ΔH_i, in an ideal shock wave. Changes in the mole number for corresponding reactions, ΔN_i, are also taken into account with the specific heat capacity, C_p, and the system temperature, T, in Equation 2-3.

Chapter 3
Effects of Buffer Gas Composition on Autoignition

3.1 Objective

Dilution strategies, such as exhaust gas recirculation, alter buffer gas composition and ignition behavior in combustors. Additionally, facilities that investigate the chemical kinetics of combustion often vary buffer gas composition to achieve targeted thermodynamic state conditions. The objective of this study was to identify the conditions at which ignition behavior is sensitive to buffer gas composition using existing mature and experimentally validated reaction mechanisms. Simulated pressure-time histories and ignition delay times were used to quantify the interactions between buffer gas composition, thermodynamic state conditions, and fuel structure on ignition behavior. Results presented in this work highlight the complex interactions between the chemical kinetic and thermal effects of buffer gas composition on ignition behavior. Recommendations are made regarding the interpretation of data measured at conditions that are sensitive to buffer gas composition.

Content of this chapter has been published in *Combustion and Flame* [24].

3.2 Computational Approach

Computational simulations were carried out using the CHEMKIN suite of software (version 10113, x64) [91] and assuming a closed 0-D homogeneous batch reactor at adiabatic, constant volume conditions. Default values from CHEMKIN were used for the solver tolerances and solver time-steps. Detailed chemical kinetic mechanisms were used for each of the fuels, and extensive information on the mechanisms can be found in the literature for *iso*-octane [92], *n*-heptane [86], and *n*-

butanol [93]. Brief summaries of the development and validation of each reaction mechanism used in this study are provided below. The reaction mechanisms were selected due to the maturity and extensive validation that has been previously completed on the reaction chemistry. No modifications to reaction rates were made to the mechanisms considered in this study. The mechanisms do not consider NO_x chemistry. Table 3-1 provides a brief summary of the characteristics of the reaction mechanisms, including the range of conditions for which the mechanisms have been developed and validated.

Table 3-1. Summary of the reaction mechanisms used in this work. Detailed descriptions of the development and validation of the reaction mechanisms can be found in the references listed.

Fuel	# Species	# Reactions	Validation Devices and Conditions[a]	References
i-C_8H_{18}	874	3,796	RCM, ST, JSR, PFR (ϕ = 0.3-1.5, P = 1-45 atm, T = 550-1700 K)	[92,94]
n-C_7H_{16}	1,795	7,245	RCM, ST, JSR, PFR (ϕ = 0.3-1.5, P = 1-50 atm, T = 550-1700 K)	[86,92, 95,96]
n-C_4H_9OH	243	1,446	ST (ϕ = 0.5-2.0, P = 1-8 atm, T = 1100-1800 K) JSR (ϕ = 0.5-2.0, P = 10 atm, T = 750-1100 K)	[93,97,98]

[a] RCM = rapid compression facility, ST = shock tube, JSR = jet stirred reactor, PFR = plug flow reactor

Initial conditions were selected based on relevance to internal combustion engine operating conditions and existing experimental ST and RCM data, particularly the initial pressures. The simulations were conducted at stoichiometric fuel-to-oxygen equivalence ratios (ϕ = 1.0) and over a minimum temperature range of 600-1100 K in 25 K increments for all fuels. Two dilution levels of 3.76:1 and 5.64:1 (buffer gas to O_2 ratios, mole basis) were considered in this study. The dilution levels correspond to air levels of oxygen (or ~21% O_2) and a more dilute mixture with ~15% O_2, mole basis. Argon, nitrogen, carbon dioxide, and water vapor were each evaluated as buffer gases in this study. Devices such as rapid

compression machines and internal combustion engines often use mixtures of buffer gases (e.g., 50% argon/50% nitrogen, or 10% carbon dioxide/15% water/75% nitrogen). In this study, only pure buffer gases (e.g., 100% nitrogen) were considered to isolate and maximize the effects of a particular component on the autoignition behavior. Table 3-2 provides the initial conditions and mixture compositions studied.

Table 3-2. Initial conditions for 0-D homogeneous batch reactor simulations used in CHEMKIN. Composition is provided on a mole basis.

Fuel [-]	Fuel [%]	O_2 [%]	Buffer gas [%]	Φ [-]	Buffer gas:O_2 [-]	P_o [atm]	T_o [K]
i-C_8H_{18}	1.65	20.66	77.69	1.0	3.76	9.0	600-1100[a]
i-C_8H_{18}	1.19	14.88	83.93	1.0	5.64	9.0	600-1100
i-C_8H_{18}	1.19	14.88	83.93	1.0	5.64	60.0	600-1100
n-C_7H_{16}	1.87	20.61	77.52	1.0	3.76	9.0	600-1100[a]
n-C_7H_{16}	1.34	14.90	83.76	1.0	5.62	9.0	600-1100
n-C_7H_{16}	1.34	14.90	83.76	1.0	5.62	60.0	600-1100
n-C_4H_9OH	3.38	20.30	76.32	1.0	3.76	3.2	600-1100[a]
n-C_4H_9OH	2.45	14.71	82.84	1.0	5.63	3.2	600-1100
n-C_4H_9OH	2.45	14.71	82.84	1.0	5.63	60.0	600-1100

[a] Additional high temperature simulations (600-1800 K) were carried out for comparison to experimental data at these conditions.

n-Heptane Mechanism

Simulations of *n*-heptane (the structure is presented in Figure 3-1) autoignition in this study used the reaction mechanism from the *n*-heptane ignition

and speciation study of Karwat et al. [86]. Their *n*-heptane mechanism was largely based on the most recent Lawrence Livermore National Laboratory (LLNL) *n*-heptane chemical kinetic mechanism by Mehl et al. [92], which originates from the work of Curran et al. [95]. The *n*-heptane mechanism from Karwat et al. [86] can be categorized as having 25 distinct reaction classes which describe the low and high temperature chemical kinetic pathways for normal alkanes up to heptane, and a detailed small hydrocarbon (H_2 and C_1-C_4) submechanism updated from the work of Aul et al. [96]. Reaction classes are schemes that allow modelers to assign reaction rates to molecules that have not been studied either theoretically or experimentally based on similar structure. Karwat et al. [86] also modified the low-temperature chemistry (e.g., reactions involving alkylperoxy radicals, RO_2, and hydroperoxyalkyls, QOOH) based on theoretical calculations by Villano et al. [99,100] to improve agreement between model predictions and experimental measurements of heptane intermediates. Karwat et al. [86] found their mechanism produced satisfactory results for their experimental results, in addition to agreeing with the validation targets tested from the Mehl et al. [92] and Curran et al. [95] studies.

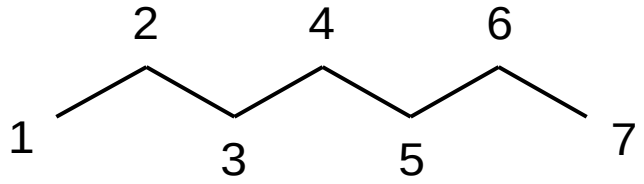

Figure 3-1. Molecular structure of *n*-heptane with carbon atoms numbered from left to right.

iso-Octane Mechanism

Autoignition simulations of *iso*-octane (2,2,4-trimethylpentane, the structure is presented in Figure 3-2) in this study were conducted using the LLNL *iso*-octane chemical kinetic mechanism (Version 3) [92] available online. Version 3 is the most recent available update of the LLNL *iso*-octane mechanism by Curran et al. [94]. Two sets of reaction blocks compose the *iso*-octane mechanism, the first is a chemistry set for hydrocarbons up to C_4. The second is the main reaction set

comprising the same general 25 reaction classes as the *n*-heptane mechanism with rates for branched hydrocarbons up to C_8. The most recent updates to small hydrocarbon chemistry and low-temperature chemistry pathways made to the *n*-heptane mechanism in Karwat et al. [86] are not reflected in the Mehl et al. [92] *iso*-octane mechanism used in this study. Mehl et al. [92] reported satisfactory validation of their *iso*-octane mechanism with recent shock tube, rapid compression machine, and jet stirred reactor data, in addition to the original validation data used by Curran et al. [94].

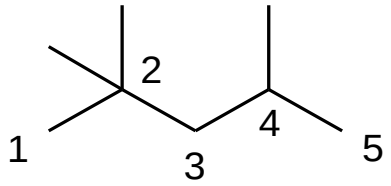

Figure 3-2. Molecular structure of *iso*-octane (2,2,4-trimethylpentane) with the carbon atoms in the linear portion numbered from left to right.

n-Butanol Mechanism

For the *n*-butanol (the structure is presented in Figure 3-3) simulations, the chemical kinetic mechanism by Black et al. [93] was used. Reactions in the Black et al. [93] mechanism consist of a sub-set of reactions for hydrocarbons up to C_4 based on the work of Donato et al. [98] and a sub-set of reactions for *n*-butanol generated using EXGAS and modified to fit the validation data. The authors reported good agreement between the modeled and experimental ignition delay times for lean and stoichiometric mixtures at all pressures investigated. Black et al. [93] found their mechanism was less accurate for rich conditions and indicated that the ratio of unimolecular decomposition to hydrogen atom abstractions may be the cause. Dilution effects (buffer gas:O_2 of 3.6:1 and 26.6:1) on ignition delay times of stoichiometric mixtures at 2.6 atm were also captured well by the authors' mechanism. Experimental species measurements by Dagaut et al. [97] made in their jet-stirred reactor for stoichiometric mixtures at 10 atm were captured reasonably well by the *n*-butanol mechanism, with the largest disagreements

observed for the rate of *n*-butanol consumption, ethyne concentrations, and butanal concentrations.

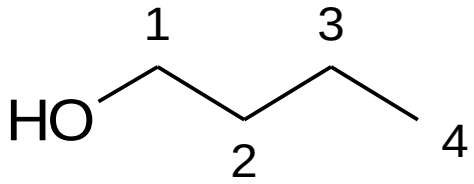

Figure 3-3. Molecular structure of *n*-butanol with the carbon atoms numbered from left to right.

3.3 Results and discussion

Pressure-time histories from the CHEMKIN simulations were used to determine ignition delay times for the *n*-heptane, *iso*-octane, and *n*-butanol mixtures. When single stage ignition occurred, the overall ignition delay time was defined as the time from the start of the simulation to the time corresponding to the maximum rate of pressure rise, dP/dt_{max}, as has been used previously [85,86,101,102,103]. For conditions where two stage ignition occurred, the first stage of ignition was determined from the start time of the simulation to the time of the first maxima in the rate of pressure rise. The overall ignition delay time for two stage ignition was defined as the start time of the simulation to the time of the second maxima in the rate of pressure rise. The temperatures reported for the ignition delay times and pressure-time histories were the initial temperatures of the simulations. Figure 3-4 compares the pressure time histories and corresponding pressure derivatives for the different buffer gases for *n*-heptane at a low temperature (700 K), low pressure (9.0 atm), and dilute mixture condition (where dilution was quantified by the molar ratio of the buffer gas to the O_2 in the mixture). As expected, the final pressures after ignition vary based on the specific heat capacity of the buffer gases. Additionally, the CO_2 results show a slow rate of pressure rise compared to the other buffer gases during ignition.

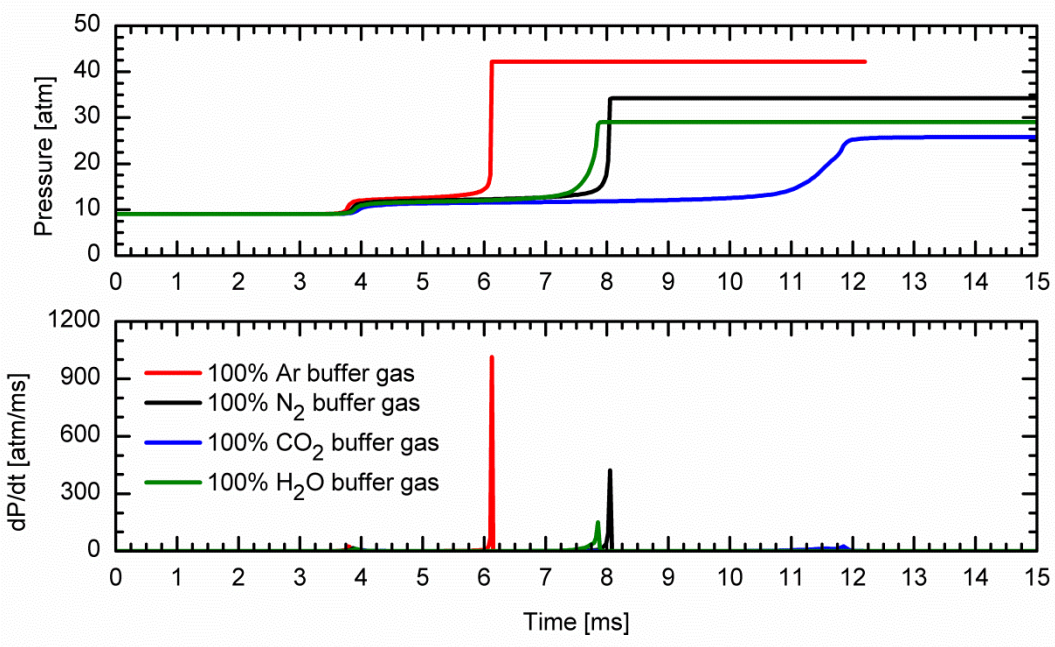

Figure 3-4. Computed pressure-time histories and corresponding derivatives for stoichiometric *n*-heptane mixtures. Initial conditions of 700 K, 9.0 atm, *n*-C_7H_{16} = 1.34%, O_2 = 14.90%, buffer gas = 83.76% (mole basis).

Figure 3-5 shows results for computed first stage ignition delay times (+ symbols) and the overall ignition delay times (solid lines) in an Arrhenius diagram for the case of *n*-heptane at ϕ = 1.0, P = 9.0 atm, buffer gas:O_2 = 5.62, over the temperature range 600-1100 K for the four buffer gases considered. While only the results for *n*-heptane are presented in Figure 3-5, similar trends were observed for *iso*-octane at the same equivalence ratio, pressure, and dilution level. (Please see Appendix A for simulation results not shown in the text. The Arrhenius diagram for *iso*-octane at these conditions is provided as Figure A-4.)

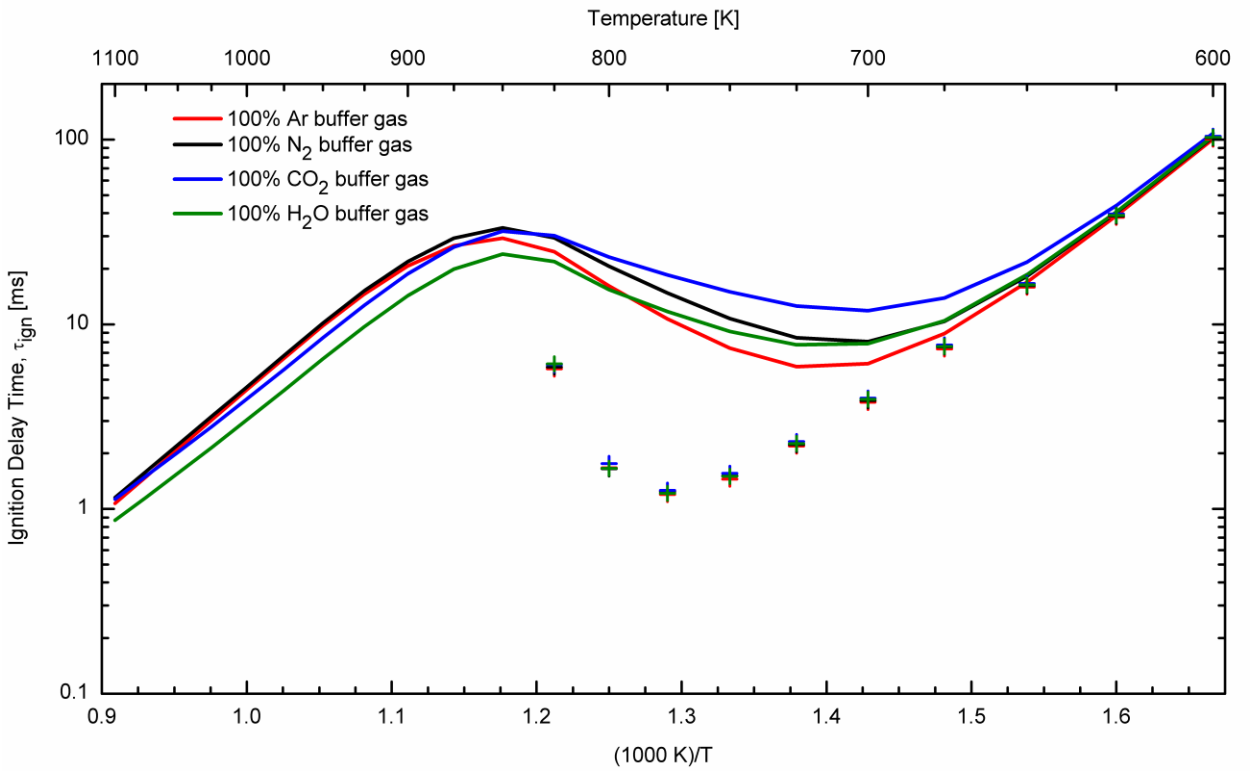

Figure 3-5. Arrhenius diagram for computed ignition delay times of *n*-heptane. For conditions where two stage ignition were observed, the + symbols indicate the computed first stage ignition delay times. Initial conditions of *P* = 9.0 atm, *n*-C_7H_{16} = 1.34%, O_2 = 14.90%, buffer gas = 83.76% (mole basis).

Within the negative temperature coefficient (NTC) region (~650 – 850 K for *n*-heptane, ~600 – 800 K for *iso*-octane), buffer gas composition had significant effect on the overall ignition delay time, with argon and water vapor decreasing overall ignition times up to 31% (30% for *iso*-octane) and carbon dioxide increasing times up to 49% (65% for *iso*-octane) relative to N_2. However, the first stage of ignition shows little variance (< 7% for *n*-heptane, < 16% for *iso*-octane) for any of the buffer gases relative to nitrogen. Outside of the NTC region for both fuels, the buffer gases had less impact on the computed ignition delay times, with water vapor showing the most significant effect in the intermediate temperature chemistry regime, decreasing times up to 37% (34% for *iso*-octane). Rate of production analysis showed that OH and HO_2 radicals from water are not significant reaction pathways at the conditions studied for either PRF, and therefore are not the source of the

decrease in ignition delay times at higher temperatures when water is considered as the buffer gas. Water, and carbon dioxide at higher temperatures (T > ~850 K for *n*-heptane), decrease ignition delay times by their role in three-body reactions (e.g., H_2O_2 decomposition) and the corresponding enhanced collision efficiencies of water and carbon dioxide in such reactions. In the intermediate temperature chemistry regime for *n*-heptane (T > 900 K), argon and carbon dioxide did not alter ignition times more than 17% (15% for *iso*-octane), which is considered reasonably within the uncertainty of the overall reaction mechanisms.

For *n*-butanol at conditions of ϕ = 1.0, P = 3.2 atm, and buffer gas:O_2 = 5.63, there was no NTC behavior over the range of temperatures considered, and the relative reactivity due to the buffer gases was consistent throughout the temperature range. (The Arrhenius diagram for *n*-butanol at these conditions is provided as Figure A-9.) Water vapor and carbon dioxide decreased ignition times up to 52% and 32%, respectively, compared to N_2, and argon increased ignition delay times less than 10% compared to N_2. As with the primary reference fuels, water was not a significant source of radical formation when used as the buffer gas for the conditions studied and the decrease in ignition delay times caused by CO_2 and H_2O is explained by enhanced collision efficiencies.

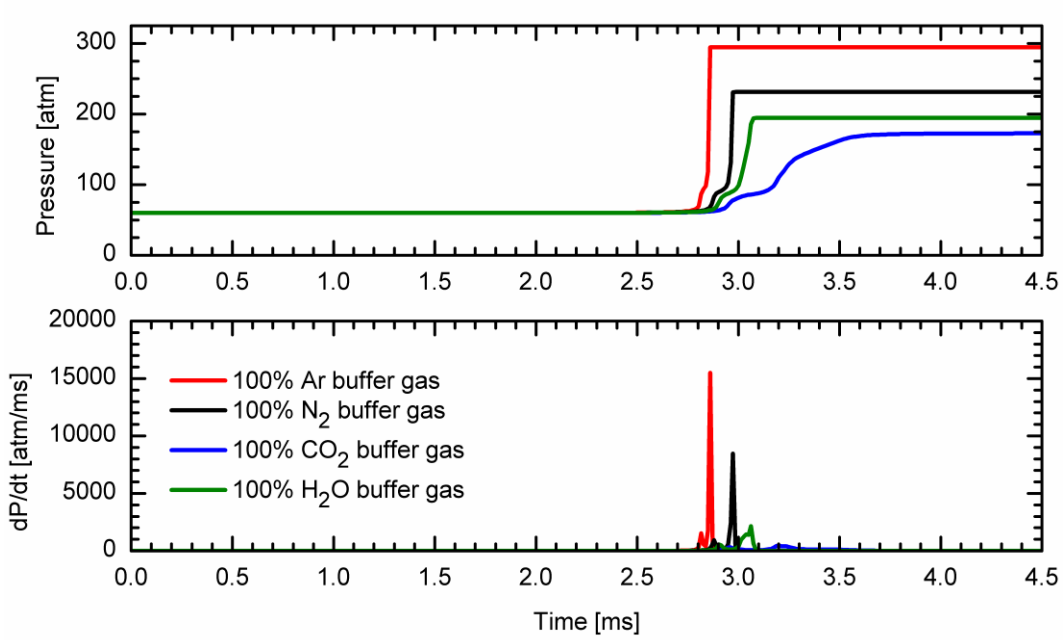

Figure 3-6. Computed pressure-time histories and corresponding pressure derivatives for stoichiometric *n*-heptane mixtures. Initial conditions of *P* = 60.0 atm, *n*-C_7H_{16} = 1.34%, O_2 = 14.90%, buffer gas = 83.76% (mole basis).

Figure 3-6 presents the pressure time histories for the buffer gases at a high pressure condition of 60 atm and 700 K. The duration of the first stage of ignition is considerably reduced for each buffer gas compared to the same temperature and lower pressure conditions of Figure 3-4. The CO_2 continues to exhibit longer times for heat release relative to the other buffer gases. This high pressure condition is near the low temperature limit for the NTC behavior predicted for *n*-heptane, as seen in Figure 3-7. The simulations conducted at high pressure (ϕ = 1.0, 60.0 atm, buffer gas:O_2 = 5.64) show the NTC region shifted to higher temperatures compared to the low pressure simulations (to ~750 – 950 K for *n*-heptane, to ~700 – 900 K for *iso*-octane), and the general trends as a function of buffer gas composition were the same as observed at low pressure. Buffer gas effects on the first stage ignition delay times were negligible (less than 15%) for *n*-heptane and *iso*-octane. Although only two pressures were considered in this study, the results indicate the ignition delay times for the fuels scale by ~P^{-1} on the high temperature side of the NTC region.

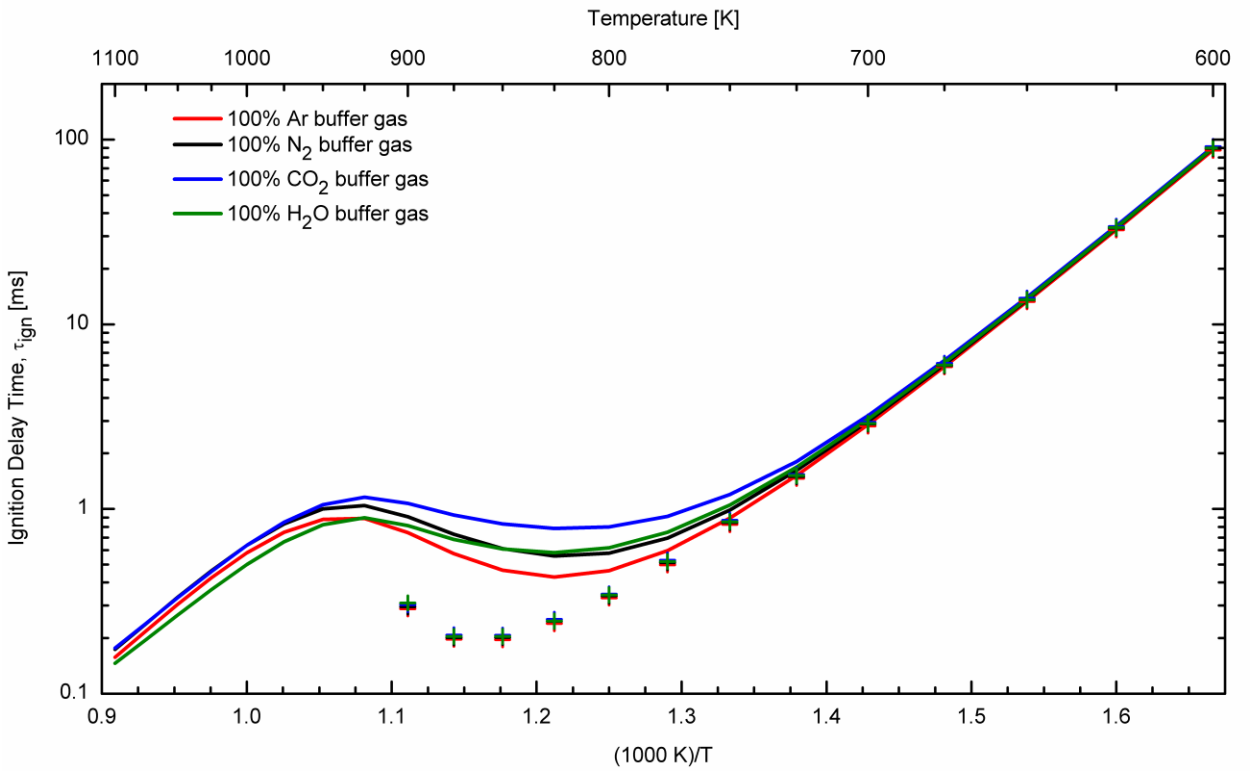

Figure 3-7. Computed ignition delay times for stoichiometric *n*-heptane mixtures at high pressures. For conditions where two stage ignition were observed, the + symbols indicate the computed first stage ignition delay times. Initial conditions of *P* = 60.0 atm, *n*-C_7H_{16} = 1.34%, O_2 = 14.90%, buffer gas = 83.76% (mole basis).

Simulations at the lower level of dilution (3.76 molar ratio of buffer gas to O_2) and the lower pressure (9 atm) revealed similar trends to the higher dilution results as seen in Figure 3-8. The NTC region was shifted slightly (< 25 K) for *n*-heptane and *iso*-octane by decreasing the dilution level from 5.62:1 to 3.76:1. Outside the NTC region, the effects of dilution were approximately proportional, e.g., the 33% decrease in dilution resulted in ~35% decrease in ignition delay times outside of the NTC region for *n*-heptane/nitrogen and *iso*-octane/nitrogen mixtures. Within the NTC region, the decrease in dilution led to ~60% decrease in ignition delay times for the *n*-heptane/nitrogen and *iso*-octane/nitrogen mixtures.

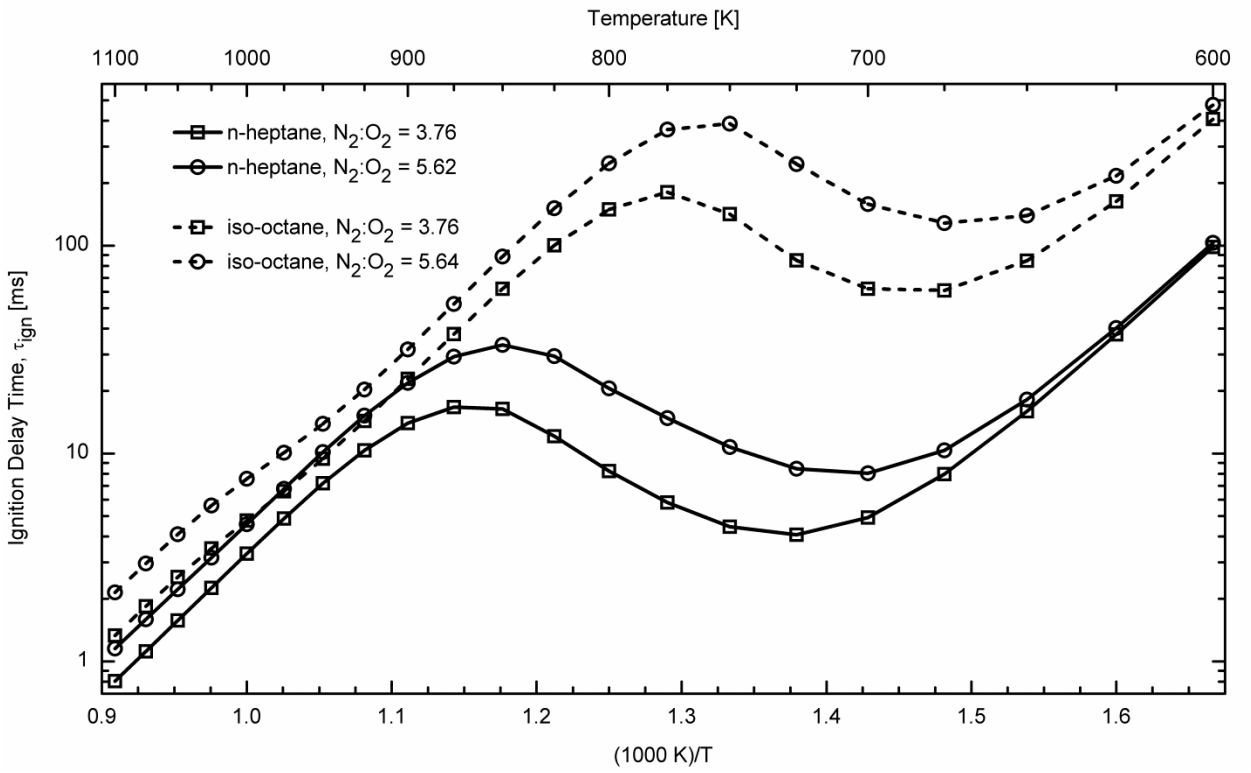

Figure 3-8. Dilution level effects on ignition delay times for stoichiometric mixtures of the primary reference fuels, *iso*-octane and *n*-heptane, at low pressure (*P*=9.0 atm) using N_2 as the buffer gas.

As expected, decreasing the dilution de-amplified the effects of buffer gas composition to the point where changing the buffer gas composition resulted in less than 30% change in the ignition delay time throughout the range of conditions studied for *iso*-octane and *n*-heptane. Lowering the level of dilution for *n*-butanol indicated an approximately proportional impact on ignition delay time (the 33% decrease in dilution yielded a systematic decrease in ignition delay time of ~20%). Air levels of dilution were not considered for the high pressure case (P = 60 atm) for any fuel.

As seen in this study, conditions of lower pressure (< ~10 atm) and higher levels of dilution (buffer gas:O_2 > 3.76) amplify the effects of buffer gas composition, and the NTC region is particularly sensitive to buffer gas composition. NTC behavior is generally attributed to the ratio of reactions forming alkylperoxy radicals (RO_2) to reactions forming alkyl radicals (R). The subsequent isomerization of RO_2 to hydroperoxyalkyl radicals (QOOH), and resulting pathways lead to chain-

branching decomposition. Increases in pressure result in a shift in favor of RO_2 formation as shown by Villano et al. [99], shifting the NTC region to higher temperatures as pressure increases. Increasing pressure also decreases the magnitude of the NTC behavior as observed in the experimental study by Czieki and Adomeit [104]. As dilution decreases, the O_2 concentrations increase also shifting the equilibrium towards RO_2 formation and moving the NTC region to higher temperatures. Comparing Figures 3-5, 3-7, and 3-8, pressure exhibits greater influence than dilution on the NTC behavior for the conditions studied here.

Comparison of Model Trends with Experimental Data

Simulated autoignition times for stoichiometric *n*-butanol mixtures at air levels of dilution and initial pressures of 3.2 atm are compared with existing data from the literature in Figure 3-9. The experimental data shown in the figure are from stoichiometric mixtures and initial temperatures from 678 K < T < 1711 K. The experimental data were obtained for a wide range of pressures and dilution levels, with pressures from 0.9 – 90.3 atm and buffer gas:O_2 ratios from 3.6 - 65.5. Based on the trends observed in this study and in previous work [86,105], all experimental ignition delay times presented in Figure 3-9 were scaled assuming ignition delay times scale inversely with pressure (i.e., as P^{-1}) and proportionally with dilution based on the molar ratio of buffer gas:O_2. All experimental data were scaled to 3.2 atm and buffer gas:O_2 = 3.76. These scaling rules are considered reasonable for data outside the NTC region, with higher uncertainty introduced by scaling within the NTC region.

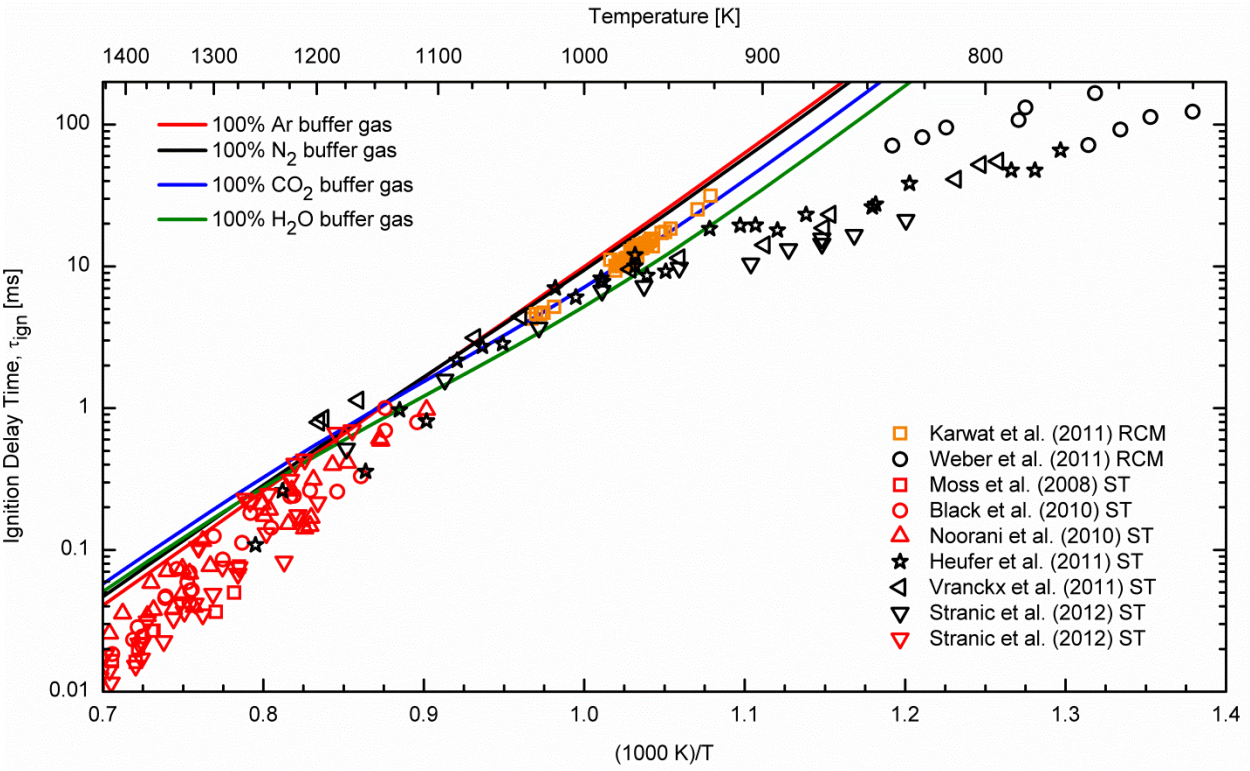

Figure 3-9. Comparison of computed and experimental ignition delay times of stoichiometric mixtures of *n*-butanol at air dilution levels. Simulation results are presented as lines for initial conditions of P = 3.2 atm, *n*-C_4H_9OH = 3.38%, O_2 = 20.30%, buffer gas = 76.32% (mole basis). The symbols are the experimental results and are colored-coded based on the buffer gas composition used: red for argon, black for nitrogen, and orange for mixtures of Ar/N_2 buffer gases. All experimental data have been scaled to P = 3.2 atm and dilution of 3.76:1 (see text for details).

For temperatures above ~1000 K, there is fair agreement amongst the experimental data, within a factor of 3, from all facilities regardless of buffer gas composition. The degree of scatter above 1000 K cannot be attributed to buffer gas effects as the majority of data were acquired with argon. For temperatures below ~900 K, the model predictions deviate from the experimental data. For the long ignition times (>100 ms), this may be due in part because the adiabatic 0-D model is not appropriate for many RCM data. For example, low temperature ignition experiments may be complicated by heat losses as well as weak ignition phenomena, where heat losses typically increase experimental measurements of ignition delay times and weak ignition effects decrease ignition delay times

[106,107,108]. Additionally, the reaction mechanisms used in the study have limited validation targets at low temperatures.

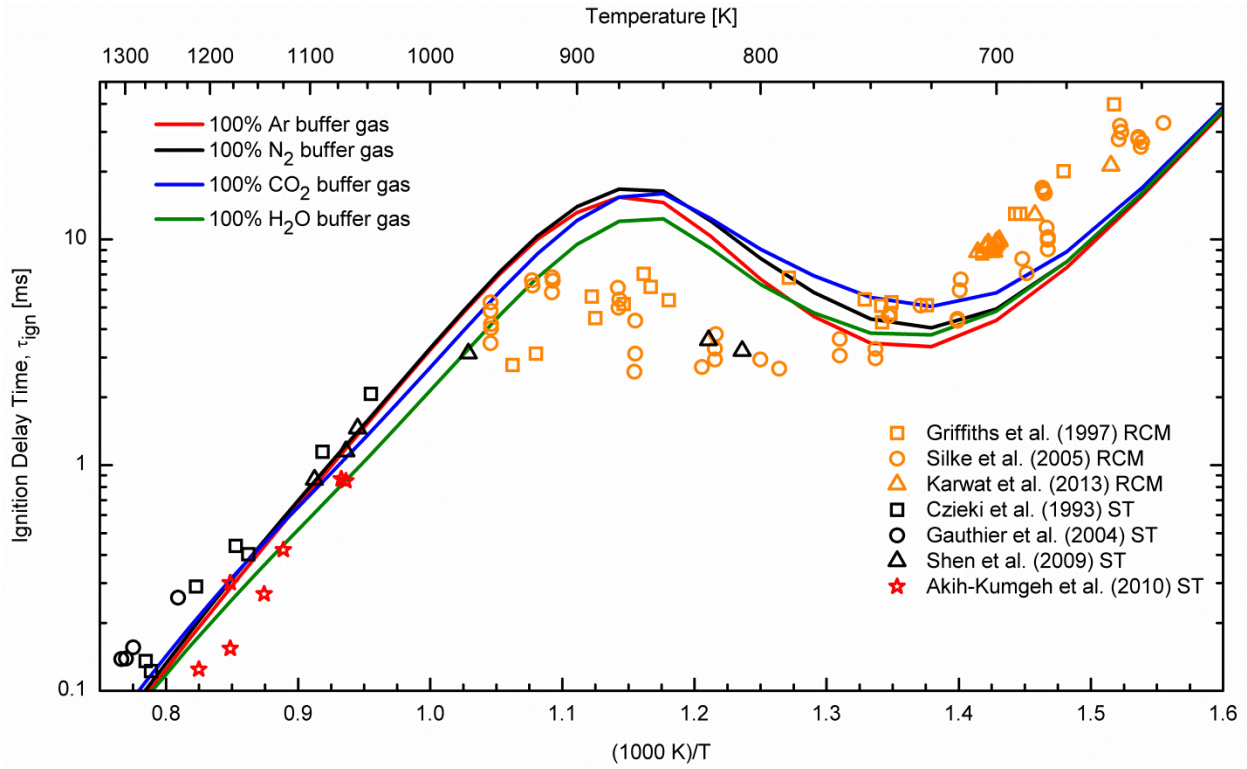

Figure 3-10. Comparison of computed and experimental ignition delay times of stoichiometric mixtures of *n*-heptane at air dilution levels. Simulation results are presented as lines for initial conditions of P = 9.0 atm, *n*-C_7H_{16} = 1.87%, O_2 = 20.61%, buffer gas = 77.52%. Experimental results are presented as symbols and are colored-coded based on buffer gas composition: red for argon, black for nitrogen, and orange for either Ar/N_2 or CO_2/N_2 buffer gases.

The trends between the simulations and experimental data for buffer gas composition are generally consistent. In the temperature range 927-1034 K, Karwat et al. [103] varied argon levels from 15-35% of the buffer gas (with the balance being N_2) for experiments at 3.2 atm and buffer gas:O_2 = 5.63. They observed no changes in autoignition behavior with changes to the buffer gas composition, which is consistent with the model predictions for Ar and N_2. Further, in the limited temperature window where data from different facilities and different buffer gases overlap (~950 K – 1250 K), the results are consistent for argon and

nitrogen as is predicted by the model, albeit the scatter in the experimental data is greater than the effects predicted by changing the buffer gas composition.

Ignition delay times from the *n*-heptane simulations are compared with experimental data at air dilution levels in Figure 3-10. Due to the significant NTC characteristics of *n*-heptane and the effects of pressure on NTC behavior, experiments within a narrow range of pressures (6-12 atm) were used for comparison. The dilution levels considered in the experiments were in the range of 2.48-5.62, molar ratio of buffer gas to O_2. As with the *n*-butanol comparison, the experimental data were scaled inversely with pressure and proportionally with dilution throughout the temperature range considered. The RCM studies used three buffer gases (Ar, N_2, and CO_2) and blends of the buffer gases to vary the end of compression temperatures over the range considered. There is little overlap in the experimental data using different buffer gases. However, at high temperatures (T > 1000 K), the shock tube data using N_2 are systematically slower than the shock tube data using Ar, with larger differences at higher temperatures. This trend extends to higher temperatures not shown on the figure. While the reaction mechanism predicts faster ignition for Ar mixtures compared to N_2, the model predicts only a slight (~5%) decrease in ignition delay time compared to the difference in the experimental data sets (a factor of ~2). Within the NTC region, the scatter in the RCM data is larger than the variation predicted by the model for the range of buffer gases considered, so no conclusions on the effect of buffer gas can be drawn.

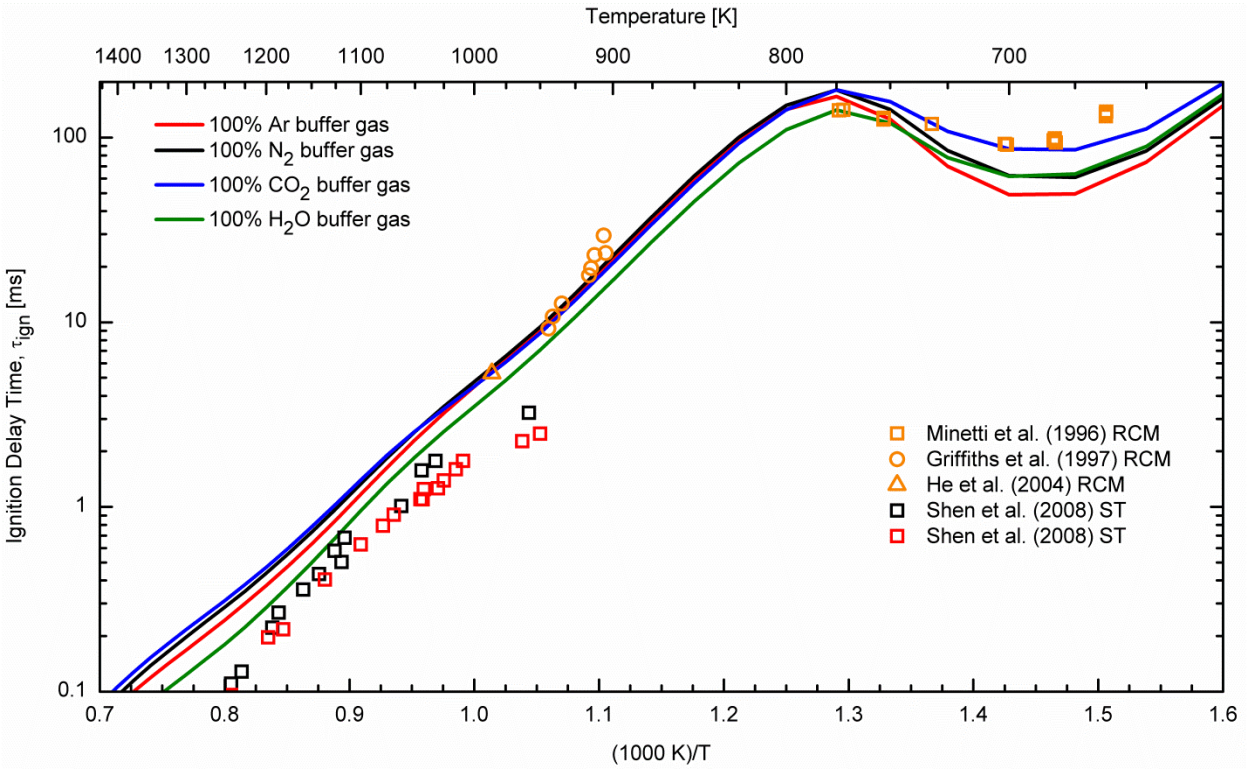

Figure 3-11. Comparison of computed and experimental ignition delay times of stoichiometric mixtures of *iso*-octane at air dilution levels. Simulation results are presented as lines for initial conditions of P = 9.0 atm, *i*-C_8H_{18} = 1.65%, O_2 = 20.66%, buffer gas = 77.69%. Experimental results are colored based on buffer gas composition: red for argon, black for nitrogen, and orange for either Ar/N_2 or CO_2/N_2 buffer gases.

Results of stoichiometric *iso*-octane simulations at air levels of dilution are compared with experimental data in Figure 3-11. The experimental data span a pressure range of 6-12 atm, and have been scaled to 9 atm in the figure using $\tau \alpha P^{-1}$. The experimental data span dilution levels of 2.48 – 5.00 and have been scaled to air levels of dilution using $\tau \alpha$ (buffer gas:O_2). There is a small temperature range (~950 – 1000 K) where there are experimental data using N_2 (black symbols), Ar (red symbols), and N_2/Ar and N_2/CO_2 blends (orange symbols). The trends are consistent with the model predictions, with Ar yielding the fastest ignition and the blends yielding the slowest; however, the reaction mechanism predicts less sensitivity to the buffer gas than observed in the experiments.

Thermal Effects of Buffer Gas Composition

In the mechanisms considered in this study, typical third-body collision efficiencies for carbon dioxide and water vapor are ~2-4 and ~5-12 times that of nitrogen, respectively. The third-body collision efficiencies for argon are typically ~0.3-0.9 that of nitrogen. To isolate the thermal effects of buffer gas composition from the chemical kinetic effects of the collision efficiencies on ignition delay times, simulations were conducted where all the third-body collision efficiencies were set to 1, the collision efficiency of nitrogen. The simulations considered mixtures of ϕ = 1.0 with buffer gas:O_2 = 5.64 and low pressures of 3.2 atm (*n*-butanol) and 9.0 atm (*n*-heptane and *iso*-octane). Results from the simulations are provided in Appendix A. The resulting first stage and overall ignition delay times correlated with expectations based on the specific heat capacity of the buffer gases (i.e., $\tau_{Ar} < \tau_{N2} < \tau_{H2O} < \tau_{CO2}$) for all three fuels, for all temperatures.

Outside of the NTC region, buffer gases without enhanced (or reduced) collision efficiencies relative to N_2 changed the ignition delay by ~±25%. Within the NTC region for *n*-heptane (Figure A-2) and *iso*-octane (Figure A-6), the changes to the collision efficiencies changed the overall ignition delay time by nearly a factor of 2, while the first stage of ignition was virtually unchanged (< 7% for *n*-heptane and < 16% for *iso*-octane). The large difference in the sensitivity to buffer gas composition in the NTC region is attributed to the specific heat capacities of the buffer gases when the collision efficiencies are set to 1. Carbon dioxide and water vapor with higher specific heat capacities than nitrogen exhibit smaller pressure and temperature increases during the first stage of ignition. Since mixtures with carbon dioxide and water vapor are significantly cooler after the first stage compared to nitrogen, the second stage of ignition is demonstrably longer for H_2O and CO_2 when collision efficiencies are set equal to 1. The second stage of ignition is discernibly shorter for argon when compared to nitrogen, due to a higher second stage temperature, when the efficiencies of all the buffer gases are set to 1.

When the recommended collision efficiencies are considered, as in Figure 3-5 and Figure 3-10 for *n*-heptane, the effects of carbon dioxide and water vapor change

from increasing ignition delay times at low temperatures (< 700 K for *n*-heptane) to decreasing ignition delay times (relative to nitrogen) as temperature increases. This effect is observed at both low and high pressures and for both air and dilute mixtures for *iso*-octane and *n*-heptane, and shows how the chemical kinetic and thermal effects are particularly convolved in the NTC region.

Effects of Buffer Gas Composition on Heat Release Rate

As seen in Figure 3-4, buffer gas composition affects heat release rates as well as ignition delay times. The maximum rate of pressure rise (MRPR) correlates with the maximum heat release rate during autoignition, and MRPR is a key metric of engine performance. A characteristic time for heat release, τ_{HR}, can be defined using the MRPR and the overall pressure rise during ignition, P_{max}-P_o:

$$\tau_{HR} = (P_{max}\text{-}P_o)/MRPR$$

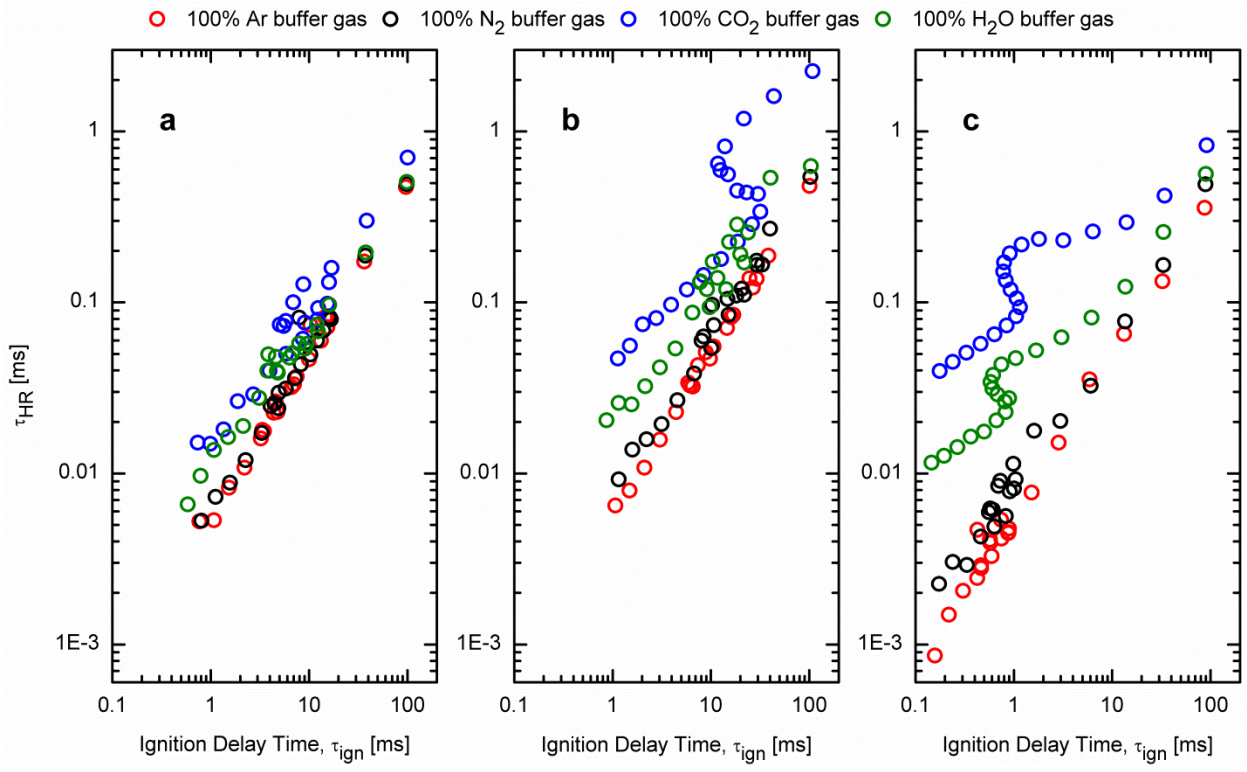

Figure 3-12. Simulation results for characteristic times of heat release as a function of ignition delay time for stoichiometric *n*-heptane mixtures at initial conditions of: (a) P = 9.0 atm, buffer gas:O_2 = 3.76, (b) P = 9.0 atm, buffer gas:O_2 = 5.62, (c) P = 60.0 atm, buffer gas:O_2 = 5.62.

Figure 3-12 shows the relationship between the simulation results for τ_{HR} and ignition delay time for *n*-heptane at ϕ = 1.0 and the dilution levels and pressures considered in this work. Results showing the relationship for τ_{HR} and ignition delay times from *n*-butanol and *iso*-octane simulations are provided in Appendix A. For *n*-heptane at the air levels of dilution and P = 9 atm, the results show characteristic times for heat release correlate linearly with the autoignition times, and the composition of the buffer gas has a larger effect on heat release at faster ignition delay times. The effects of buffer gas composition on heat release are amplified at higher levels of dilution and higher pressures, with over an order of magnitude difference between the characteristic time for heat release for CO_2 and N_2 at P = 60 atm for the same autoignition time. The results indicate that strategies that fix engine autoignition phasing will yield different combustion rates based on the buffer gas composition, and higher engine speeds will be affected more than lower engine speeds. However, while the impact of composition is dramatic at some conditions in Figure 3-12, the concentrations of CO_2 and H_2O in EGR are generally each less than 5% mole fraction, so the effects will be reduced at expected engine levels of dilution.

Sensitivity Analysis

Sensitivity of the ignition delay time and heat release rate results to the third-body collision efficiencies, η, were examined for the three fuels at the stoichiometric, lower pressures of 3.2 atm (*n*-butanol) and 9.0 atm (*n*-heptane and *iso*-octane), and higher level of dilution (buffer gas:O_2 = 5.64) conditions. Third-body collision efficiencies were varied by a factor of 2 from their nominal values, η_o, for this local sensitivity analysis. The factor of 2 was considered a reasonable estimate of the uncertainties of the collision efficiencies. The authors of the *n*-heptane mechanism used a separate reaction, (R20), to represent hydrogen peroxide decomposition with water as a third-body reactant rather than include a third-body collision efficiency for water in (R18). Consequently, the sensitivity results for water were computed by varying the low-pressure A-factor of (R20) by a factor of 2.

The local sensitivity coefficient was defined as the difference between the new and the baseline ignition delay times (i.e., ignition delay times with modified collision efficiencies and the nominal values respectively), normalized by the baseline ignition delay time. Two reactions were found to have significant impact on the predicted ignition delay times and heat release rates:

$$H + O_2(+M) \rightleftharpoons HO_2(+M) \quad \text{(R9)}$$

$$H_2O_2(+M) \rightleftharpoons 2OH(+M) \quad \text{(R18)}$$

All other reactions involving 3rd body collision efficiencies had negligible impact on the calculated ignition delay times.

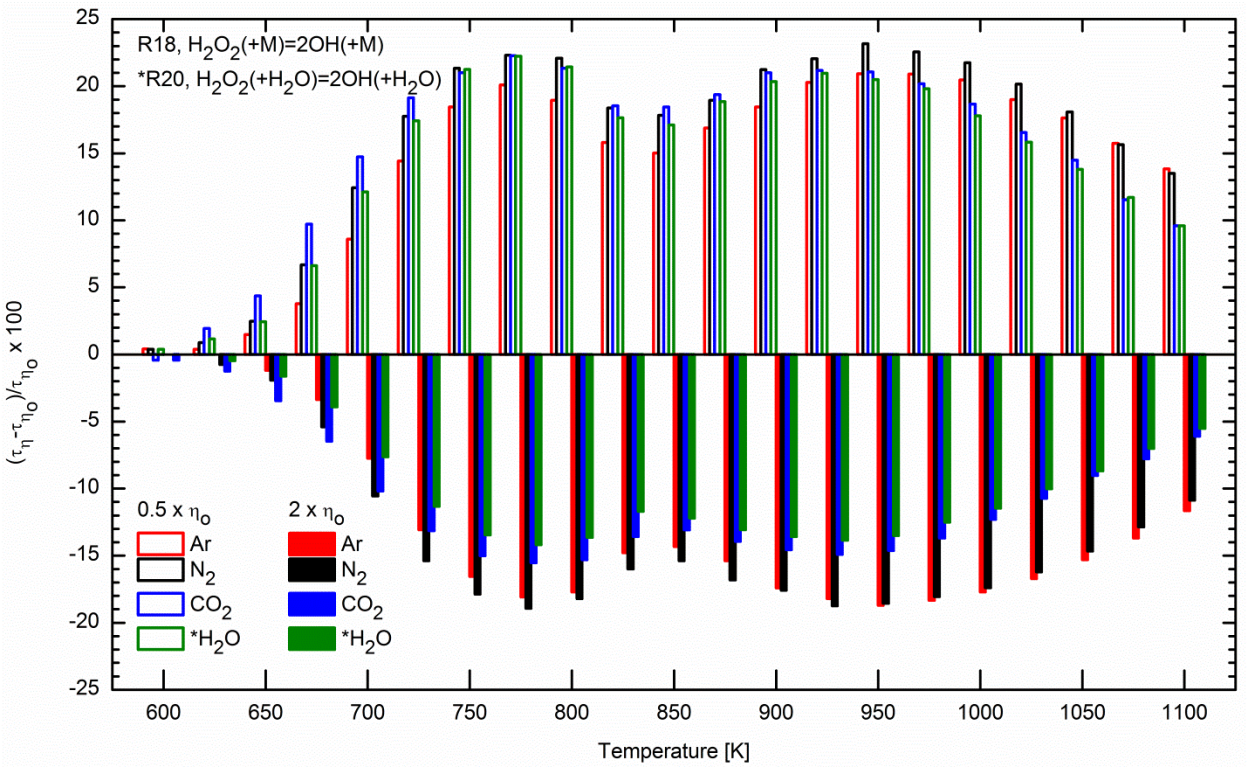

Figure 3-13. Results of the sensitivity analysis of ignition delay time for *n*-heptane to changing the third body collision efficiencies of the reaction (R18) H_2O_2 (+M) = OH + OH (+M) by a factor of 2. The initial conditions of the simulations were P = 9 atm, *n*-C_7H_{16} = 1.34%, O_2 = 14.90%, buffer gas = 83.76%. *The H_2O sensitivity coefficients were determined by changing the A factor for reaction (R20) by a factor of 2. See text for details.

Results of the sensitivity analysis for ignition delay time are presented in Figure 3-13 for *n*-heptane at the conditions of ϕ = 1.0, P = 9.0 atm, buffer gas:O_2 =

5.62. The results show a factor of 2 uncertainty in the values of the collision efficiencies can have as much as a 23% effect on ignition delay time for temperatures ≥750 K. For all fuels, the sensitivities for all the buffer gases remained below 30% for (R18) throughout the entire temperature range at this pressure and dilution level. Sensitivity analysis of (R9) revealed that ignition delays were affected less than 10%/30%/5% for *n*-heptane/*iso*-octane/*n*-butanol respectively at this same initial condition.

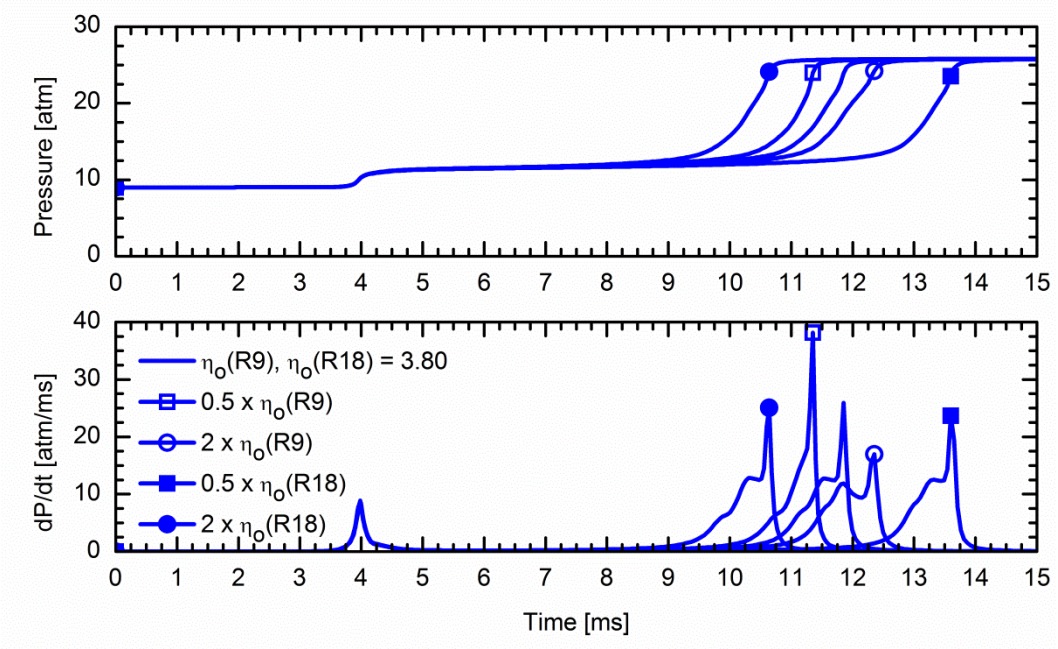

Figure 3-14. Results of changing the collision efficiencies of reactions (R9) and (R18) on pressure and pressure derivative time histories of *n*-heptane at initial conditions of T = 700 K, P = 9.0 atm, *n*-C_7H_{16} = 1.34%, O_2 = 14.90%, CO_2 = 83.76%.

Results of the sensitivity analysis for representative pressure and pressure derivative time histories are shown in Figure 3-14 for T = 700 K for *n*-heptane at ϕ = 1.0, P = 9.0 atm, buffer gas:O_2 = 5.62 and using CO_2 as the buffer gas. The first stage of ignition was unaffected by changes in the collision efficiencies for all fuels and buffer gases. Varying the collision efficiency of (R9) resulted in less than a 5% change of the ignition delay time for the *n*-heptane/carbon dioxide mixture. However, (R9) significantly altered the maximum rate of pressure rise in the second stage of ignition for the *n*-heptane/carbon dioxide mixture, by nearly a factor of two

between the two limiting values of the collision efficiencies. The results for (R18) show while the ignition delay time was affected significantly, the maximum rate of pressure rise was nominally unchanged (< 9%) for *n*-heptane/carbon dioxide. Water vapor showed similar effects to carbon dioxide on the pressure rise rate for *n*-heptane, while argon and nitrogen exhibited little sensitivity (< 14% change). The pressure derivative time histories were less affected (<20% change) by changes in the collision efficiencies for (R9) and (R18) at 700 K for *iso*-octane or *n*-butanol for any of the buffer gases.

3.4 Conclusions

This study improves our understanding of the thermal and chemical kinetic effects of buffer gas composition on the important combustion characteristics of ignition and heat release rate for three reference fuels. Simulations were presented for *n*-heptane, *iso*-octane, and *n*-butanol in stoichiometric mixtures with four buffer gases (Ar, N_2, H_2O, and CO_2) for a range of pressures, dilution levels, and temperatures. Based on the conditions examined in this study, low pressures (<10 atm), high levels of dilution (>1.5× that of air), and negative temperature coefficient conditions are most likely to result in significant thermal and chemical kinetic effects on ignition delay time and heat release rates due to the composition of buffer gases. Fuels that exhibit negative temperature coefficient behavior may show significantly more pronounced buffer gas effects during two stage ignition, with a factor of 2 or more impact on overall ignition times. Caution should be exercised when comparing and compiling data acquired in the NTC region from different experimental facilities that may have used different buffer gases. Ignition data are also subject to uncertainties in the collision efficiencies of the different buffer gases. Experimental data for *n*-heptane at high temperatures indicated a faster ignition for Ar compared to N_2 (on the order of a factor of 2); however, the model simulations predicted much smaller sensitivity to buffer gas composition for *n*-heptane. There are currently few experimental studies which target the effects of buffer gas composition on ignition; particularly studies that vary buffer gas composition using

the same facility. Additional experimental and computational studies will reduce the chemical kinetic uncertainties associated with buffer gas composition, and such work has potential to significantly improve predictive understanding of the complex chemistry and thermal interactions of NTC behavior.

Chapter 4
On the Ignition Chemistry of methyl *trans*-3-hexenoate

4.1 Objective

Many biodiesel fuels are blends of methyl esters which possess structural features, including alkenyl and carboxyl functional groups, which affect combustion behavior in ways that are not fully understood. The objective of this study was to experimentally and computationally investigate the chemical kinetics associated with a representative methyl ester ($C_7H_{12}O_2$, methyl *trans*-3-hexenoate, mh3d) in the University of Michigan rapid compression facility at thermodynamic state conditions relevant to advanced combustion strategies. High speed imaging was coupled with pressure-time histories to measure global chemical kinetic metrics such as ignition delay times. Fast gas sampling and gas chromatography techniques were applied to identify and quantify stable intermediates formed during the ignition experiments. A reaction mechanism for mh3d was developed and validated with measurements from the current work. An ignition delay time regression is presented and the measured stable intermediates highlight uncertainties associated with unsaturated small hydrocarbon chemistry.

Content in this chapter has been submitted for review and publication to *Fuel* [56].

4.2 Experimental Approach

Ignition delay and speciation experiments were conducted in this work using the University of Michigan rapid compression facility (UM RCF). Details regarding the experimental facility and procedures of this study are provided in section 2.1. The pressure transducer used in the test section of the UM RCF was a Kistler

6041AX4, while the transducers used in the mixing manifold were Varian CeramiCel VCMT12TFA (100 torr and 1000 torr). High speed imaging was taken with a Vision Research Phantom v7.1 camera.

Gas Chromatography

Three GCs (Perkin Elmer Autosystem) and columns allow the stable intermediate species to be identified and quantified. GC-OHC (GC2) uses a flame ionization detector (FID) with a Varian CP-Porabond Q capillary column to target oxygenated species. GC-C5 (GC3) uses a FID with a Varian CP-Al_2O_3/Na_2SO_4 capillary column to target species smaller than C_5. GC-C10 uses a FID with a Restek RTX-1 capillary column to target species smaller than C_{10} and some oxygenated species. Helium was used as the carrier gas in all the GCs. Table 4-1 contains the temperature methods applied for each of the columns used in this study.

Table 4-1. Gas chromatography temperature methods for methyl *trans*-3-hexenoate.

Column	Length	ID	Film	Carrier Gas	T_{column}	Detector	$T_{detector}$
CP-Porabond Q	25 m	0.53 mm	10 µm	Helium	40°C (2 min) → 45°C/min 75°C (8 min) → 45°C/min 120°C (7 min)	FID	300°C
CP-Al_2O_3/Na_2SO_4	25 m	0.53 mm	10 µm	Helium	40°C (4 min) → 45°C/min 75°C (13 min)	FID	300°C
RTX-1	60 m	0.32 mm	1 µm	Helium	40°C (8 min) → 45°C/min 75°C (6 min) → 45°C/min 120°C (3 min)	FID	300°C

High-purity gases were used to calibrate for methane (CH_4, Cryogenic Gases, chemically pure, 99%), ethyne (C_2H_2, Praxair, dissolved), ethane (C_2H_6, Cryogenic Gases, chemically pure, 99.0%), ethene (C_2H_4, Matheson, chemically pure, 99.5%),

propane (C_3H_8, Cyrogenic Gases, instrument grade, 99.5%), propene (C_3H_6, Cryogenic Gases, polymer grade, 99.5%), and 1-butene (1-C_4H_8, Cyrogenic Gases, 99%). Calibrations were also determined using vapor from liquid methanol (CH_3OH, Sigma Aldrich, ACS spectrophotometric grade, ≥99.9%), ethanal (CH_3CHO, Fluka, puriss. p.a., anhydrous, >99.5% GC grade, ≤0.5% free acid CH_3CHO), ethanol (C_2H_5OH, Sigma Aldrich, 200 proof, anhydrous, ≥99.5%), butanal (*n*-C_4H_7OH, Sigma Aldrich, puriss., ≥99.0%), but-3-en-1-ol (C_4H_7OH, Sigma Aldrich, 96%), and methyl *trans*-3-hexenoate ($C_7H_{12}O_2$, Sigma Aldrich, 98%). Signals from the gas chromatographs were captured using a high-resolution data acquisition system (NI PXI 4472) at a rate of 8 Hz. Species were calibrated and quantified using the area under the response peak unless otherwise noted.

4.3 Reaction Mechanism Development

A reaction mechanism for methyl *trans*-3-hexenoate (mh3d) was developed based on the mechanism of Herbinet et al. [26] for methyl dec-5-enoate. The key features of the mechanism were found to be those portions that describe the effects of the C=C double bond, which is located at the midpoint, or '3' location in the chain of five carbon-carbon bonds in the fuel, which can be described as:

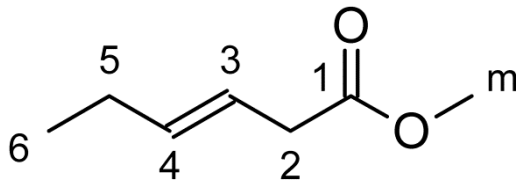

The C atoms are labeled, starting with the C atom in the C=O bond as #1. In contrast with saturated methyl esters, the vinyl C-H bonds (carbon sites #3,4) are very strong and those H atoms are difficult to abstract. The C-H bonds at the C atoms adjacent to the double bond (carbon sites #2,5) are very weak allylic bonds, and these H atoms are preferentially abstracted by reactive radical species during autoignition and oxidation of mh3d. As a result, the dominant alkyl-like radicals produced during mh3d combustion are these allylic radicals.

4.4 Experimental Results

Ignition Delay Time

A typical plot of the test section pressure and pressure derivative from a mh3d autoignition experiment is presented in Figure 4-1. The maximum pressure at the end of compression (EOC) is defined as t = 0 s and labeled P_{max}. The time from the end of compression to the maximum rate of pressure rise is defined as the ignition delay time for the experiment, i.e. the time between P_{max} and dP/dt_{max}. Figure 4-1 also presents typical pressure time histories of a sampling experiment and the corresponding pressure data from one of the sample chambers. During sampling experiments individual trigger pulses are used to actuate the two sampling systems. Frames from the imaging data corresponding to the pressure time history of the non-gas sampling ignition experiment are presented in Figure 4-2. The images show autoignition is volumetric and characterized by blue emission (attributed to C_2 and CH radicals) [86,109]. The maximum intensity of the emission corresponds to the peak in the pressure derivative.

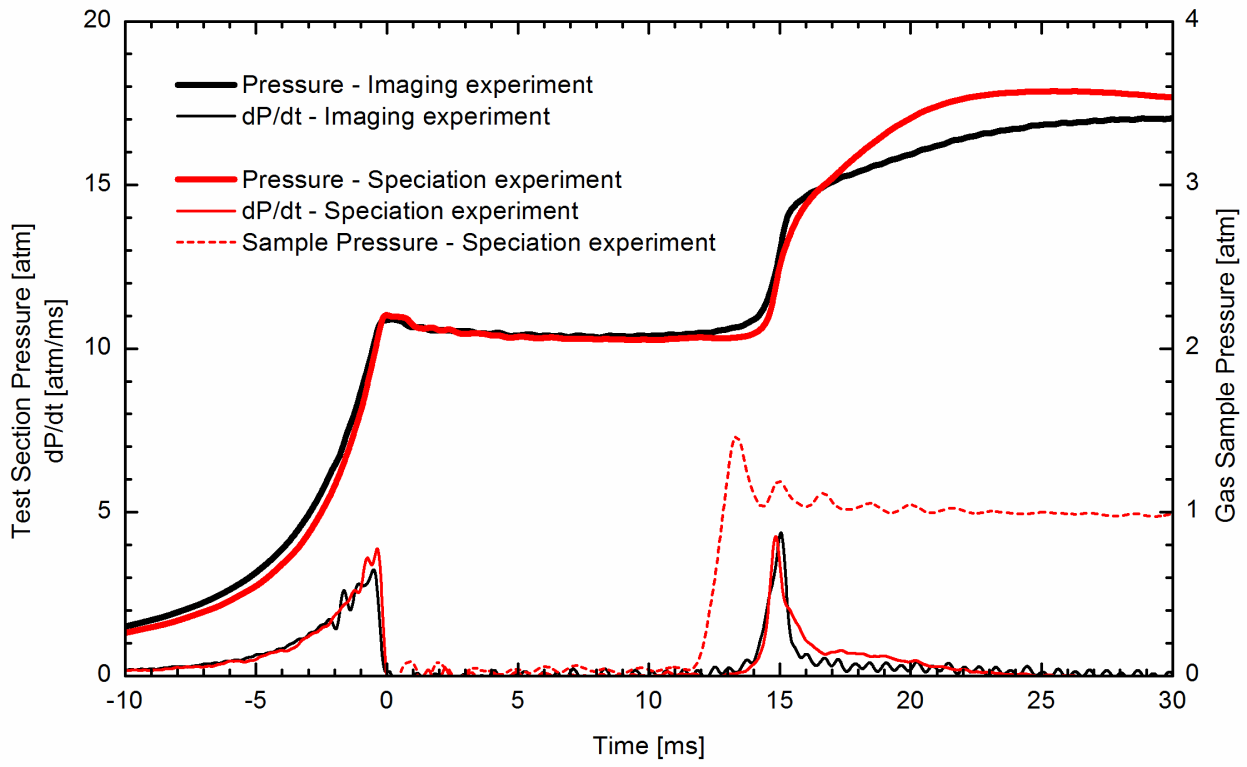

Figure 4-1. Typical results for test section pressure (imaging and speciation experiments), sampling chamber pressure, and pressure derivative time histories. Imaging experiment: P_{eff} = 10.6 atm, T_{eff} = 937 K, ϕ = 0.30, inert:O_2 ratio = 3.76, χ(mh3d) = 0.69%, $\chi(O_2)$ = 20.86%, $\chi(N_2)$ = 73.74%, $\chi(CO_2)$ = 4.70%, τ_{ign} = 15.2 ms. Speciation experiment: P_{eff} = 10.4 atm, T_{eff} = 938 K, ϕ = 0.28, inert:O_2 ratio = 3.77, χ(mh3d) = 0.65%, $\chi(O_2)$ = 20.84%, $\chi(N_2)$ = 76.13%, $\chi(CO_2)$ = 2.37%, τ_{ign} = 14.9 ms, t_{sample} = 11.2 ms.

The effective pressure (P_{eff}) for each experiment is defined as the time-integrated average pressure from the P_{max} to dP/dt_{max}, which captures heat losses from the test section and any exo- or endothermicity prior to ignition. The effective temperature (T_{eff}) for each experiment is determined by numerically integrating the isentropic compression equation and using the known values of P_{eff}, the initial charge pressure, the initial temperature (~295 K), and the temperature dependent ratio of the specific heats of the unreacted test gas mixture, which is determined using the NASA polynomial fits [110] to their thermodynamic properties.

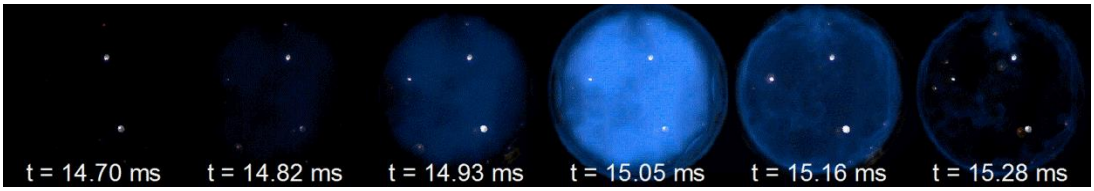

Figure 4-2. Still images corresponding to the speciation experiment in Figure 4-1.

A summary of all experimental conditions and results is presented in Table 4-2. Equivalence ratio (ϕ) is defined as the molar ratio of the fuel to oxygen divided by the stoichiometric ratio of fuel to oxygen. Different inert gases (argon, carbon dioxide, and nitrogen) were used in the study to control (partially) the end of compression conditions via the ratio of the specific heats of the test gas mixture. Experimental conditions were held at a fixed equivalence ratio of ϕ = 0.3 and a fixed inert gas to oxygen ratio of 3.76. P_{eff} targeted 10.5 atm and the data range from 9.5-11.5 atm, and T_{eff} span 884-1085 K.

Table 4-2. Summary of experimental conditions and results for methyl *trans*-3-hexenoate autoignition. All mixture data are provided on a mole fraction basis.

ϕ	Inert:O_2	Test Gas Composition					P_{eff}	T_{eff}	τ_{ign}
		χ(mh3d) [%]	χ(O_2) [%]	χ(N_2) [%]	χ(Ar) [%]	χ(CO_2) [%]	[atm]	[K]	[ms]
0.30	3.76	0.69	20.86	64.06	-	14.38	10.3	884	34.6
0.30	3.76	0.69	20.86	64.05	-	14.39	10.3	885	35.7
0.30	3.76	0.69	20.86	69.05	-	9.39	10.7	914	19.8
0.30	3.76	0.69	20.87	69.07	-	9.37	10.9	919	21.3
0.30	3.76	0.69	20.85	76.05	-	2.40	9.8	924	17.6
0.29	3.72	0.68	21.03	74.94	-	3.34	10.1	925	19.5
0.30	3.76	0.69	20.84	75.04	-	3.42	10.1	926	17.3
0.30	3.76	0.69	20.86	75.11	-	3.33	10.1	927	18.6
0.30	3.76	0.69	20.86	75.12	-	3.32	10.2	928	18.5
0.30	3.76	0.69	20.86	75.09	-	3.36	10.2	929	18.9
0.30	3.77	0.69	20.84	75.95	-	2.52	10.2	931	16.6
0.30	3.76	0.69	20.86	75.10	-	3.34	10.4	932	16.0
0.30	3.76	0.69	20.85	76.03	-	2.43	9.8	933	16.4

0.30	3.77	0.69	20.83	75.09	-	3.38	10.5	934	14.5
0.29	3.76	0.67	20.87	74.99	-	3.46	10.5	935	15.6
0.30	3.76	0.69	20.86	76.05	-	2.40	10.3	935	15.1
0.30	3.76	0.69	20.86	73.74	-	4.70	10.6	937	15.2
0.30	3.76	0.69	20.85	76.05	-	2.40	10.4	938	13.6
0.30	3.78	0.69	20.76	75.21	-	3.33	10.7	939	15.3
0.30	3.77	0.69	20.83	76.05	-	2.43	10.6	939	13.7
0.30	3.76	0.69	20.86	76.05	-	2.40	10.6	941	14.4
0.30	3.76	0.69	20.87	73.75	-	4.69	10.9	945	12.7
0.30	3.76	0.69	20.85	74.12	4.34	-	9.5	964	13.1
0.30	3.77	0.69	20.84	78.09	-	0.38	10.9	972	8.7
0.30	3.76	0.69	20.87	78.13	-	0.30	10.9	972	8.7
0.30	3.76	0.69	20.87	72.96	5.48	-	10.4	983	8.0
0.30	3.76	0.69	20.87	72.69	5.75	-	10.8	994	6.3
0.30	3.76	0.69	20.87	72.68	5.75	-	11.1	1000	5.4
0.29	3.70	0.69	21.13	65.63	12.55	-	10.7	1022	3.9
0.29	3.70	0.69	21.13	65.63	12.54	-	11.0	1028	3.4
0.30	3.76	0.69	20.85	61.73	16.73	-	9.6	1033	3.8
0.30	3.76	0.69	20.85	61.72	16.74	-	11.1	1052	2.4
0.30	3.77	0.69	20.80	61.49	17.02	-	11.3	1058	2.4
0.30	3.77	0.69	20.80	61.50	17.01	-	10.6	1058	2.6
0.30	3.77	0.69	20.80	61.55	16.96	-	10.9	1066	2.2
0.30	3.76	0.70	20.87	58.93	19.51	-	10.9	1067	1.8
0.30	3.76	0.69	20.86	59.50	18.95	-	10.9	1068	2.1
0.30	3.76	0.70	20.87	58.92	19.51	-	11.0	1068	2.0
0.30	3.76	0.69	20.86	57.80	20.64	-	10.9	1080	1.7
0.30	3.76	0.69	20.87	57.77	20.67	-	11.5	1083	1.3
0.30	3.76	0.69	20.87	57.83	20.62	-	11.1	1085	1.4

Regression analysis was used to develop an expression for τ_{ign} [ms] as a function of temperature. An Arrhenius form of the fit equation was used, and the result with $R^2 = 0.99$ is:

$$\tau_{ign} = 1.4 \times 10^{-6} \exp\left[\frac{30100}{\bar{R}_{\left[\frac{cal}{K \cdot mol}\right]} \cdot T}\right] \tag{4-4}$$

A summary of the autoignition data and Equation 4-4 are presented Figure 4-3. The subset of data which correspond to the speciation experiments is highlighted by the inset in Figure 4-3. The autoignition delay measurements are highly repeatable as evidenced by the standard deviation of 0.9 ms or ±6% over the temperature range 930-938 K, where most of the gas-sampling experiments were conducted. The overall uncertainty in the ignition delay time measurements is ±21% which is based on experimental accuracy of the state conditions.

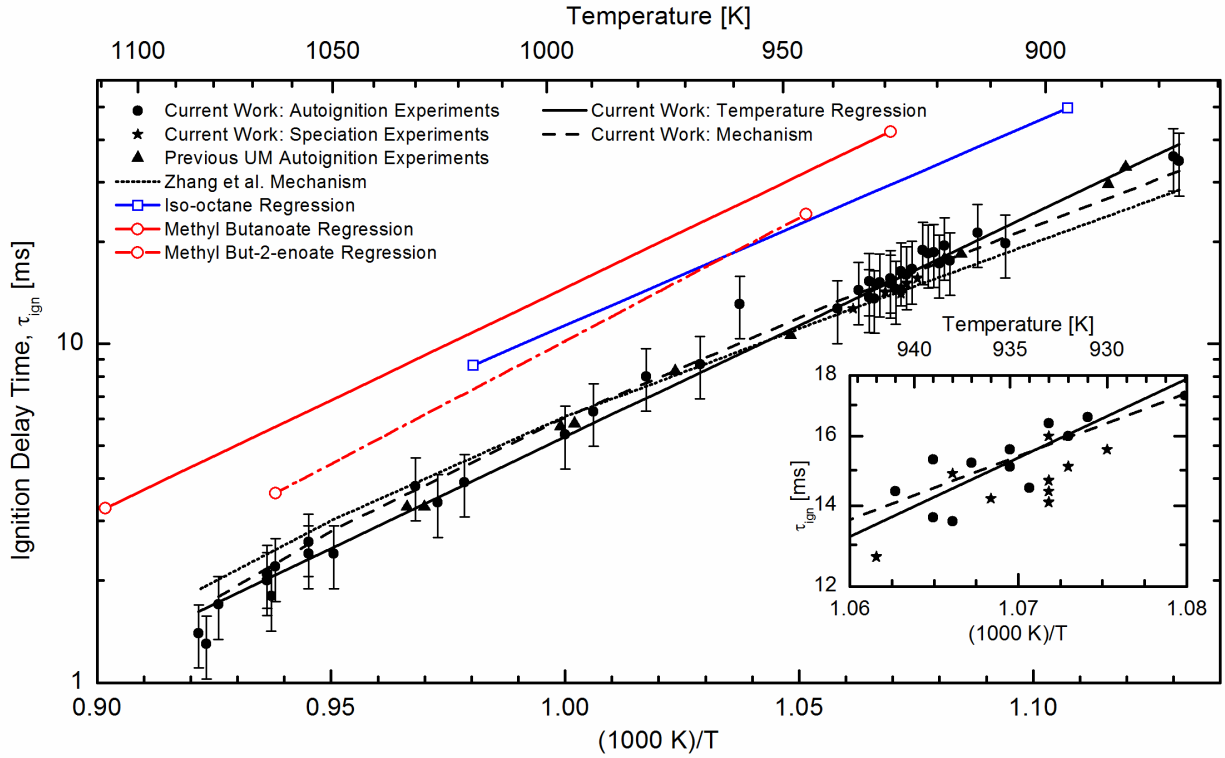

Figure 4-3. Results for experimentally measured methyl *trans*-3-hexenoate ignition delay time and comparison with other fuel ignition characteristics. The mh3d data were acquired at nominal conditions of P = 10.5 atm, ϕ = 0.30 and $\chi(O_2)$ = 20.90%.

The experimental ignition delay time data of mh3d are compared to results of previous autoignition studies of *iso*-octane [85], methyl butanoate [29,46], and methyl but-2-enoate [111] in Figure 4-3. Provided in Table 4-3 are the parameters describing the regression correlations. Regression correlations were used to normalize the previous results to the conditions considered in this study, i.e. P = 10.5 atm, ϕ = 0.3, $\chi(O_2)$ = 20.9%. The data show a clear progression from the least

reactive saturated C_5 ester methyl butanoate, to the unsaturated C_5 ester, to the fastest ignition observed with the unsaturated C_7. The current work supports our understanding of the effects of chain length and the double bond leading to faster ignition chemistry as observed in other studies, including recent work by Wang et al [52]. Negative temperature coefficient behavior is not observed for any of the fuels at these temperatures and pressures.

Table 4-3. Parameters for ignition delay regression correlations from previous autoignition studies of methyl butanoate, methyl but-2-enoate, and methyl butanoate. Regression correlations are in the form of $\tau_{ign} = A \cdot P^b \cdot \phi^c \cdot \chi(O_2)^d \cdot \exp(E_a/RT)$.

Fuel	A [ms]	b	c	d	E_a [cal/mol/K]	Reference
methyl butanoate	3.2e-3	-1.21	-0.77	-1.62	30,300	[29,46]
methyl but-2-enoate	5.6e-7	0	0	0	33,200	[111]
iso-octane	2.8e-3	-1.25	-0.79	-1.14	27,300	[85]

The reaction mechanism developed in this study and the mechanism by Zhang et al. [55] were used with the CHEMKIN software to model a 0-D, adiabatic, constant volume reactor while solving the energy equation at the conditions of the experiments. Inert gas composition was varied in the simulations to reflect the changes made experimentally to control the end of compression temperatures. The results of the model predictions are presented in Figure 4-3 as the dashed line (current work) and dotted line (Zhang et al. [55]). During the process of developing the reaction mechanism (provided in the supplemental material) in the current work, sensitivity analysis was performed to identify important reactions. Some rate coefficients were then modified slightly to improve the agreement between the model predictions and the experimental data. In particular, the R+O2 reactions of the mh3d radicals, especially those at allylic sites have the highest uncertainties. These allylic sites are responsible for the reductions in cetane number associated with methyl oleate, methyl linoleate and methyl linolenate; the biodiesel fuel components that have one or more C=C double bonds. As seen in Figure 4-3, both

reaction mechanisms are in excellent agreement with the experimental data for ignition delay time.

Intermediate Species

Figure 4-4 presents typical gas chromatographs used to identify and quantify intermediate species from mh3d autoignition experiments. Some features of the chromatograms were both identified and quantified. Methane (CH_4) and 1-butene (C_4H_8-1) eluted distinctly across all three GC systems and showed excellent agreement between the measured concentrations. Ethane (C_2H_6), ethene (C_2H_4), ethanal (CH_3CHO), and propene (C_3H_6) eluted distinctly across two of three GC systems and also showed excellent agreement in measured concentrations. Only GC2 was capable of quantifying methanol.

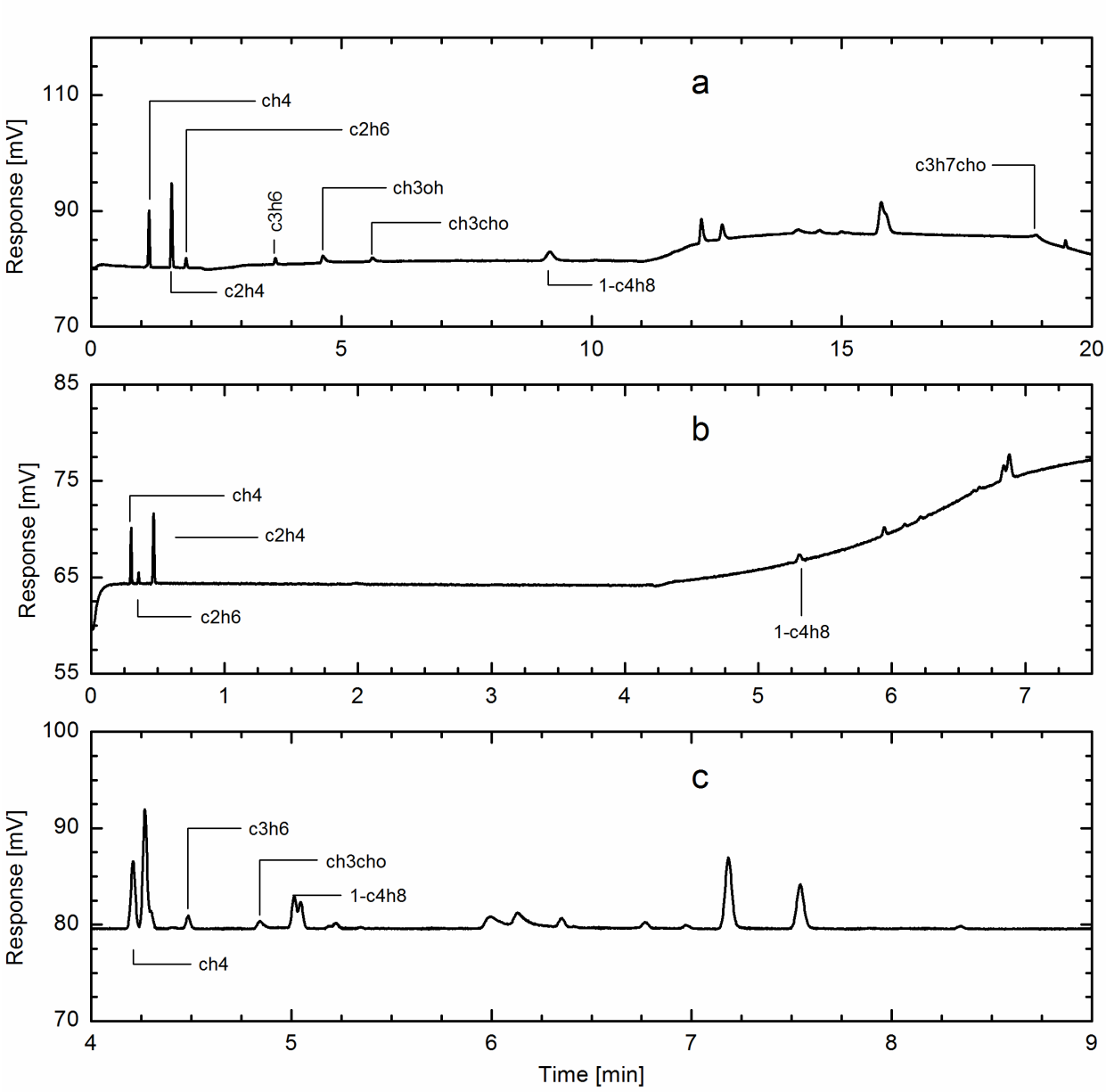

Figure 4-4. Typical gas chromatograms from methyl *trans*-3-hexenoate experiments: (a) GC2 - oxygenates, (b) GC3 - smaller hydrocarbons, (c) GC4 - larger hydrocarbons. The data are from the speciation experiment shown in Figure 4-1.

Ethyne (C_2H_2), ethanol (C_2H_5OH), propane (C_3H_8), and but-3-en-1-ol (C_4H_7OH) were below the detectable limits (<10 ppm). Butanal (C_3H_7CHO) was found to be most accurately quantified by calibrations using peak response height, and a higher uncertainty (a factor of 3) is recommended for the experimental measurements of butanal due to peak tailing and a sharp change in the baseline response at the time

of elution. A fourth column (DB-WAX, Agilent J&W) via FID-GC was used to identify methyl *trans*-3-hexenoate; however, a reliable calibration could not be determined at the concentrations used in the experiments. At high concentrations (> ~0.25%, mole basis), methyl *trans*-3-hexenoate exhibited a high tendency to adsorb and condense when injecting calibration standards despite efforts to reduce these effects (i.e., heated injection lines, controlled dilution of samples). The results of the gas sampling experiments are presented in Figure 4-5.

Figure 4-5 presents the measured results for the stable intermediates where the time scale has been normalized from $t/\tau_{ign} = 0$ (end of compression) to $t/\tau_{ign} = 1$ (autoignition). The experimental results are the average of the measurements from the two sampling systems and from the multiple columns (where available). The horizontal and vertical error bars represent the uncertainty in the sample timing (±1.2 ms) and the measured species (±50%) respectively. Comparing the experimental data, ethene and methane were formed in the highest concentrations with peak values of over 300 ppm. All the other measured intermediates were formed at values less than 100 ppm.

Table 4-4. Summary of experimental conditions and results for mh3d sampling experiments.

φ	**Inert:O_2**	**Test Gas Composition**				**P_{eff}**	**T_{eff}**	**τ_{ign}**	**t_{sample}**
		χ(mh3d)	$\chi(O_2)$	$\chi(N_2)$	$\chi(CO_2)$				
		[%]	[%]	[%]	[%]	[atm]	[K]	[ms]	[ms]
0.29	3.76	0.66	20.85	76.03	2.45	10.2	933	16.0	1.1
0.30	3.76	0.68	20.85	76.05	2.41	10.2	932	15.1	2.9
0.30	3.76	0.69	20.85	76.05	2.40	10.1	930	15.6	4.8
0.30	3.76	0.69	20.87	75.10	3.33	10.5	933	14.4	6.9
0.30	3.77	0.69	20.80	75.18	3.33	10.4	933	14.1	8.2
0.29	3.77	0.66	20.84	76.04	2.45	10.6	942	12.7	10.4
0.28	3.77	0.65	20.84	76.13	2.37	10.4	938	14.9	11.2
0.30	3.75	0.69	20.88	76.01	2.41	10.3	936	14.2	12.2
0.29	3.77	0.68	20.83	76.07	2.41	10.3	933	14.7	12.4

The speciation data are compared to predictions from the two reaction mechanisms in Figure 4-5. A 0-D, isometric, adiabatic CHEMKIN simulation was used for the mechanism predictions where the initial conditions were the average conditions of the sampling experiments: P_{eff} = 10.3 atm, T_{eff} = 934 K, ϕ = 0.29, $\chi(O_2)$ = 20.85%, and inert:O_2 = 3.76. The agreement between the experimental data and the mechanism developed in the current work is generally quite good, typically within a factor of two and within the experimental uncertainties.

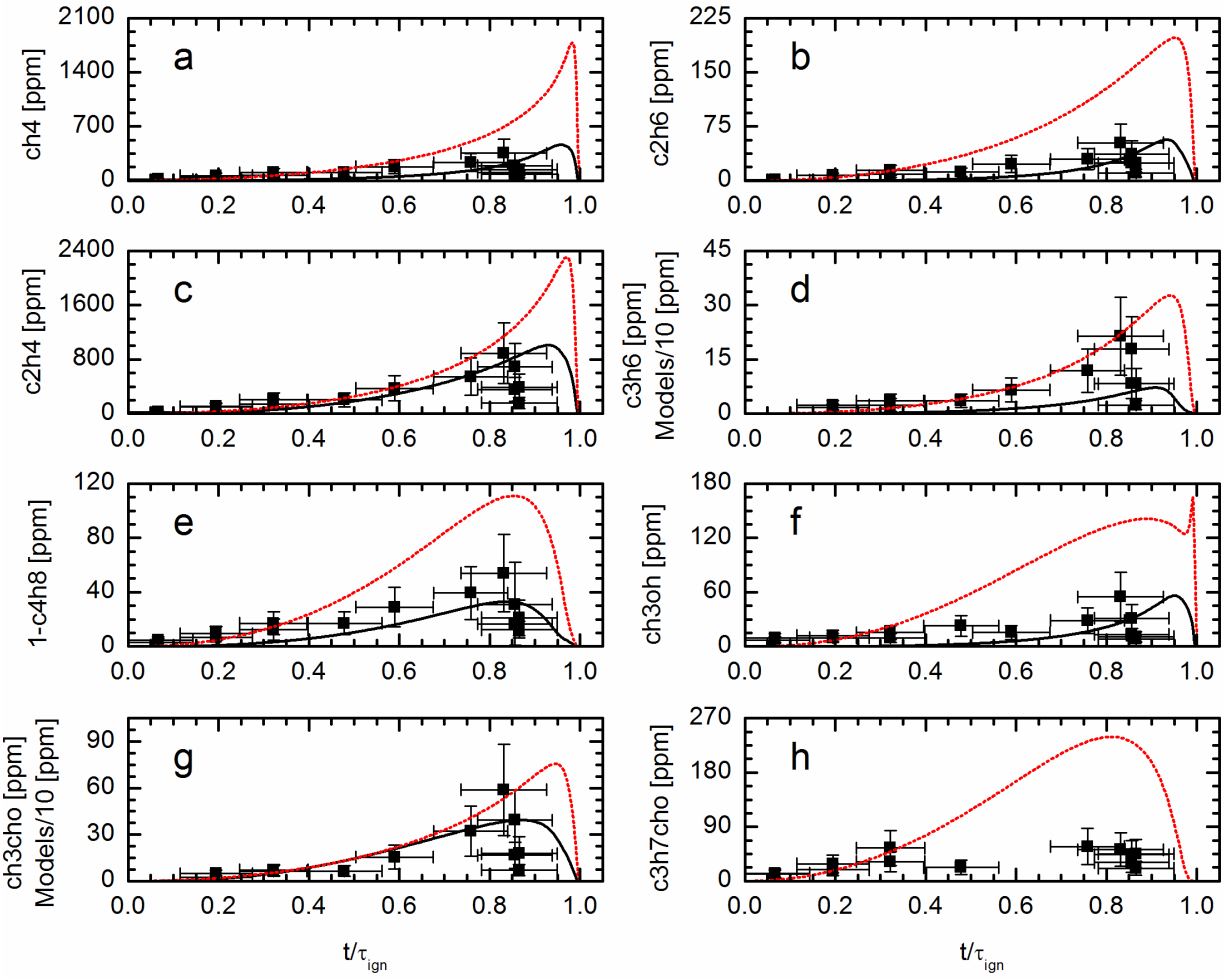

Figure 4-5. Stable intermediate time histories (mole fraction) during mh3d autoignition: a) CH_4, b) C_2H_6, c) C_2H_4, d) C_3H_6, e) 1-C_4H_8, f) CH_3OH, g) CH_3CHO, h) C_3H_7CHO. Experimental results of the current work are represented as symbols and the black solid line is the result of the mechanism developed in this study. The results using the Zhang et al. [55] mechanism are shown as the red dotted line. Average conditions for the sampling experiments were P_{eff} = 10.3 atm, T_{eff} = 934 K, ϕ = 0.30, $\chi(O_2)$ = 20.90%, inert:O_2 = 3.76.

For the species that were monitored in the experiments, yet below the detectable limits of the GC systems, the mechanism was in good agreement, predicting mole fractions of less than 3 ppm for ethanol and less than 1 ppm for propane. However, the mechanism only predicts trace amounts of butanal, less than 18 ppb, which does not agree with the experimental results. The isomer but-3-en-1-ol was not included in the kinetics model developed, but predictions for isomers but-1-en-1-ol and but-2-en-1-ol remain below 5 ppm each during the ignition delay time. Ethyne mole fractions of over 1500 ppm were predicted by the model which is significantly higher than the upper limit determined experimentally of less than 10 ppm.

Model predictions based on the Zhang et al. [55] mechanism (included in Figure 4-5) are consistently higher than the predictions using the reaction mechanism developed in the current work. The level of agreement with the experimental data is generally good (within a factor of 3) with the exception of the peak values predicted from some of the unsaturated species (ethyne and propene) and ethanal which differ by a factor of 10 or more. Recall that both reaction mechanisms were in good agreement with the experimental data for ignition delay time. Each reaction mechanism indicates that the allylic C-H bonds adjacent to the carbonyl group are weak and the vinylic bonds are strong when compared to the C-H bonds at equivalent sites found in saturated fuels. These agreements, and others, on the effect of the double bond in mh3d lead to trend-wise agreement in the predicted effects at low and high temperatures (e.g., increased ignition delay times at low temperatures, increased production of unsaturated and oxygenated species at high temperatures). However, there are numerous species and reactions in each mechanism that are absent from the other, i.e. the reaction pathways predicted by each can differ significantly. A complete understanding of the similarities and discrepancies in the two reaction mechanisms for predicting the small intermediates is beyond the scope of the current study and may not yield definitive conclusions. The differences between the predictions of the two mechanisms highlight the complexity and uncertainty of modeling the reaction pathways for

forming and consuming these small intermediate species. The results further highlight the importance of ignition delay time and speciation data for providing rigorous targets for understanding reaction pathways and validating chemistry.

The speciation results of this study provide an interesting new challenge for kinetic modeling that underscores the importance of new studies of unsaturated methyl ester fuels. The first few reactions for fuels with one or more C=C double bonds are not much different from those of saturated fuels, but eventually smaller fragment species are produced with one or more double bonds, and current modeling capabilities are comparably much less developed for such species. Examples of such species are C_3H_4, C_4H_6, C_5H_8, as well as the many polyunsaturated radical species that can be produced. These unsaturated species have multiple isomeric forms, often resonantly related, and most have yet received very little kinetic analysis. Without prior guidance about how to deal with these species, it is often difficult to identify the specific products from their reactions, and the few such species that have been studied are often used, in the absence of any information to the contrary. In the present mechanism, it is clear that too many of these reactions have been assumed to produce ethyne or vinyl radicals, and the large overestimation of ethyne, relative to the experimentally measured value, is evidence that this portion of the mechanism needs further attention. Results derived from further small molecule studies will benefit future mechanisms for large biodiesel fuels.

The sampled intermediate species (i.e., methane, methanol, ethane, ethene, ethanal, propene, 1-butene, and butanal) account for ~6.1% of the carbon and ~8.3% of the hydrogen. In comparison, the developed mechanism predicts values of ~5.6% of the carbon and ~6.7% of the hydrogen for the same species. The simulations from the developed mechanism indicate that a significant fraction of the carbon and hydrogen in the system remains in methyl *trans*-3-hexenoate (~30% mole basis) and other species (e.g., ~12% in methyl 3,5-hexenoate, ~6% in methyl 3,4-hexenoate), for which reliable calibrations could not be obtained, late in the ignition delay period (t/τ_{ign} = 0.80). While the species measured do not close the carbon or hydrogen

balance in the system, the data provide valuable information on the intermediate reaction pathways important during mh3d autoignition.

4.5 Conclusions

The current work presents new measurements of methyl *trans*-3-hexenoate ignition delay times and of intermediate species formed during mh3d ignition. Such data are vital to understanding the effects of unsaturated esters on combustion kinetics. The autoignition data quantify the faster autoignition of the longer chain ester compared to other shorter length saturated and unsaturated esters. The study also identifies areas of high uncertainty in the reaction chemistry for unsaturated esters, including the change in the reaction rates of important $R+O_2$ reactions compared to unsaturated esters, and the reaction pathways involving smaller unsaturated and poly-unsaturated stable and radical species. The kinetic features associated with the C=C double bond are important, and these experimental data inform model development and guide further experimental studies to quantify the combustion chemistry of practical biodiesel and related fuels.

Chapter 5
Laser Schlieren Interrogation of Phenyl Oxidation

5.1 Objective

Aromatic compounds are significant components of fuel blends and central intermediates in the pathways of soot formation and oxidation. The objective of this study was to quantify phenyl oxidation reaction (i.e., $C_6H_5 + O_2$) rates and pathways using the Argonne National Laboratory diaphragmless shock tube at high temperature (> 1000 K), low pressure conditions (< 1 atm). Axial density gradients of the reacting system were measured with a laser schlieren technique. A chemical kinetic mechanism which accounts for the generation and subsequent oxidation of the phenyl radical was developed to interpret the experimental measurements. Results presented in this chapter highlight the promise, and challenges, associated with application of the laser schlieren technique to the study of oxidation reactions.

5.2 Experimental Approach

Phenyl oxidation experiments were performed using the Argonne National Laboratory diaphragmless shock tube (ANL DFST). Details regarding the experimental facility and procedures of this study are given in Section 2.2. Gases used in the preparation of test mixtures and experiments include oxygen (99.99%, Air Gas), krypton (99.999%, Air Gas), and helium (99.999%, Air Gas). Vapor from liquid phase iodobenzene (98%, Sigma Aldrich) was used as the precursor for generating phenyl radicals.

Laser Schlieren

Molar refractivity values were taken from Gardiner et al. [112] (Kr – 6.382, O_2 – 4.035) or calculated from the index of refraction and the density using the

methodology of Birch [113] (C_6H_5I – 39.15). It was assumed that the mixture molar refractivity did not change significantly during reaction. This is generally an excellent approximation for dilute mixtures such as used in the current work.

5.3 Reaction Mechanism Development

A reaction mechanism was developed for the oxidation of phenyl radicals (the structure is presented in Figure 5-1) by molecular oxygen and is presented in Table 5-1. A subset of the mechanism is based on the experimental and theoretical work of Tranter et al. [60] in which iodobenzene decomposition and phenyl-phenyl reactions were studied. Experiments by Tranter et al. [60] were conducted in the ANL DFST with laser schlieren and time of flight mass spectrometry at similar conditions to the current work.

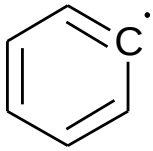

Figure 5-1. Molecular structure of a phenyl radical with the radical site indicated.

Initial rates for phenyl oxidation and secondary reactions were based on studies by Frank et al. [62] and Kumaran and Michael [64], which utilized atomic and molecular resonance absorption spectroscopy for their measurements. Phenyl oxidation rates were subsequently modified in the current work to fit the experimental measurements. In the current work, another subset of reactions was included to account for high temperature hydrogen chemistry based on a private communication with Sivaramakrishnan [114] and work by Michael [115]. The rate of cyclopentadienyl (*c*-C_5H_5) decomposition at 100 torr was used from a theoretical study by Moskaleva and Lin [116]. Thermochemical properties for the reaction mechanism presented in this work are based on the work by Tranter et al. [60] and Goos et al. [117] and are provided in Table B-1. Reactions presented in Table 5-1

are assumed to be reversible and reverse rates are calculated from equilibrium constants and thermochemical properties.

Table 5-1. Reaction mechanism and Arrhenius parameters for phenyl radical oxidation.

	Reaction [a]	log(A)	n	E_a	$\Delta H_{r,298K}$	References
1	$C_6H_5I \rightarrow C_6H_5 + I$					
	120 torr	72.783	-17.1	46.73	66.8	[60]
	60 torr	77.483	-18.6	47.63	66.8	[60]
2	$C_6H_5 + C_6H_5 \rightarrow C_{12}H_{10}$	22.508	-2.8	2.41	-117.6	[60]
3	$OH + H_2 \rightarrow H_2O + H$	8.331	1.5	1.74	-14.6	[114]
4a	$O + OH \rightarrow O_2 + H$	18.420	-1.8	0.43	-16.4	[114]
4b	$O + OH \rightarrow O_2 + H$	18.207	-1.4	4.36	-16.4	[114]
5	$O + H_2 \rightarrow OH + H$	4.704	2.7	3.17	1.5	[114]
6	$H + O_2 + M \rightarrow HO_2 + M$	20.857	-1.7	0.27	-49.2	[114]
7	$HO_2 + H \rightarrow OH + OH$	12.824	0.3	-0.06	-37.2	[114]
8	$C_6H_5I + C_6H_5 \rightarrow C_{12}H_{10} + I$	12.300	0.0	5.54	-50.8	[60]
9	$C_6H_5 + H \rightarrow C_6H_6$	49.495	-10.2	11.41	-112.8	[60]
10	$C_6H_6 + H \rightarrow C_6H_5 + H_2$	14.540	0.0	8.11	8.6	[60]
11	$C_6H_6 + C_6H_5 \rightarrow C_{12}H_{10} + H$	12.300	0.0	5.54	-4.8	[60]
12	$C_6H_5I + H \rightarrow C_6H_5 + HI$	5.941	2.5	-0.07	-4.1	[60]
13	$H + HI \rightarrow H_2 + I$	13.600	0.0	0.00	-33.3	[60]
14	$o\text{-}C_6H_4 \rightarrow C_4H_2 + C_2H_2$	14.813	0.0	41.77	53.8	[60]
15	$H + O_2 \rightarrow OH + O$	14.281	0.0	8.26	16.4	[115]
16	$H + H + M \rightarrow H_2 + M$	17.800	-1.0	0.00	-104.2	[60]
17	$C_6H_5I \rightarrow o\text{-}C_6H_4 + HI$	75.540	-18.3	47.45	77.7	[60]
18	$C_6H_5 + O_2 \rightarrow p\text{-}C_6H_4O_2 + H$	13.306	0.0	4.52	-57.5	p.w.
19	$C_6H_5 + O_2 \rightarrow C_6H_5O + O$	13.111	0.0	3.08	-6.3	p.w.
20	$C_6H_5O \rightarrow c\text{-}C_5H_5 + CO$	11.869	0.0	22.07	21.8	[62]
21	$C_6H_5 + O \rightarrow c\text{-}C_5H_5 + CO$	13.699	0.0	0.00	-103.6	p.w.
22	$c\text{-}C_5H_5 + O \rightarrow C_5H_4O + H$	13.840	0.0	0.00	-57.2	p.w.
23	$c\text{-}C_5H_5 + H \rightarrow c\text{-}C_5H_6$	14.178	0.0	0.00	-82.9	[64]
24	$p\text{-}C_6H_4O_2 \rightarrow C_5H_4O + CO$	11.869	0.0	29.70	15.8	[62]
25	$HO_2 + H \rightarrow H_2 + O_2$	7.049	1.9	-0.32	-55.0	[114]
26	$HO_2 + O \rightarrow O_2 + H$	10.455	1.0	-0.36	-10.4	[114]
27a	$OH + OH \rightarrow O + H_2O$	13.452	-0.8	-0.23	-16.1	[114]

27b	$OH + OH \rightarrow O + H_2O$	4.100	2.5	-0.82	-16.1	[114]
28	$H + OH + M \rightarrow H_2O + M$	21.656	-1.8	0.25	-118.8	[114]
29	$H + O + M \rightarrow OH + M$	16.792	-0.6	0.00	-102.7	[114]
30	$O + O + M \rightarrow O_2 + M$	13.277	0.0	-0.90	-119.1	[114]
31	$OH + OH + M \rightarrow H_2O_2 + M$	25.754	-3.4	0.29	-50.3	[114]
32	$C_6H_5 + C_6H_5 \rightarrow o\text{-}C_6H_4 + C_6H_6$	-2.768	4.6	-2.89	-30.9	[60]
33	$c\text{-}C_5H_5 \rightarrow C_2H_2 + C_3H_3$	79.446	-18.3	65.84	75.7	[116]

[a] Rate constants are provided as $k = AT^n\exp(-E_a/RT)$, with units of cm^3, mol, s, and kcal.

5.4 Experimental Results

Incident shock waves were used to achieve the desired thermodynamic state conditions for laser schlieren measurements of phenyl oxidation reactions. Incident shock pressures (P_2) and temperatures (T_2) were calculated using the shock velocity, initial pressures (P_1) and temperatures (T_1), and isentropic shock wave relations. Uncertainty for the incident shock temperatures presented in this study are estimated to be ~10 K based on the work by Lynch et al. [88]. Mixtures of 0.5% iodobenzene with two oxygen concentrations (2.5% and 5% in krypton buffer gas) were each shock heated to two nominal pressures (P_2 = 59 ± 2 torr and 121 ± 6 torr) and high temperatures (1299 ≤ T_2 ≤ 1739 K). Table 5-2 presents the state conditions and mixture compositions for the experiments in this study.

Table 5-2. Reactant composition and state conditions of laser schlieren shock tube experiments.

$\chi(C_6H_5I)$ [%]	$\chi(O_2)$ [%]	$\chi(Kr)$ [%]	P_1 [torr]	T_1 [K]	P_2 [torr]	T_2 [K]
2.0	0.0	98.0	7.00	21.8	128	1393
2.0	0.0	98.0	6.00	21.8	130	1588
2.0	0.0	98.0	6.50	21.8	131	1505
2.0	0.0	98.0	6.00	21.7	135	1639
0.5	2.5	97.0	3.60	22.2	56	1350
0.5	2.5	97.0	3.70	22.0	57	1341
0.5	2.5	97.0	3.50	22.0	58	1420
0.5	2.5	97.0	3.50	22.0	59	1429

0.5	2.5	97.0	3.70	22.0	59	1369
0.5	2.5	97.0	3.50	22.1	59	1444
0.5	2.5	97.0	3.30	22.2	60	1527
0.5	2.5	97.0	3.50	22.2	60	1459
0.5	2.5	97.0	3.90	22.0	60	1338
0.5	2.5	97.0	3.30	22.2	60	1530
0.5	2.5	97.0	3.20	22.2	61	1592
0.5	2.5	97.0	6.40	22.5	113	1493
0.5	2.5	97.0	7.00	22.5	113	1391
0.5	2.5	97.0	6.70	22.5	115	1456
0.5	2.5	97.0	7.10	22.6	115	1395
0.5	2.5	97.0	6.95	22.6	115	1421
0.5	2.5	97.0	7.30	22.0	117	1380
0.5	2.5	97.0	7.70	22.0	117	1327
0.5	2.5	97.0	6.85	22.6	118	1464
0.5	2.5	97.0	7.10	22.0	119	1425
0.5	2.5	97.0	8.00	22.0	119	1299
0.5	2.5	97.0	6.30	22.5	119	1580
0.5	2.5	97.0	6.85	22.5	120	1479
0.5	2.5	97.0	6.50	22.5	121	1561
0.5	2.5	97.0	6.80	22.6	123	1518
0.5	2.5	97.0	7.10	22.0	125	1484
0.5	2.5	97.0	7.30	22.5	125	1460
0.5	2.5	97.0	6.80	22.5	127	1558
0.5	2.5	97.0	7.20	22.5	130	1523
0.5	2.5	97.0	7.10	22.5	132	1557
0.5	5.0	94.5	3.25	27.9	54	1422
0.5	5.0	94.5	3.30	27.9	56	1453
0.5	5.0	94.5	3.10	27.5	57	1543
0.5	5.0	94.5	3.45	27.9	57	1420
0.5	5.0	94.5	3.10	27.5	58	1558
0.5	5.0	94.5	3.00	27.5	59	1639
0.5	5.0	94.5	3.02	27.5	64	1739
0.5	5.0	94.5	6.80	28.5	115	1453
0.5	5.0	94.5	7.40	28.4	118	1384

0.5	5.0	94.5	6.95	28.5	119	1460
0.5	5.0	94.5	7.70	28.4	119	1352
0.5	5.0	94.5	7.20	28.4	120	1434
0.5	5.0	94.5	6.95	28.4	121	1479
0.5	5.0	94.5	7.10	28.4	121	1463
0.5	5.0	94.5	7.00	28.5	122	1481
0.5	5.0	94.5	6.70	28.5	122	1535
0.5	5.0	94.5	6.60	28.5	122	1559
0.5	5.0	94.5	6.55	28.5	123	1580
0.5	5.0	94.5	7.30	28.4	125	1461
0.5	5.0	94.5	6.70	28.5	125	1570
0.5	5.0	94.5	7.00	28.4	126	1522
0.5	5.0	94.5	6.60	28.4	139	1728

Four typical plots of unprocessed signals from laser Schilieren DFST experiments are presented in Figure 5-2. The shock wave and laser beam interact causing, in most experiments, a small negative response (t ~ 9-10 μs) followed by a much larger positive response (t ~10-11 μs). Chemical reactions begin within the timeframe of the shock/laser beam interaction and therefore the initial reaction time, t_0, is determined following methods established by Kiefer et al. [89,90]. The methodology of Kiefer et al. [89,90] was used to determine an estimate of the initial reaction time which was then corrected for optical shift, shock curvature, and beam signal modulation effects. The corrected initial reaction time is known with an accuracy of <~0.2 μs. The influence of chemical reactions on the raw signal can be seen in each of the plots of Figure 5-2 after the shock wave has passed and the signal gradually returns to baseline values (t ~ 11-15 μs).

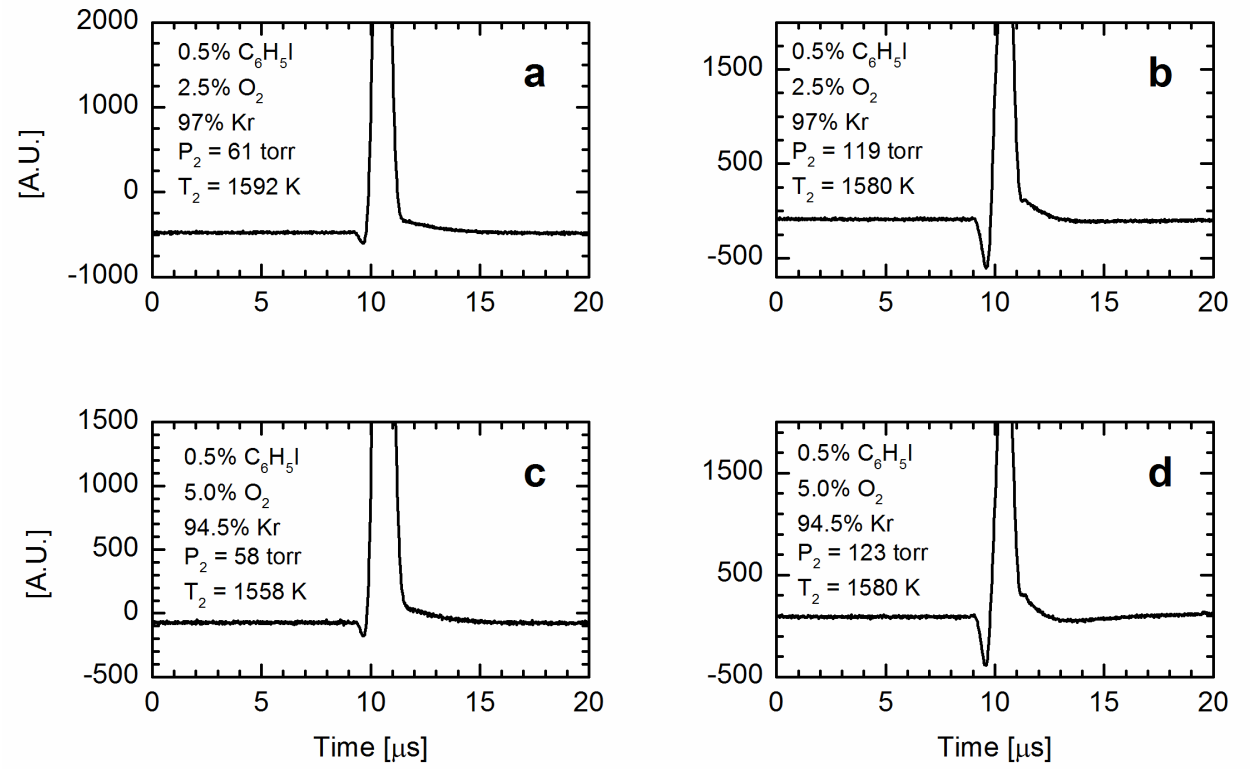

Figure 5-2. Typical raw profiles from laser schlieren shock experiments for iodobenzene/oxygen/krypton mixtures.

Displayed in Figure 5-3 are the four plots of the density gradients corresponding to the unprocessed signals presented in Figure 5-2. The density gradients are determined from the unprocessed signal using the methodology described in section 2.2. The initial (t <~1-2 μs) density gradients, $(d\rho/dx)_0$, in Figure 5-3 are determined by extrapolation of the experimental data to the initial reaction time, t_0. The entire time history of the experimental absolute density gradient was modeled, and individual reaction rates determined, based on the mechanism presented in section 5.3 and a software program at ANL which is based on the methodology of Gardiner et al. [118].

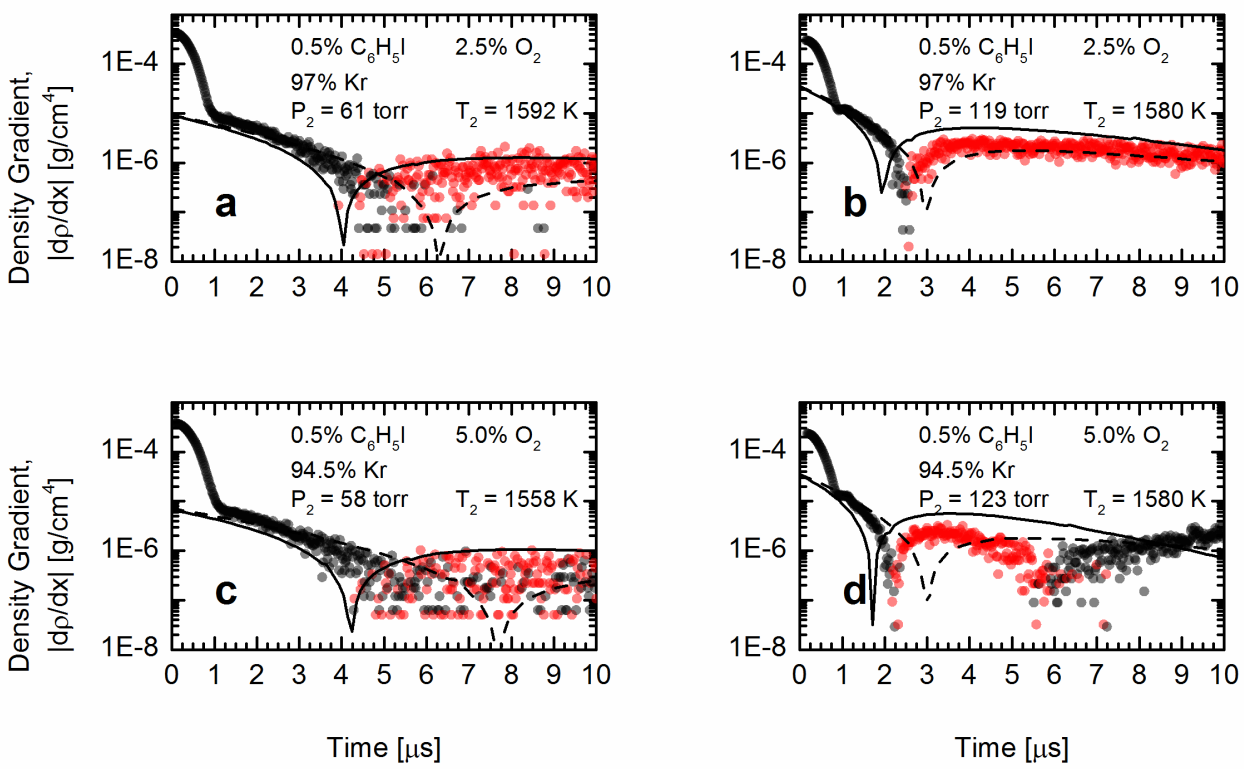

Figure 5-3. Density gradients for shock heated iodobenzene/oxygen/krypton mixtures. Unprocessed data for the corresponding experiments are shown in Figure 5-2. Symbols indicate experimental results, where black symbols denote positive density gradients and red symbols denote negative density gradients. Lines are simulation results, dashed for iodobenzene decomposition and phenyl recombination and solid for phenyl oxidation. See text for details.

Two sets of simulation results are provided in Figure 5-3. Simulations for the decomposition of iodobenzene and phenyl recombination (i.e., without the presence of oxygen) are indicated by the dashed lines in Figure 5-3. In this study, the density gradient at early times $(d\rho/dx)_0$ is a result of the rate of iodobenzene decomposition which was determined by Tranter et al. [60]. Unexpectedly, the early portion of the time history of the density gradient is in good agreement with the model predictions for thermal decomposition of iodobenzene for these oxidation experiments. Additional iodobenzene pyrolysis experiments (see Table 5-2) were conducted and the current measurements are in excellent agreement with the work of Tranter et al. [60]. Also presented in Figure 5-3 are simulation results for the complete phenyl oxidation mechanism represented by the solid lines. The

predictions based on the oxidation mechanism shifts the inflection point of the density gradient to earlier times compared to the pyrolysis predictions. Agreement of the oxidation mechanism with the experimental measurements is fair at the high temperature conditions presented in Figure 5-3 and at the lower temperature conditions of Figure 5-4.

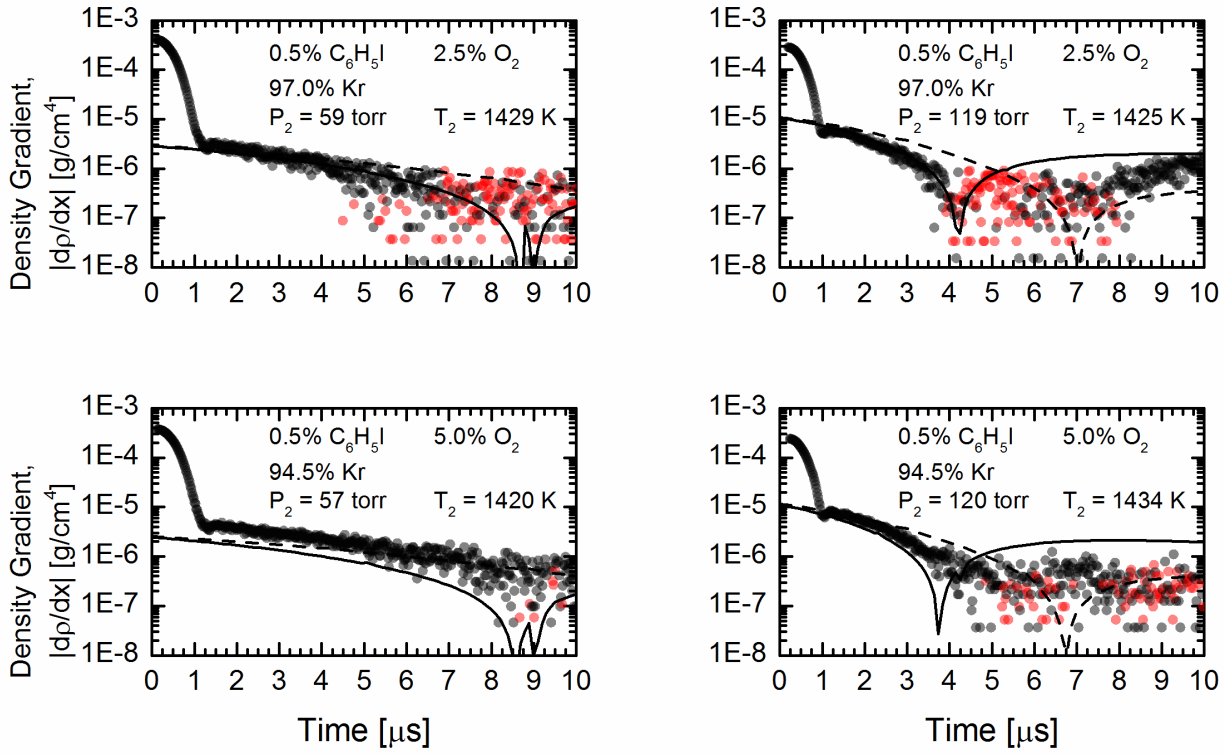

Figure 5-4. Density gradients for lower temperature (~1427 K) shock heated iodobenzene/oxygen/krypton mixtures. Symbols indicate experimental results, where black symbols denote positive density gradients and red symbols denote negative density gradients. Lines are simulation results, dashed for iodobenzene decomposition and phenyl recombination and solid for phenyl oxidation. See text for details.

Sensitivity analysis of the simulated density gradient to variations in each of the reaction rates was conducted. Reactions 18, 19, 21, and 22 have the largest impact on the density gradients predicted by the mechanism simulations.

$$C_6H_5 + O_2 \rightarrow p\text{-}C_6H_4O_2 + H \quad \text{(R18)}$$

$$C_6H_5 + O_2 \rightarrow C_6H_5O + O \quad \text{(R19)}$$

$$C_6H_5 + O \rightarrow c\text{-}C_5H_5 + CO \quad \text{(R21)}$$

$$c\text{-}C_5H_5 + O \rightarrow C_5H_4O + H \quad \text{(R22)}$$

The reaction mechanism presented in Table 5-1 was modified by decreasing the A-coefficients for reactions R18, R19, R21, and R22 within a factor of 2 from previous literature values to improve agreement of the simulations with the experimental measurements. The results for the modified oxidation reaction mechanism are presented in Figure 5-3. Decreasing the rate coefficients for these reactions slowed oxidation of the phenyl radicals produced by the iodobenzene decomposition, thereby shifting the decrease in the density gradient to later times. The initial rates for R18, R19, and R21 were based on the phenyl oxidation study by Frank et al. [62]. The measurements made by Frank et al. [62] using resonance absorption spectroscopy (of H, O, I and CO) were taken at higher pressures (>1 bar) than the current work. Measurements from the phenyl oxidation work by Kumaran and Michael [64] were used for the initial rates for R22. Kumaran and Michael [64] also conducted higher pressure (> 269 torr) experiments with atomic resonance absorption spectroscopy (of H and O). The lower pressures of the current study and the limited studies of the secondary reactions R21 and R22 indicate the decrease in the reaction rates required for the simulations to agree with the experimental results are within reasonable uncertainty bounds for the reactions.

The sensitivity analysis of the mechanism highlights uncertainties associated with secondary reactions (e.g., R21 and R22). Additional secondary chemistry concerns can be, in part, addressed by utilizing additional experimental diagnostic techniques. Time of flight mass spectroscopy has been previously used in the ANL DFST to further refine the rate coefficients included in predictive mechanisms [60,88]. The phenyl oxidation mechanism is also sensitive to thermochemistry values, such as the reference enthalpies and entropies of *p*-$C_6H_4O_2$ and C_6H_5O, which have been subject to limited experimental and theoretical studies.

Experimentally measured density gradients presented in this work are also subject to uncertainties that can be reduced with additional experiments. Initial mixture compositions and state conditions affect the baseline perturbations, uncertainty in the initial reaction time, and the signal to noise ratios of the

experimental data. A broader range of compositions and conditions (i.e., incident shock pressures) would reduce these experimental uncertainties.

5.5 Conclusions

In this study, new experimental measurements of phenyl oxidation were taken with the laser schlieren technique at low pressure, high temperature conditions created by incident shock waves. The experimental measurements presented demonstrate the novel application of laser schlieren to radical oxidation. A kinetic mechanism was created that captures some of the trends of the density gradients measured experimentally. Phenyl oxidation rates from the current work are in fair agreement with previous literature values. The current work indicates that understanding of phenyl oxidation is inadequate and that alternative pathways to R18 ($C_6H_5 + O_2 \rightarrow p\text{-}C_6H_4O_2 + H$) and R19 ($C_6H_5 + O_2 \rightarrow C_6H_5O + O$) may be active. This study is the first to take laser schlieren measurements of radical+O_2 reactions, building on previous work utilizing laser schlieren to study the oxidation of stable species [65]. This study validates the approach of measuring radical oxidation reaction rates by laser schlieren, with similar potential and challenges to previous pyrolysis studies. Future oxidation studies at lower temperature, higher pressure conditions may be possible, which would provide invaluable kinetic information on low temperature chemistry pathways.

Chapter 6
Linear Hexene Isomer Ignition and Speciation Experiments

6.1 Objective

Alkenyl features are present in fuels, their stable intermediates, and design surrogates for combustors and are not quantitatively well understood. The objective of this work was to quantify the impact of the carbon-carbon double bond position on global chemical kinetics and reaction pathways using the University of Michigan rapid compression facility and the three *trans*-hexene isomers. Ignition delay times were measured and correlated with high speed imaging to quantify the impact on global combustion chemistry. Stable intermediates were captured with fast gas sampling and measured with gas chromatography techniques to provide insight on reaction pathways. Comparisons to previous experimental and computational work provide additional context for the impact of the double bond position. The experimental results of this study highlight the significant impact alkenyl features can have on ignition timing and emissions composition.

6.2 Experimental Approach

Ignition delay and speciation experiments were conducted in this work using the University of Michigan rapid compression facility (UM RCF). Details regarding the experimental facility and procedures of this study are provided in section 2.1. The pressure transducer used in the test section of the UM RCF was a Kistler 6045A, while the transducer used in the mixing manifold was a MKS Baratron 690A13TRB. High speed imaging was taken with a Vision Research Phantom v711 camera.

Gas Chromatography

Four GCs (Perkin Elmer Autosystem) and columns allowed the stable intermediate species to be identified and quantified. GC-OHC used a flame ionization detector (FID) with a Varian CP-Porabond Q capillary column to target hydrocarbon species up to C_6, including oxygenates. GC-C5 used a FID with a Varian CP-Al_2O_3/Na_2SO_4 capillary column to target species smaller than C_5. GC-LVHC is equipped with a FID with a Varian DB-Wax capillary column to target low volatility and high polarity species. GC-PG utilized a thermal conductivity detector (TCD) and a Restek ShinCarbon ST packed column to target permanent gases and light hydrocarbon species. Helium was used as the carrier gas in all the GCs. Table 6-1 contains the temperature methods applied for each of the columns used in this study.

Table 6-1. Gas chromatography temperature methods for linear hexene speciation experiments.

Column	Length	ID	Film	Carrier Gas	T_{column}	Detector	$T_{detector}$
CP-Porabond Q	25 m	0.53 mm	10 µm	Helium 31 cm/s	40°C (2 min) → 6°C/min 160°C (3 min)	FID	300°C
CP-Al_2O_3/Na_2SO_4	25 m	0.53 mm	10 µm	Helium 32 cm/s	40°C (2 min) → 6°C/min 160°C (3 min)	FID	300°C
DB-WAX	30 m	0.25 mm	0.25 µm	Helium 70 cm/s	40°C (2 min) → 6°C/min 160°C (3 min)	FID	300°C
ShinCarbon ST	2 m	1 mm	N/A	Helium	40°C (2 min) → 6°C/min 160°C (3 min)	TCD	100°C

High purity gases and vapor from high purity liquids were used to determine calibration standards for 29 stable intermediates and mixture components. The calibrated species, purities, and suppliers used in this study are provided in Table C-4. Signals from the gas chromatographs were captured using a high-resolution data acquisition system (NI PXI 4472) at a rate of 8 Hz. Species were calibrated and quantified using the area under the response peak unless otherwise noted.

6.3 Computational Approach

Computational simulations were carried out using the CHEMKIN suite of software (version 10113, x64) [91] and assuming a closed 0-D homogeneous batch reactor at adiabatic, constant volume conditions. Assumptions of a 0-D homogeneous batch reactor at an adiabatic, constant volume condition have been examined previously for experiments that are at moderate ignition delay times (~5-50 ms) [21,86]. It has been found in this work that at appropriate time scales reaction during compression is typically negligible (for τ_{ign} > ~5 ms) and heat transfer effects are well represented by the effective thermodynamic state conditions (for τ_{ign} < ~50 ms), leading to minor differences (< ~15%) in ignition delay times between the methods used in this study and more complex simulations (e.g., contracting and expanding volume time histories). Default values from CHEMKIN were used for the solver tolerances and solver time-steps. A detailed chemical kinetic mechanism developed by Mehl et al. [92] was used to represent the hexene isomers (the structures are presented in Figure 6-1) in simulations. A brief summary of the development and validation of the reaction mechanism used in this study are provided below. The reaction mechanism was selected due to the maturity and extensive validation that has been previously completed on the reaction chemistry. No modifications to reaction rates were made to the mechanism considered in this study. The mechanism does not consider NO_x chemistry.

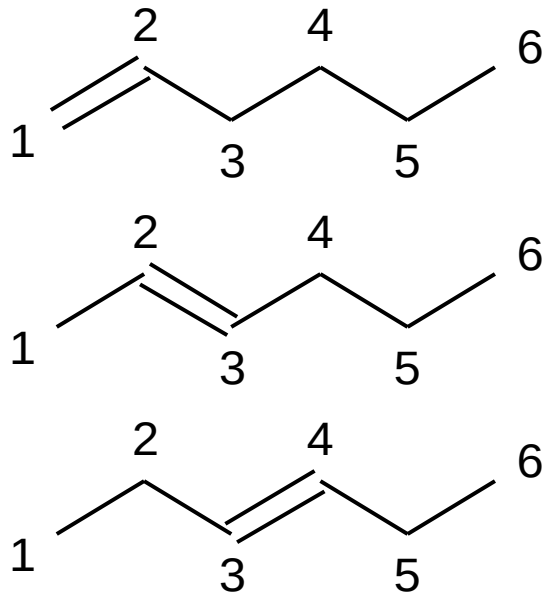

Figure 6-1. Molecular structures of 1-hexene (top row), *trans*-2-hexene (middle row), and *trans*-3-hexene (bottom row) with carbon atoms numbered from left to right.

Initial conditions were selected based on the experimental data collected in this study. The autoignition simulations were conducted at stoichiometric fuel-to-oxygen equivalence ratios (ϕ = 1.0), buffer gas:O_2 = 7.5, an initial pressure of 11 atm, and initial temperatures ranging from 600-1500 K in 25 K increments for all three hexene isomers. Nitrogen was evaluated as the buffer gas in the autoignition simulations of this study. Additional simulations were conducted for the hexene isomers at the state conditions achieved and mixture compositions utilized during gas sampling experiments.

Hexene Mechanism

Autoignition simulations of the hexene isomers in this study were conducted using the LLNL gasoline surrogate chemical kinetic mechanism [92] available online. The gasoline surrogate mechanism was developed to incorporate several sub-mechanisms, including a set of reaction chemistry for the three linear hexene isomers considered in this study. Briefly, the Mehl et al. [92] gasoline surrogate mechanism consists of four sub-mechanisms, with the first sub-mechanism describing small hydrocarbons ($\leq C_4$). The three remaining sub-mechanisms

describe the main reaction pathways for linear saturated and unsaturated hydrocarons ($\leq C_7$), branched hydrocarbons ($\leq C_8$), and aromatics. The most recent updates to small hydrocarbon chemistry and low-temperature chemistry pathways made to the *n*-heptane mechanism in Karwat et al. [86] are not reflected in the Mehl et al. [92] mechanism used in this study. The reaction pathways for the linear hexene isomers in the gasoline surrogate mechanism were based on work by Mehl et al. [77,82]. Regarding the hexene reaction pathways in the gasoline surrogate mechanisms, Mehl et al. [92] reported satisfactory validation of 1-hexene simulations against the low temperature rapid compression machine ignition delay measurements of Vanhove et al. [76]. In their previous work, Mehl et al. [82] reported satisfactory agreement of their mechanism with more validation targets from shock tubes [78,79,82] and a rapid compression machine [76] for the three linear hexene isomers.

6.4 Experimental Results

Ignition Delay Time

Experimental pressure and pressure derivative data for ignition delay time measurements of the three hexene isomers (1-hexene, *trans*-2-hexene, *trans*-3-hexene) are plotted in Figure 6-2. Thermodynamic state conditions used in this study are the effective pressure (P_{eff}) and the corresponding effective temperature (T_{eff}). Effective pressure is defined as the integrated time averaged pressure, beginning at the local maximum in pressure at the end of compression (P_{max}) and ending at the maximum in the pressure derivative (dP/dt_{max}). Effective temperature is calculated from the effective pressure using isentropic relations. The ignition delay time corresponds to the time between P_{max} and dP/dt_{max}.

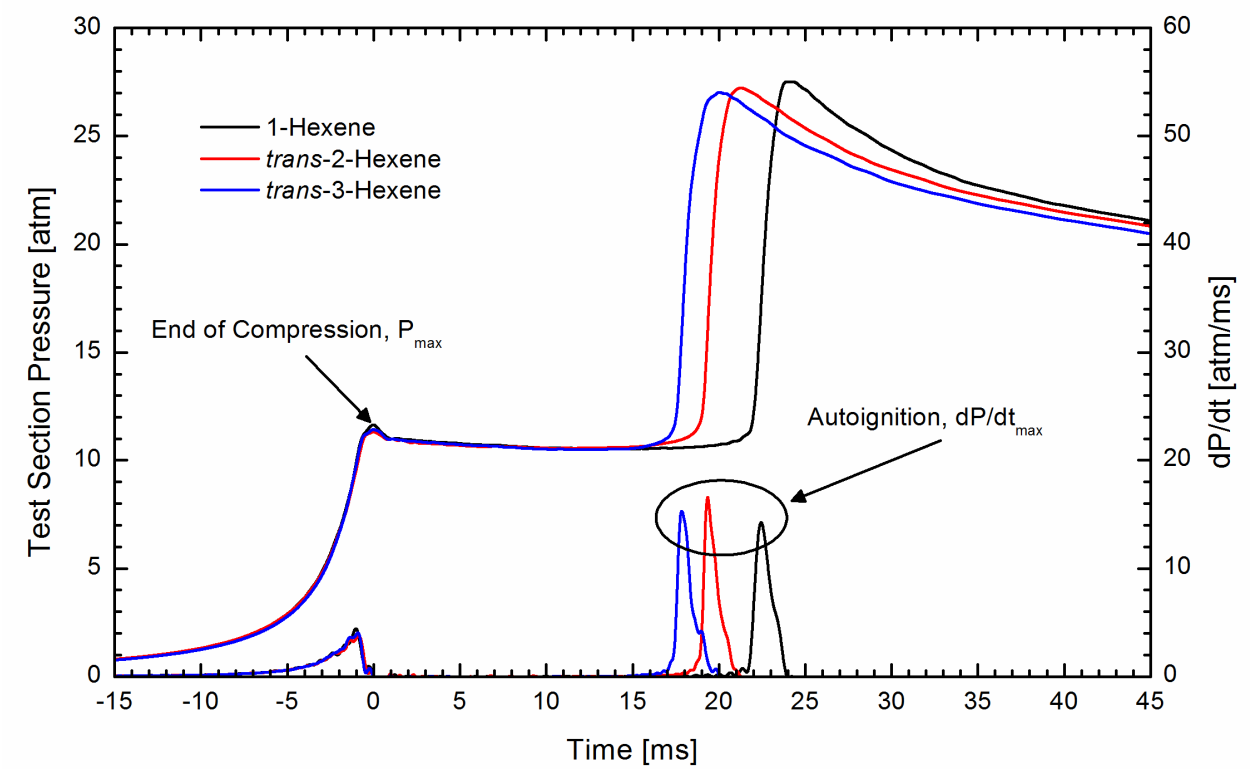

Figure 6-2. Typical pressure and pressure derivative time histories for the three linear hexene isomers. Experimental conditions for all three isomers are ϕ = 1.0, buffer gas:O_2 = 7.5, P_{eff} = 10.8 atm. 1-hexene: T_{eff} = 900 K, τ_{ign} = 22.5 ms. *trans*-2-hexene: T_{eff} = 897 K, τ_{ign} = 19.4 ms. *trans*-3-hexene: T_{eff} = 896 K, τ_{ign} = 17.9 ms.

Typical still images from the high speed imaging taken during the experiments are presented in Figure 6-3. The images shown correspond to the experimental data displayed in Figure 6-2. Blue emission from chemiluminescence was homogeneous in nearly all ignition experiments, and appeared to occur volumetrically in all cases. At the lowest temperatures (<875 K), 1-hexene and *trans*-2-hexene were observed to exhibit ignition that appeared to be initiated concentrically and may be associated with non-Arrhenius behavior at the experimental conditions. Additional pressure time histories from low temperature experiments are provided in Figure C-1, and the corresponding still images are shown in Figure C-2.

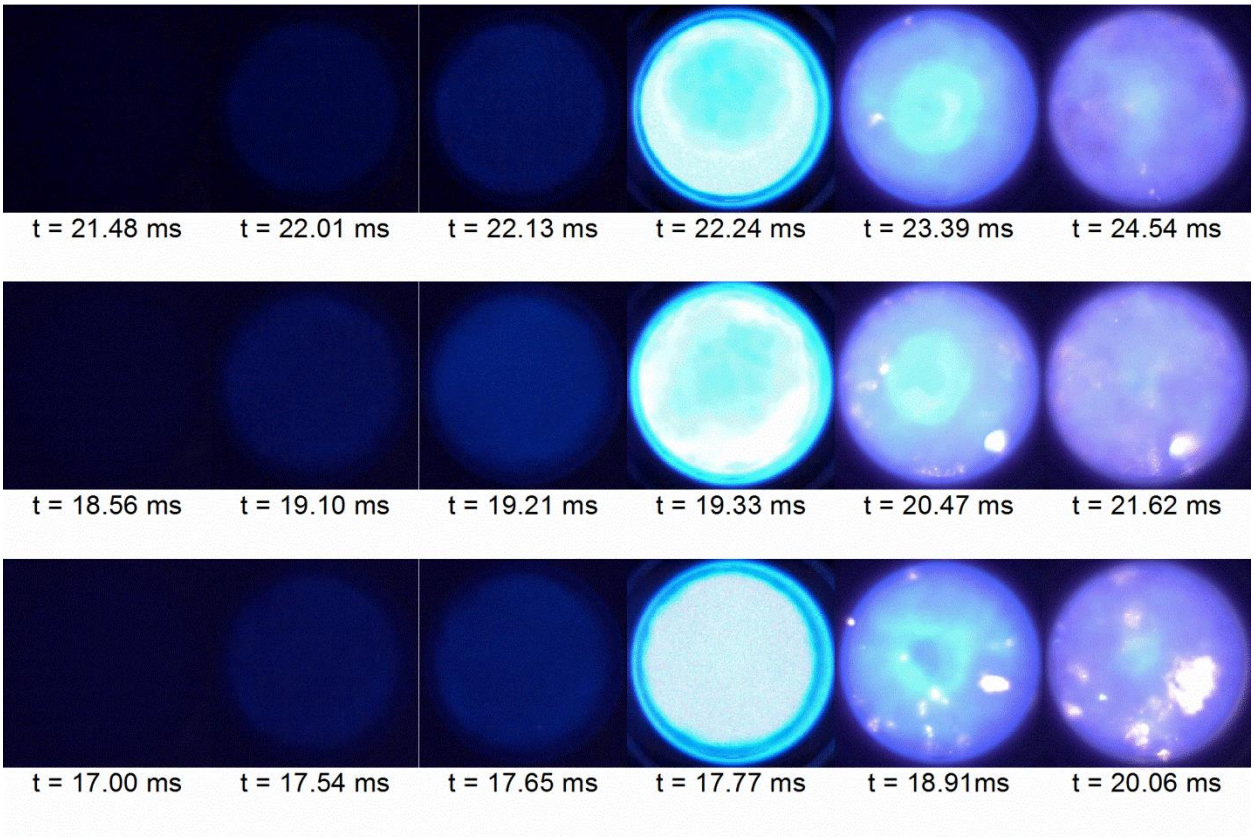

Figure 6-3. Typical still images from the high speed imaging of the UM RCF experiments presented in Figure 6-2. Row 1, 1-hexene. Row 2, *trans*-2-hexene. Row 3, *trans*-3-hexene.

A summary of the experimental ignition delay times for the three hexene isomers are presented in Figure 6-4 (Tables C-1, C-2, and C-3 provide the associated mixture compositions, thermodynamic state conditions, and ignition delay times). Experimental conditions for each fuel were fixed at a stoichiometric equivalence ratio ($\phi = 1$) and moderate dilution (buffer gas:$O_2 = 7.5$). Buffer gas composition was varied (Ar, CO_2, N_2) to refine the end of compression thermodynamic state conditions with negligible effect on the ignition delay times measured [24,119]. Data from this study span effective pressures of 10.5-12.1 atm (mean $P_{eff} = 11$ atm) and effective temperatures of 837-1086 K. The recommended uncertainty of ±20% in the ignition delay times is shown as the error bars in Figure 6-4 and is attributed primarily to the accuracy of the pressure transducer in the test section.

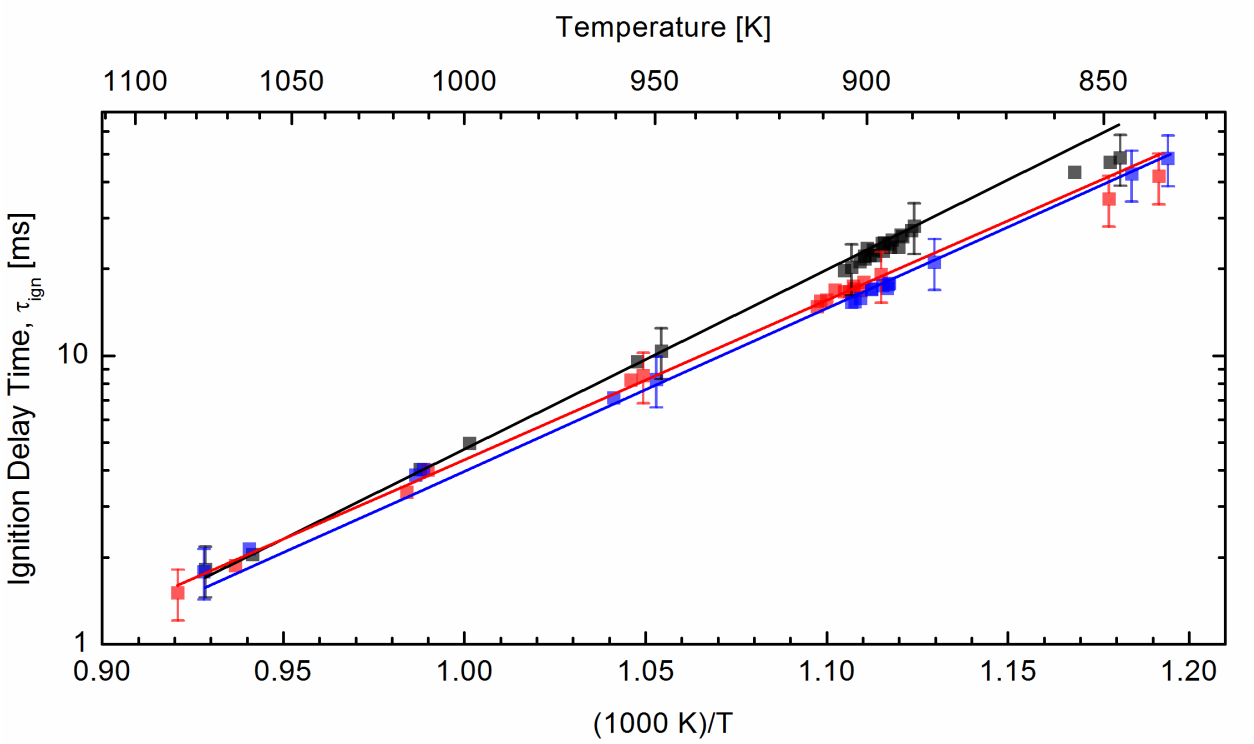

Figure 6-4. Arrhenius plots of the current UM RCF measurements of ignition delay times of 1-hexene (black symbols), *trans*-2-hexene (red symbols), and *trans*-3-hexene (blue symbols). Temperature dependent regressions of the experimental data are provided as lines. All experimental data have been normalized to conditions of buffer gas:O_2 = 7.5, and P = 11 atm.

The ignition delay times from the current work presented in Figure 6-4 highlight the similar activation energies and reactivity of the three hexene isomers at the conditions studied, where Arrhenius behavior was observed for temperatures above 875 K. The lowest temperature data (<875 K) show a small increase in reactivity and decrease in activation energy for 1-hexene and *trans*-2-hexene, consistent with theory and previous studies indicating the possible onset of non-Arrhenius behavior under these conditions. Regression correlations for the ignition delay times for each of the hexene isomers were calculated and are shown in Figure 6-4 as solid lines. Regression correlation parameters are provided in Table 6-2.

Table 6-2. Parameters for ignition delay regression correlations from the current study of 1-hexene, *trans*-2-hexene, and *trans*-3-hexene. Regression correlations are in the form of $\tau_{ign} = A \cdot \exp(E_a/\bar{R}T)$.

Fuel	A [ms]	E_a [cal/mol/K]
1-hexene	2.8e-6	28500
trans-2-hexene	1.3e-5	25200
trans-3-hexene	9.0e-6	25800

Due to differences in pressure and dilution ratio, comparisons of experimental data from different facilities benefit from scaling ignition delay times by $\tau ign \alpha P^{-1}$, $\tau ign \alpha$ buffer gas:O_2 . These scaling relationships are based on previous studies of *iso*-octane, *n*-heptane and *n*-butanol [24,86], and introduce some uncertainty in the comparisons, but are expected to be reasonable approximations for the hexene isomers. Presented in Figure 6-5 are stoichiometric (ϕ = 1) experimental data from the current study from Vanhove et al. [76], and from Mehl et al. [82], where the data from Mehl et al. [82] have been scaled to conditions of buffer gas:O_2 = 7.5 and P = 11 atm. CHEMKIN simulations (ϕ = 1, buffer gas:O_2 = 7.5, P = 11 atm) using the Mehl et al. [92] mechanism are presented in Figure 6-5 as solid lines. There is excellent agreement between the experimental data and simulation results. Differences in the agreement of experimental data near 850 K may be due effects from heat transfer, buffer gas composition, and weak ignition phenomena which can affect longer ignition delay times.

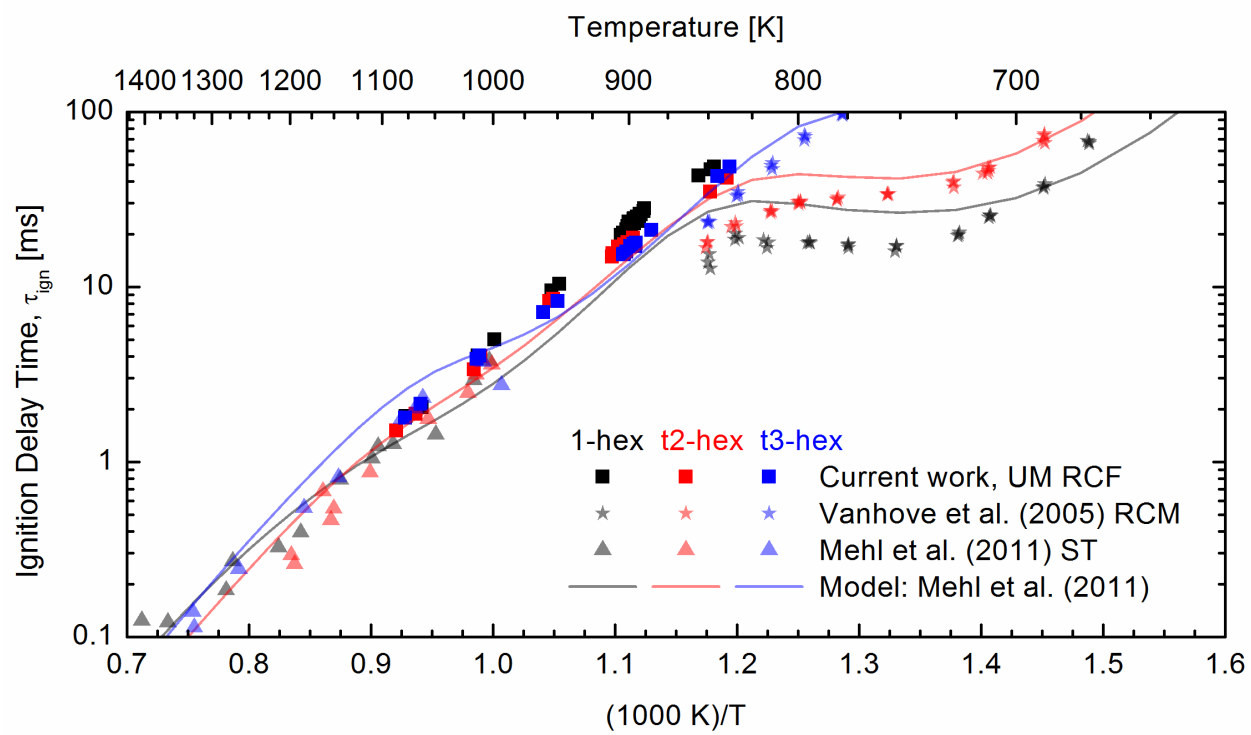

Figure 6-5. Arrhenius diagram of the UM RCF experimental data, experimental data from literature, and computed ignition delay times of the linear hexene isomers. All experimental data have been normalized to conditions of ϕ = 1, buffer gas:O_2 = 7.5, and P = 11 atm.

Intermediate Species

Results from the fast gas sampling for the three hexene fuels are shown in Figure 6-6, Figure 6-7, and Figure 6-8 . Additional stable intermediate species measurements are provided in Figure C-6. Presented in Figure 6-6 are the measured concentrations of the hexene fuels where the horizontal and vertical error bars represent the uncertainty in sample duration and timing (±1.2 ms) and measured concentration (±20%). The time scale in Figure 6-6 has been normalized such that end of compression corresponds to t/τ_{ign} = 0 and autoignition to t/τ_{ign} = 1 (the raw and normalized pressure time histories from the corresponding experiments are provided in Figure C-3, Figure C-4, and Figure C-5). The experimental data for the hexene fuels indicate that the rate of consumption is similar across all three isomers, with a rapid increase in the rate of consumption late in the ignition delay time (t/τ_{ign} > 0.9).

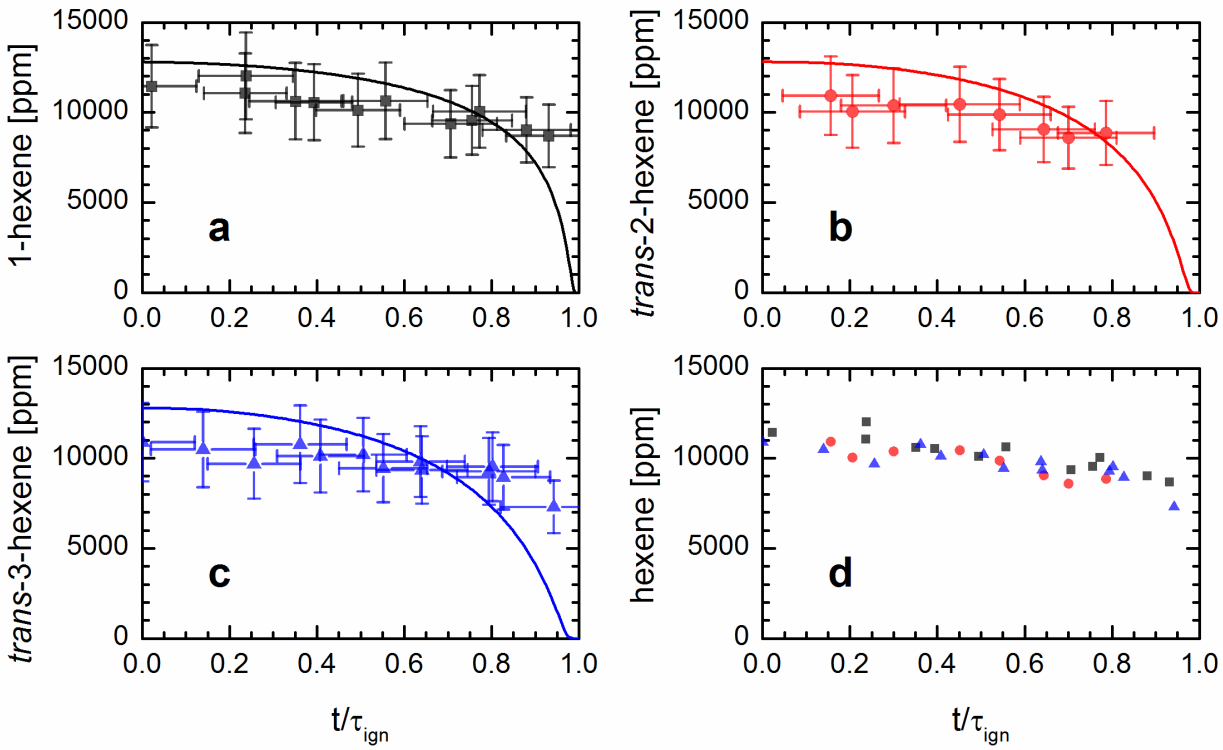

Figure 6-6. Hexene time histories for the three isomers during autoignition. a) 1-hexene, b) *trans*-2-hexene, c) *trans*-3-hexene, d) measured concentrations of the three hexene isomers. Experimental data from the UM RCF are shown as solid symbols and simulations with the Mehl et al. [92] mechanism are shown by the solid lines.

Model predictions are shown in Figure 6-6, Figure 6-7, and Figure 6-8 using the Mehl et al. [92] mechanism. A 0-D, isometric, adiabatic CHEMKIN simulation was used to model the experimental results, where initial conditions and compositions were the average conditions of the fast gas sampling experiments: 1-hexene (P_{eff} = 11.1 atm, T_{eff} = 896 K, ϕ = 1, $\chi(O_2)$ = 11.63%, buffer gas:O_2 = 7.5), *trans*-2-hexene (P_{eff} = 11.3 atm, T_{eff} = 905 K, ϕ = 1, $\chi(O_2)$ = 11.62%, buffer gas:O_2 = 7.5), and *trans*-3-hexene (P_{eff} = 11.2 atm, T_{eff} = 899 K, ϕ = 1, $\chi(O_2)$ = 11.63%, buffer gas:O2 = 7.5). Agreement between the experimental data and the model is excellent, and within 20% for the majority of the time history of the hexenes. At later times (t/τ_{ign}¬ > 0.9) during the ignition delay period, the model overpredicts the rate of consumption of *trans*-3-hexene. For the majority of the ignition delay

period (t/τ_{ign} < 0.9), the measured stable intermediate and hexene concentrations account for greater than 80% of the carbon initially in the test mixtures.

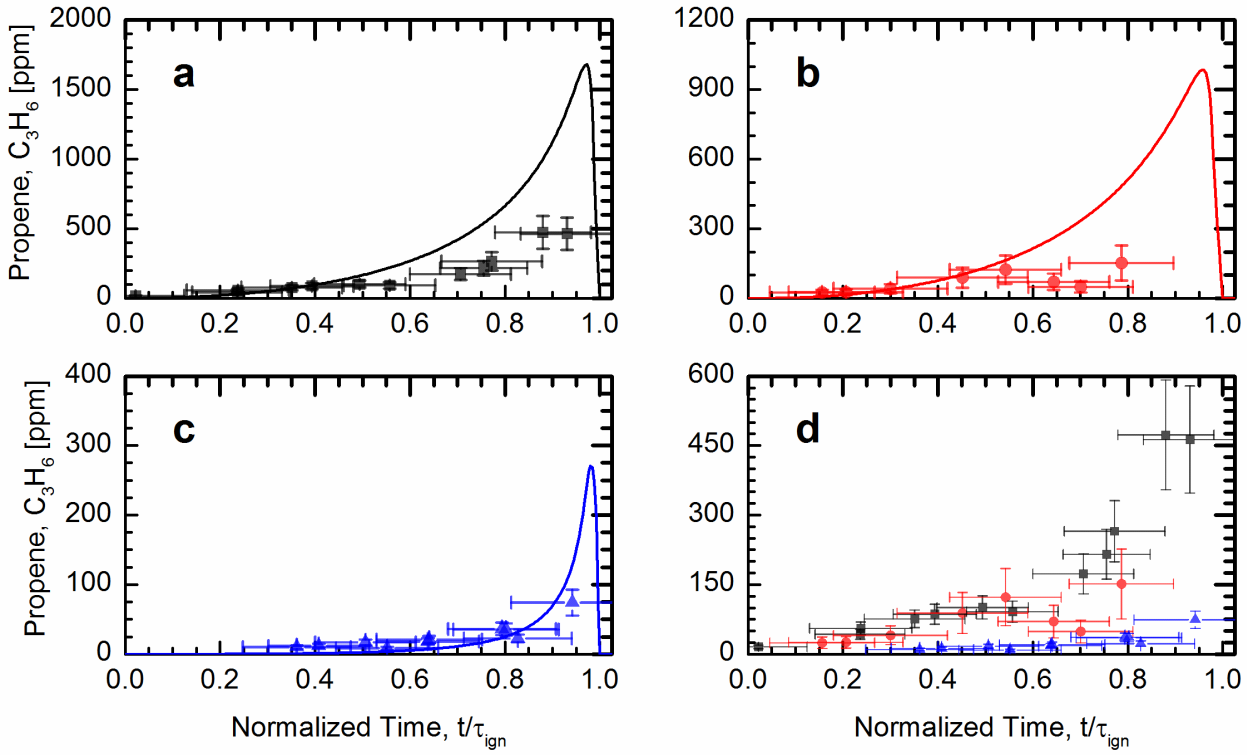

Figure 6-7. Propene (C_3H_6) time histories for the three isomers during autoignition. a) 1-hexene, b) *trans*-2-hexene, c) *trans*-3-hexene, d) measured concentrations for the three hexene isomers. Experimental data from the UM RCF are shown as solid symbols and simulations with the Mehl et al. [92] mechanism are shown by the solid lines.

Figure 6-7 shows the measurements of propene (C_3H_6) from the current work. The experimental measurements and Mehl et al. [92] mechanism simulation predictions of propene are in good agreement, within a factor of 3 for much of the ignition delay period. The experimental data also indicate that a longer alkyl chain promotes significantly increased propene production (a factor of ~5 increase in propene comparing *trans*-3-hexene and 1-hexene at t/τ_{ign} ~0.93), and this behavior is well predicted by the mechanism simulations.

The experimental measurements of propanal (C_2H_5CHO) from this study are provided in Figure 6-8. For 1-hexene and *trans*-2-hexene, the experimental data and the Mehl et al. [92] mechanism simulations are in excellent agreement, within

a factor of two. Unlike propene, the experimental measurements indicate propanal production decreases for the longer alkyl chain isomers and exhibits less sensitivity to the double bond position (a factor of ~2 decrease in propanal comparing *trans*-3-hexene and 1-hexene at t/τ_{ign} ~0.93). The mechanism simulations overpredict the experimental measurements of the current work by more than a factor of 10. The results presented in this study highlight the importance experimental measurements, such as stable intermediates, that provide valuable insight into reaction pathways. Additional experimental and computational studies of alkene chemistry are necessary to further understand the role of the double bond in combustion chemistry.

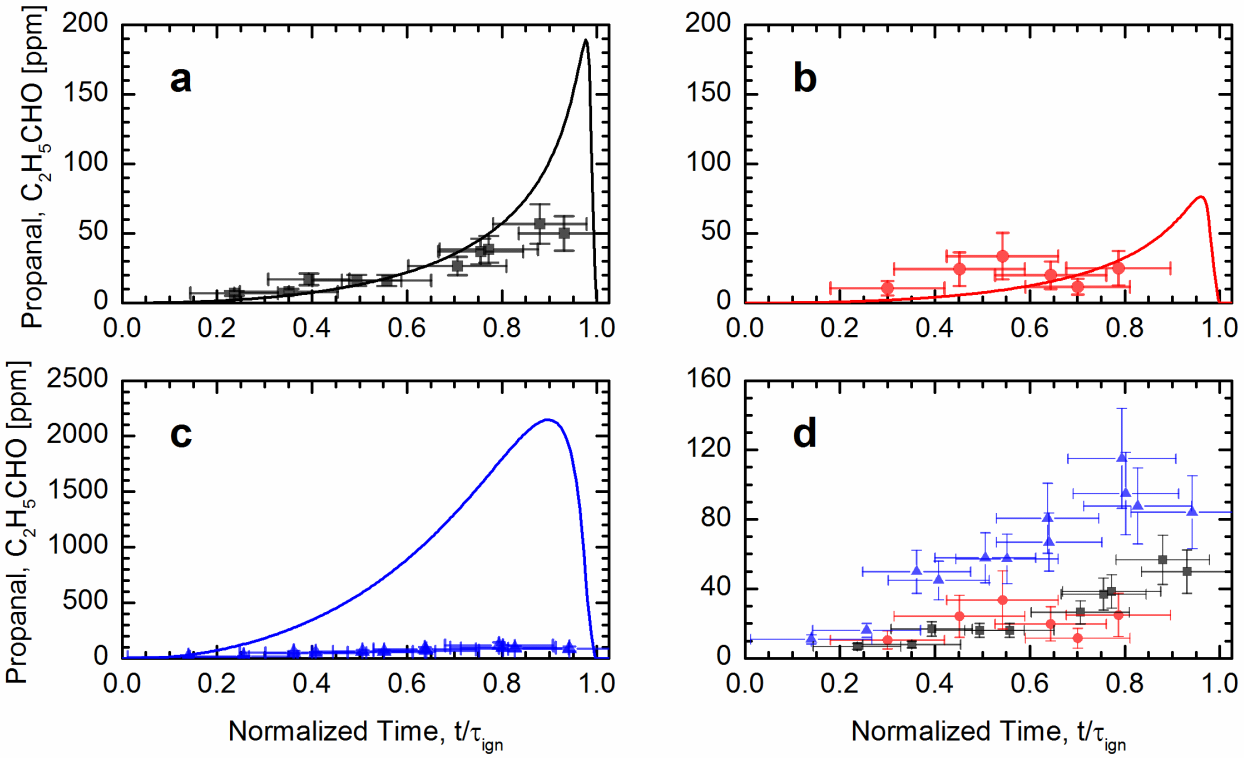

Figure 6-8. Propanal (C_2H_5CHO) time histories for the three isomers during autoignition. a) 1-hexene, b) *trans*-2-hexene, c) *trans*-3-hexene, d) measured concentrations for the three hexene isomers. Experimental data from the UM RCF are shown as solid symbols and simulations with the Mehl et al. [92] mechanism are shown by the solid lines.

6.5 Conclusions

New work compromising ignition delay times and stable intermediate species time histories of the three linear hexene isomers were presented in this study. The data provide greater insight into the role of the double bond, and its position, on combustion kinetics. Hexene ignition delay times from this study show that at higher temperatures the double bond position has negligible influence on the global chemical kinetics, while at lower temperatures the experimental data from the isomers with longer alkyl chains indicate the start of a relative increase in global reactivity and decrease in activation energy. The ignition delay results from this study are in excellent agreement with results from other experimental facilities and model predictions. Measurements of the three hexene fuels and their stable intermediates in this study indicate that the initial oxidation of the three hexene isomers proceed at similar rates until late in the ignition delay period ($t/\tau ign > 0.9$). Based on the measured species of this study (e.g., propene and propanal), the length of the alkyl chain also leads to differentiation in the stable intermediates produced and reaction pathways.

Chapter 7
Conclusions and Recommendations for Future Work

7.1 Conclusions

This thesis provides new understanding of the role of fuel chemistry at conditions relevant to advanced combustion strategies. Optically accessible facilities including a rapid compression machine and a shock tube were utilized in the technical approach to study global (e.g., ignition delay times) and detailed (e.g., stable intermediates, elementary reaction rates) combustion chemistry of several important fuel compounds. The data produced in this study are unique and led to new discoveries and unforeseen conclusions on the fuel chemistry of several important combustion species. The major findings of this thesis are provided below.

- Combustors that vary buffer gas composition (e.g., using dilution strategies such as exhaust gas recirculation) are likely sensitive to effects of the buffer gas composition on ignition timing at low pressures, high levels of dilution, and temperatures corresponding to non-Arrhenius conditions. In particular, fuels that exhibit multi-stage ignition are expected to be significantly more sensitive to buffer gas composition effects due to changes in thermochemical properties of the mixture. Additionally, internal combustion engines that operate with fixed ignition timing are expected to experience different heat release rates for faster ignition times based on the composition of the buffer gas utilized.

- Ignition delay measurements of methyl *trans*-3-hexenoate showed faster ignition delay times and suppression of non-Arrhenius behavior relative to saturated esters at comparable conditions. Measurements of the stable intermediates created during ignition of methyl *trans*-3-hexenoate highlighted uncertainties in unsaturated methyl ester reaction chemistry, namely the $R+O_2$ reaction rates and products of smaller unsaturated intermediates. The reaction rates of these species need further study, as discussed below.

- The reaction pathways of phenyl oxidation ($C_6H_5 + O_2$) were successfully interrogated with a laser schlieren technique at low pressures and high temperatures using a diaphragmless shock tube. The data presented are the first laser schlieren measurements of radical oxidation reactions. Phenyl oxidation rates were very sensitive to the initial dissociation of the precursor, while secondary reactions ($C_6H_5 + O \rightarrow c\text{-}C_5H_5 + CO$ and $c\text{-}C_5H_5 + O \rightarrow C_5H_4O + H$) were nearly as influential as the phenyl oxidation reactions on the measured rates. The results of the current work on phenyl oxidation provide a foundation for further shock tube studies which quantify important elementary reaction rates in the phenyl oxidation system and thereby inform future work on soot oxidation pathways.

- Autoignition timing of the three linear hexene compounds was largely insensitive to the double bond location at higher temperatures (> ~900 K) for the conditions studied. At lower temperatures (< ~900 K), the longer alkyl chain increased the reactivity and decreased the activation energy of the different isomers. Measured differentiation in the formation of stable intermediates (e.g., propene, propanal) was attributed to the position of the alkenyl group. At the conditions

studied, a longer alkyl chain suppressed formation of propanal and promoted production of propene.

7.2 Recommendations for Future Work

This thesis presented new experimental and computational results of kinetic studies on the role of fuel structures in combustion chemistry utilizing pressure-time histories, optical imaging, laser schlieren, and gas sampling of stable intermediates. Effects of buffer gas composition were investigated computationally and our understanding of dilution techniques (e.g., exhaust gas recirculation) would improve significantly if experimental measurements of ignition delay times could be obtained at the conditions identified as highly sensitive to buffer gas composition in the study (i.e., low pressure, high dilution, non-Arrhenius behavior). Changes in dilution and pressure have been found to be moderately well represented by proportional (dilution), and inversely proportional (pressure), relationships with ignition timing in regions of Arrhenius behavior. However, few studies have considered pressure and dilution effects at non-Arrhenius conditions. The development of alternative methods for analysis of two-stage and non-Arrhenius data would significantly enhance understanding of combustion chemistry, particularly for buffer gas composition where such effects are likely strongest.

Also in this work, laser schlieren was successfully applied to the phenyl oxidation system. Additional diagnostic techniques, such as time of flight mass spectroscopy (TOF-MS), to measure intermediates can be utilized to reduce uncertainties associated with mechanisms generated from laser schlieren data. Additionally, theoretical studies of thermochemical properties for species and reaction rates have provided new insights into combustion chemistry that complement the experimental laser schlieren measurements. Laser schlieren measurements of other classes of oxidation reactions (e.g., heptyl radicals + O_2) would provide a greater understanding to pathways that are important in low temperature combustion strategies.

There are some features of the experimental facility that could be improved or enhanced. The effects of the double bonds in fuels were studied at moderate pressures and temperatures. In the case of methyl *trans*-3-hexenoate, some stable intermediates could not be identified and/or quantified and understanding of ester reaction pathways would benefit from additional diagnostics/methods that can determine the molecular composition of unstable radical and stable intermediates. Also in the ester study, a reliable calibration could not be obtained for the high concentration of fuel used and consequently a lower fuel concentration was selected for the hexene study. Future studies of stable intermediates and their associated reaction pathways would be enhanced by the ability to resolve high concentrations of initial fuel and would improve signal to noise ratios of the stable intermediates. Experiments in the University of Michigan rapid compression facility are time consuming and difficult and simultaneous end wall imaging and gas sampling from the circumference would improve the efficiency of the experiments as well as provide insight into the thermal/fluid/kinetic interactions that take place in kinetic facilities.

Lastly, this work has highlighted uncertainties and sensitivities of classes of reactions, in particular small hydrocarbon chemistry. For example, significant concentrations of ethyne were predicted for the methyl *trans*-3-hexenoate, yet ethyne was below the detectible limit in the experimental measurements (< 10 ppm). Additional studies of alkenes even smaller than the C_6 species studied here are merited. Further, there is opportunity to design experiments at conditions accessible to the RCF to study elementary rate coefficients of important combustion reactions at low temperatures and moderate to high pressures, thus bridging the gap between the state conditions accessible to other reactor studies like flow reactors and shock tubes.

Appendix A

Effects of Buffer Gas Composition on Autoignition

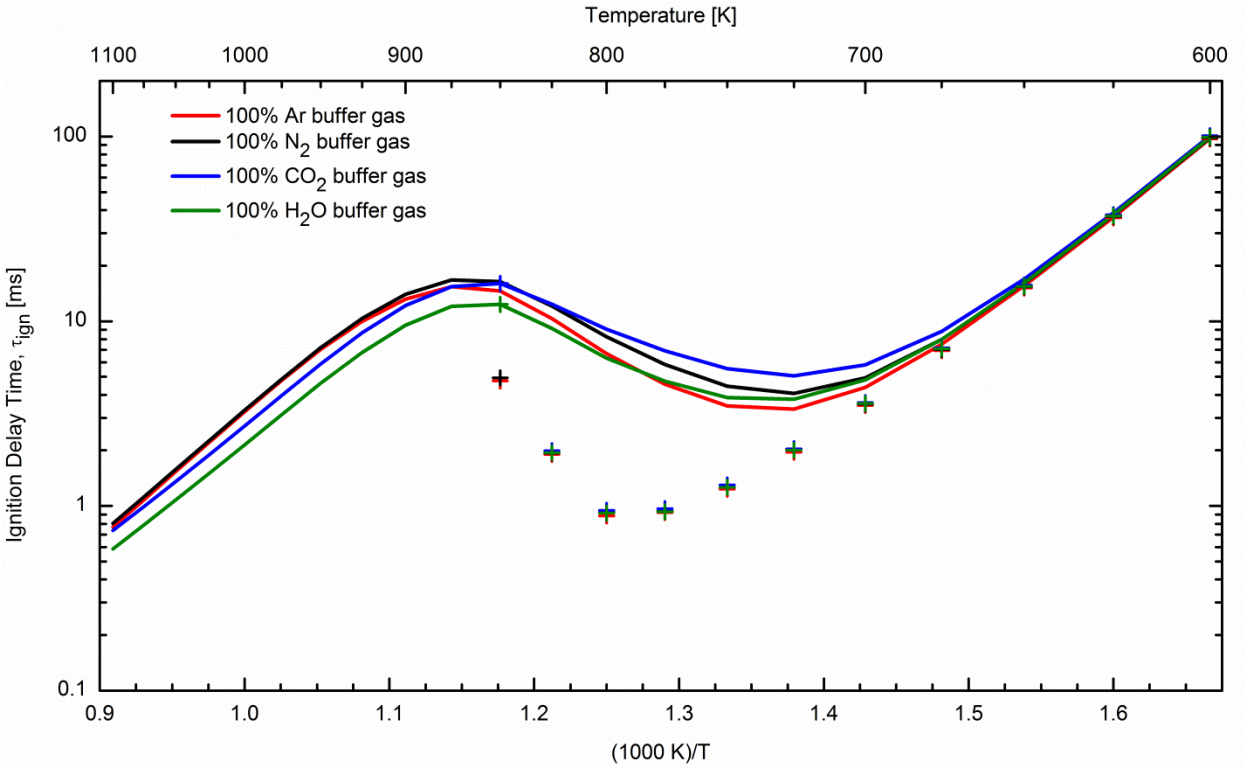

Figure A-1. Arrhenius diagram for computed ignition delay times of *n*-heptane. For conditions where two stages of ignition were observed, the + symbols indicate the computed first stage ignition delay times. Initial conditions of P = 9.0 atm, *n*-C_7H_{16} = 1.87%, O_2 = 20.61%, buffer gas = 77.52% (mole basis).

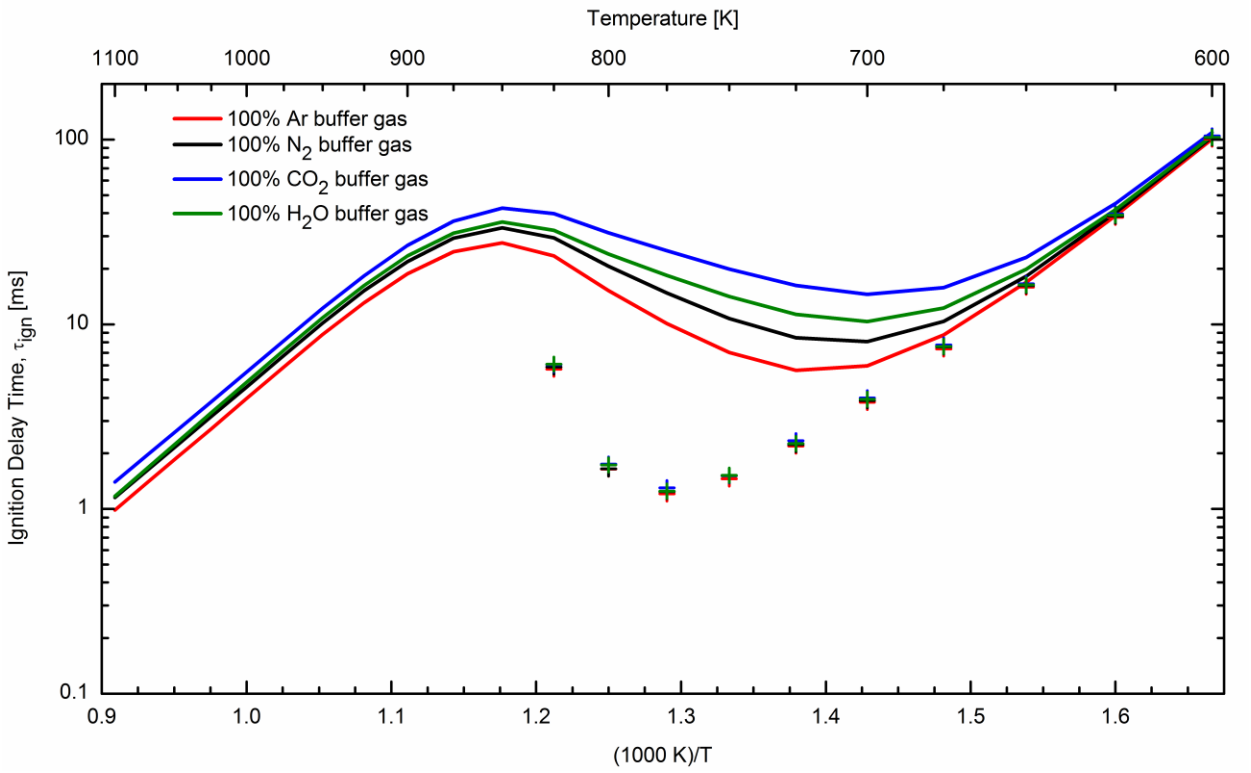

Figure A-2. Arrhenius diagram for computed ignition delay times of *n*-heptane. For conditions where two stages of ignition were observed, the + symbols indicate the computed first stage ignition delay times. Initial conditions of P = 9.0 atm, *n*-C_7H_{16} = 1.34%, O_2 = 14.90%, buffer gas = 83.76% (mole basis). All third-body collision efficiencies were set to 1, the collision efficiency of nitrogen.

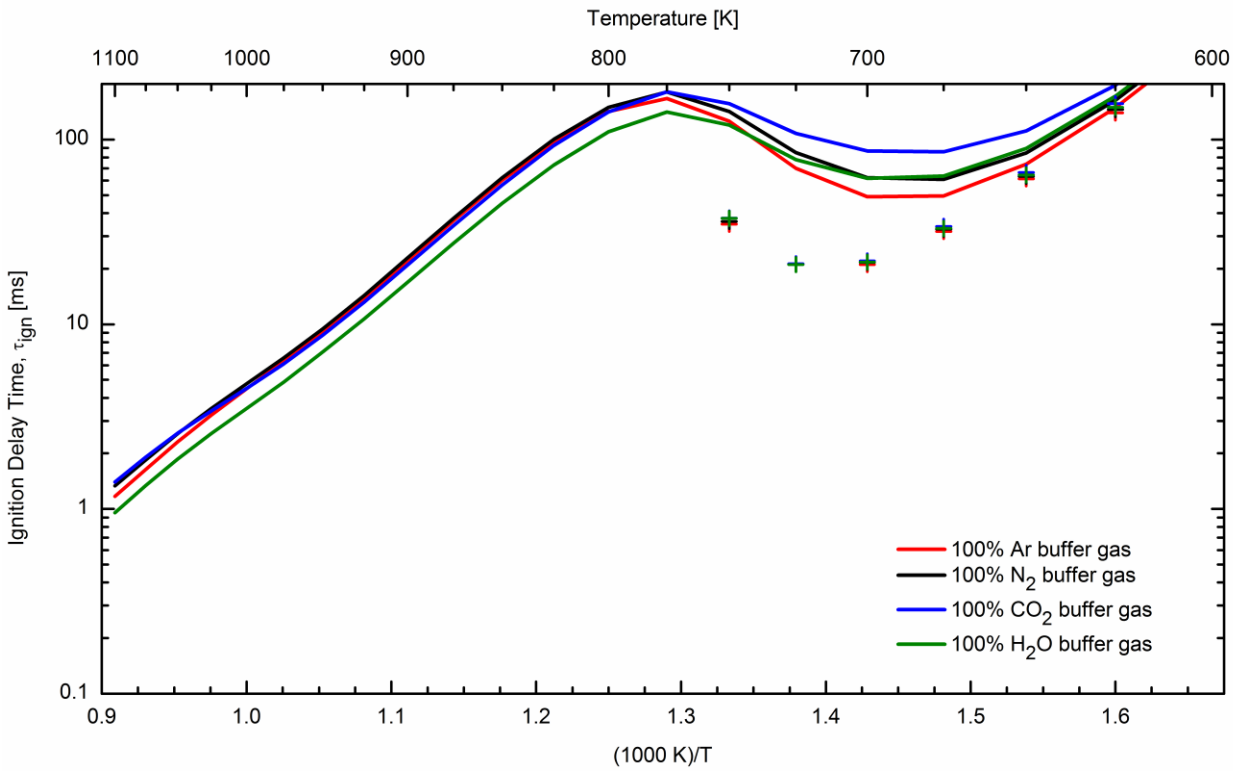

Figure A-3. Arrhenius diagram for computed ignition delay times of *iso*-octane. For conditions where two stages of ignition were observed, the + symbols indicate the computed first stage ignition delay times. Initial conditions of P = 9.0 atm, *i*-C_8H_{18} = 1.65%, O_2 = 20.66%, buffer gas = 77.69% (mole basis).

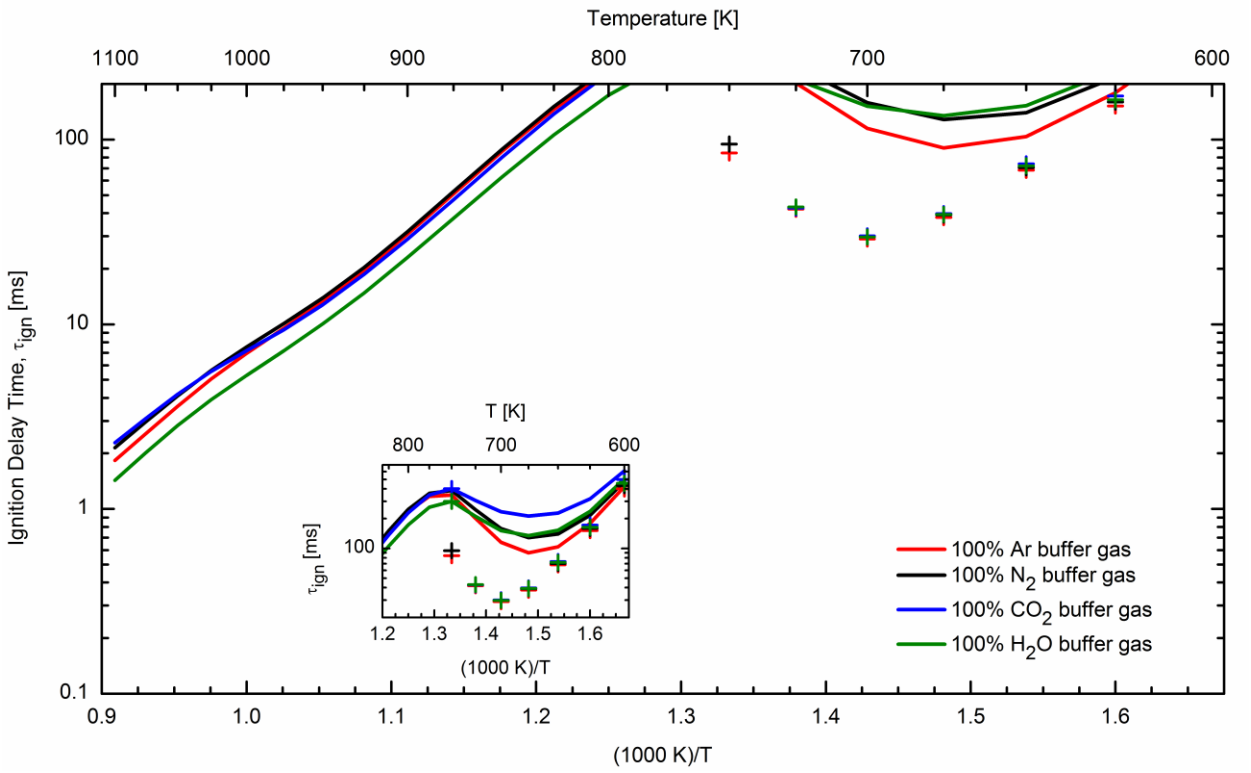

Figure A-4. Arrhenius diagram for computed ignition delay times of *iso*-octane. For conditions where two stages of ignition were observed, the + symbols indicate the computed first stage ignition delay times. Initial conditions of P = 9.0 atm, *i*-C_8H_{18} = 1.19%, O_2 = 14.88%, buffer gas = 83.93% (mole basis).

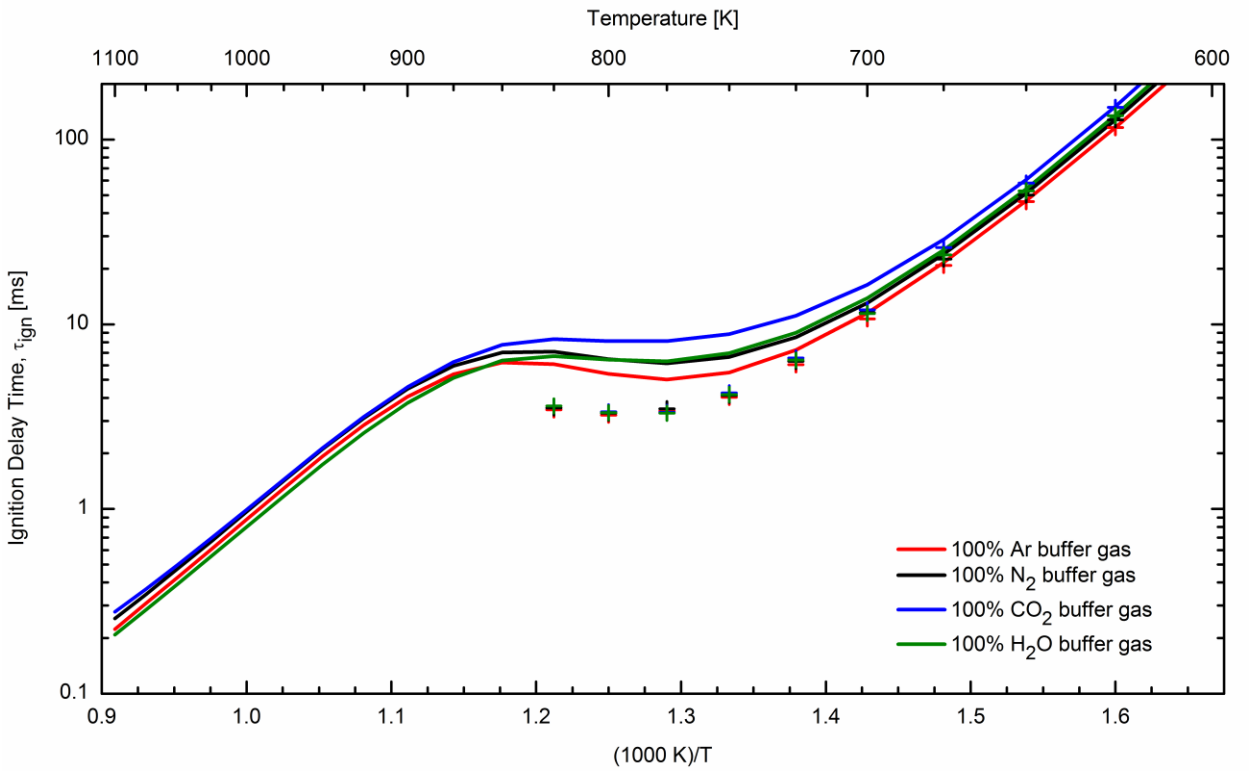

Figure A-5. Arrhenius diagram for computed ignition delay times of *iso*-octane. For conditions where two stages of ignition were observed, the + symbols indicate the computed first stage ignition delay times. Initial conditions of P = 60.0 atm, *i*-C_8H_{18} = 1.19%, O_2 = 14.88%, buffer gas = 83.93% (mole basis).

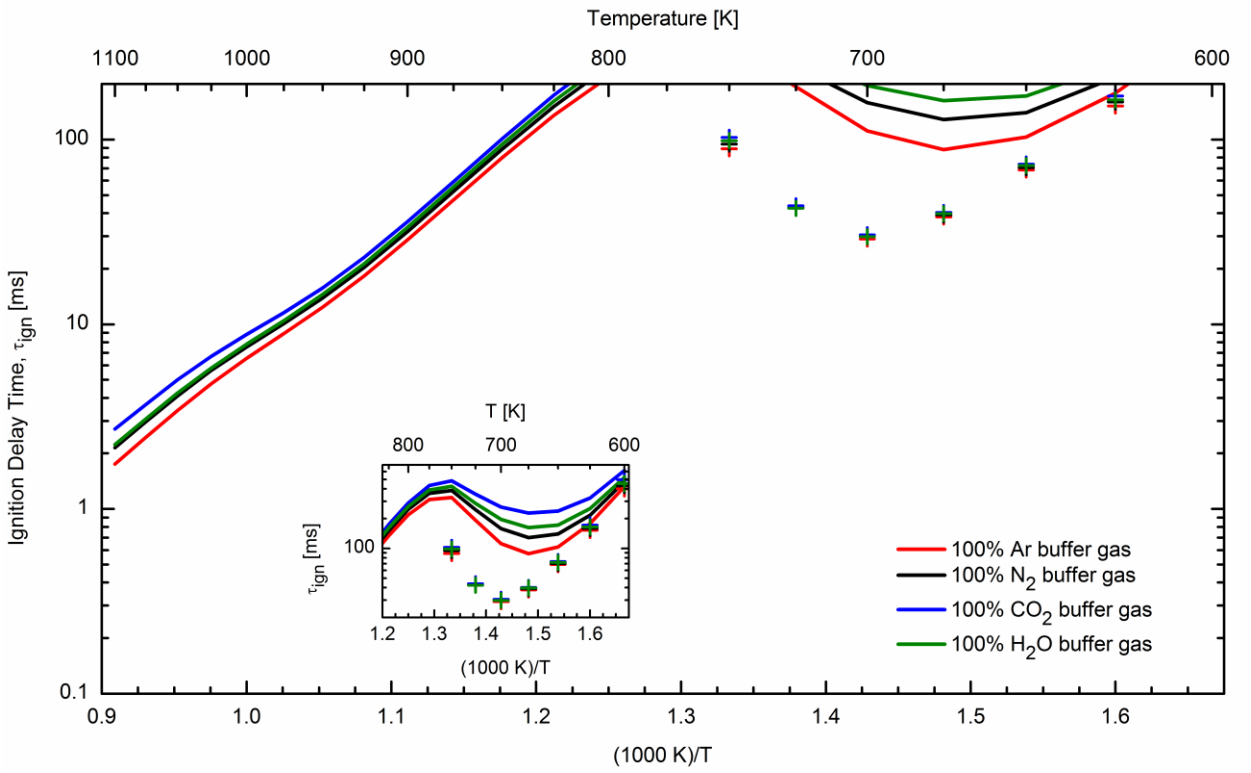

Figure A-6. Arrhenius diagram for computed ignition delay times of *iso*-octane. For conditions where two stages of ignition were observed, the + symbols indicate the computed first stage ignition delay times. Initial conditions of P = 9.0 atm, *i*-C_8H_{18} = 1.19%, O_2 = 14.88%, buffer gas = 83.93% (mole basis). All third-body collision efficiencies were set to 1, the collision efficiency of nitrogen.

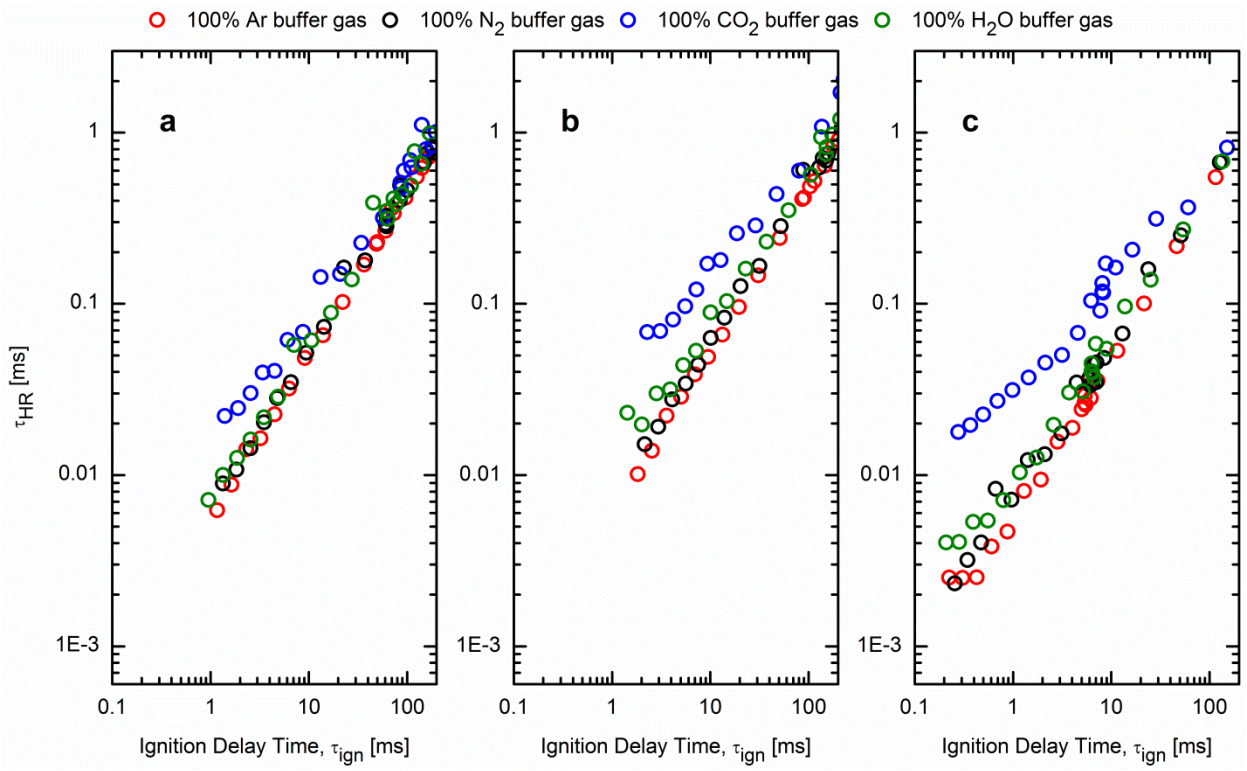

Figure A-7. Simulation results for characteristic times of heat release as a function of ignition delay time for stoichiometric *iso*-octane mixtures at initial conditions of: (a) P = 9.0 atm, buffer gas:O_2 = 3.76, (b) P = 9.0 atm, buffer gas:O_2 = 5.64, (c) P = 60.0 atm, buffer gas:O_2 = 5.64.

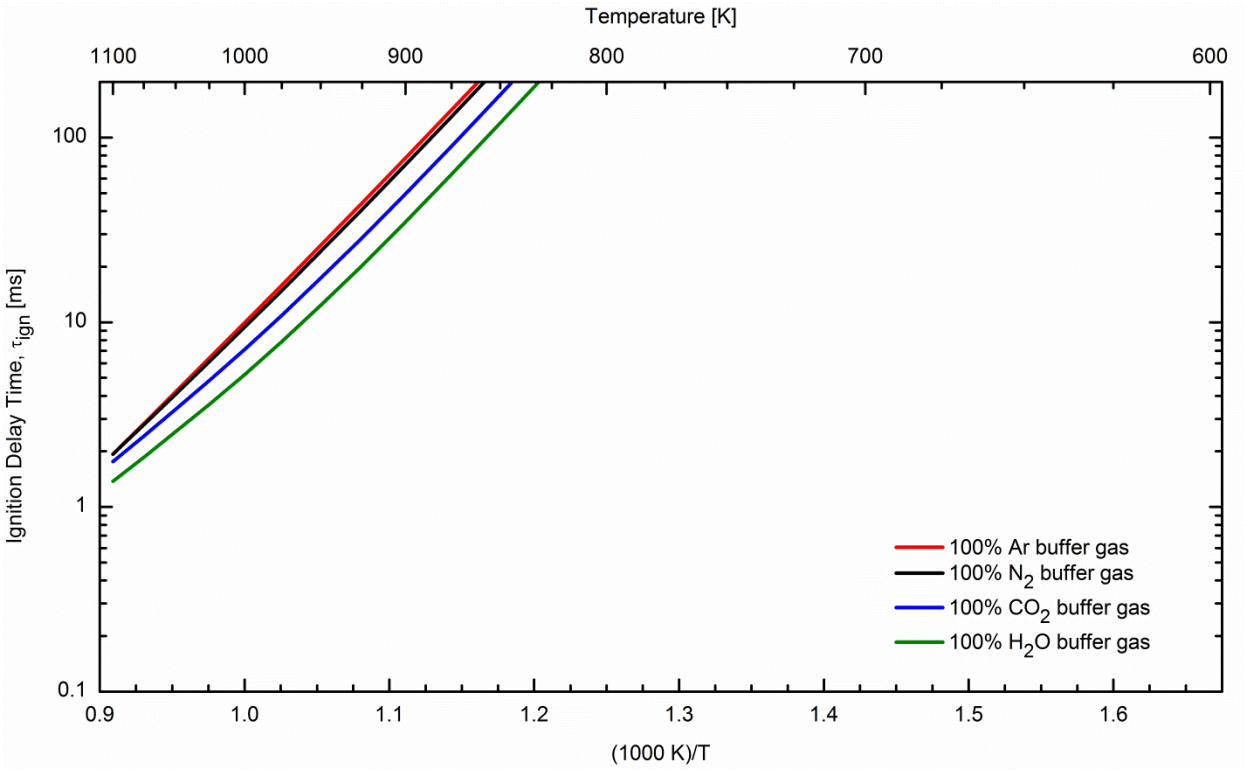

Figure A-8. Arrhenius diagram for computed ignition delay times of *n*-butanol. Initial conditions of P = 3.2 atm, *n*-C_4H_9OH = 3.38%, O_2 = 20.30%, buffer gas = 76.32% (mole basis).

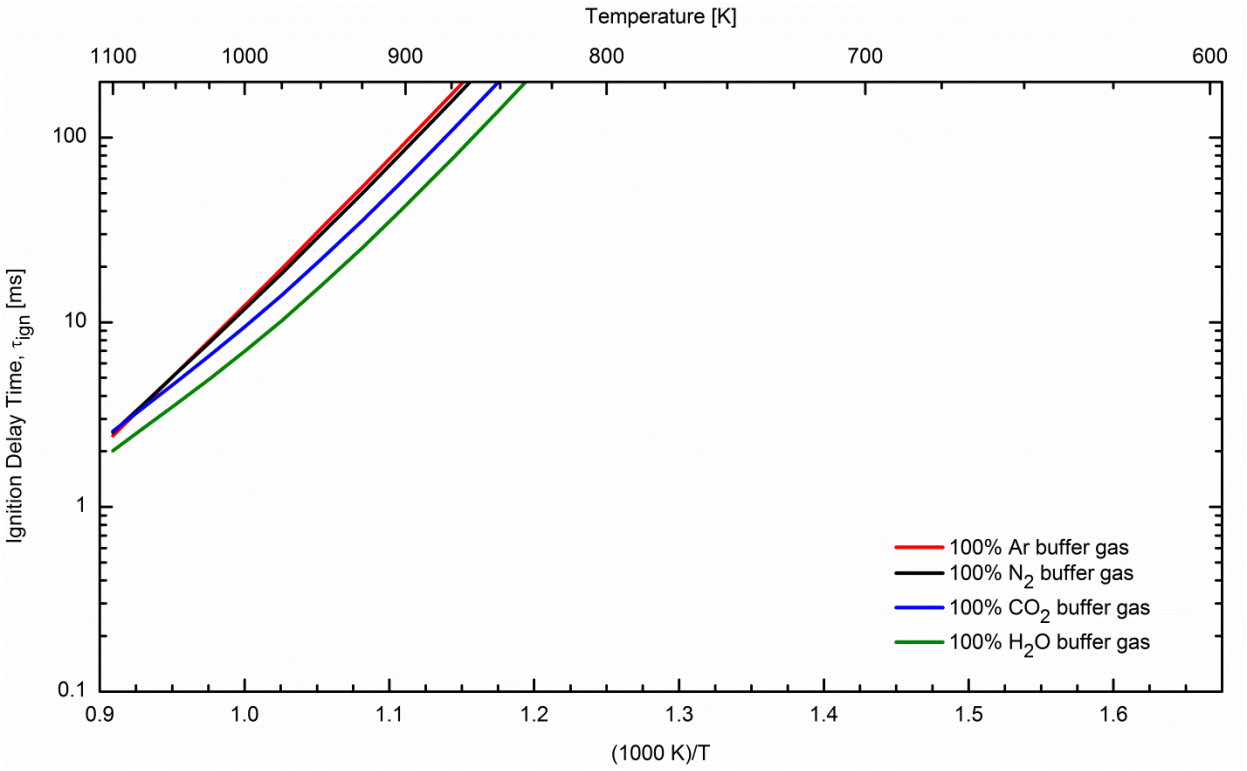

Figure A-9. Arrhenius diagram for computed ignition delay times of *n*-butanol. Initial conditions of P = 3.2 atm, *n*-C_4H_9OH = 2.45%, O_2 = 14.71%, buffer gas = 82.84% (mole basis).

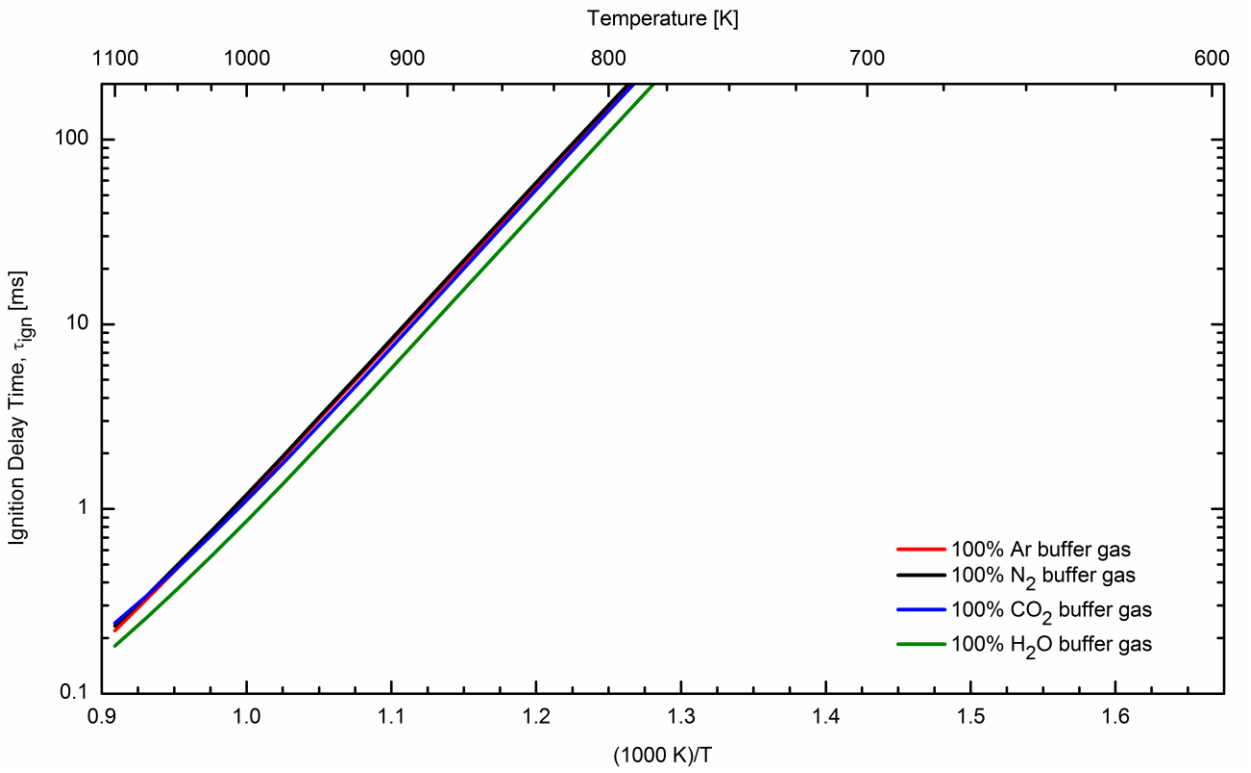

Figure A-10. Arrhenius diagram for computed ignition delay times of *n*-butanol. Initial conditions of P = 60.0 atm, *n*-C_4H_9OH = 2.45%, O_2 = 14.71%, buffer gas = 82.84% (mole basis).

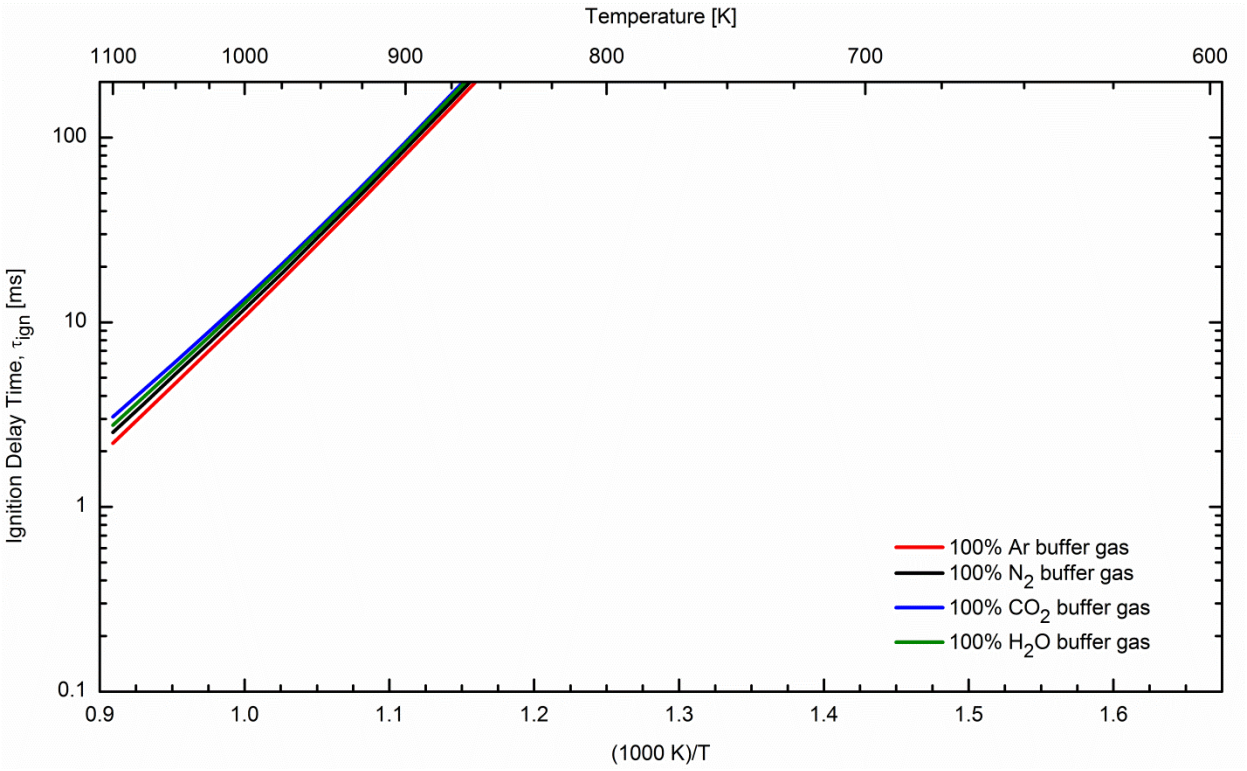

Figure A-11. Arrhenius diagram for computed ignition delay times of *n*-butanol. Initial conditions of P = 3.2 atm, *n*-C_4H_9OH = 2.45%, O_2 = 14.71%, buffer gas = 82.84% (mole basis). All third-body collision efficiencies were set to 1, the collision efficiency of nitrogen.

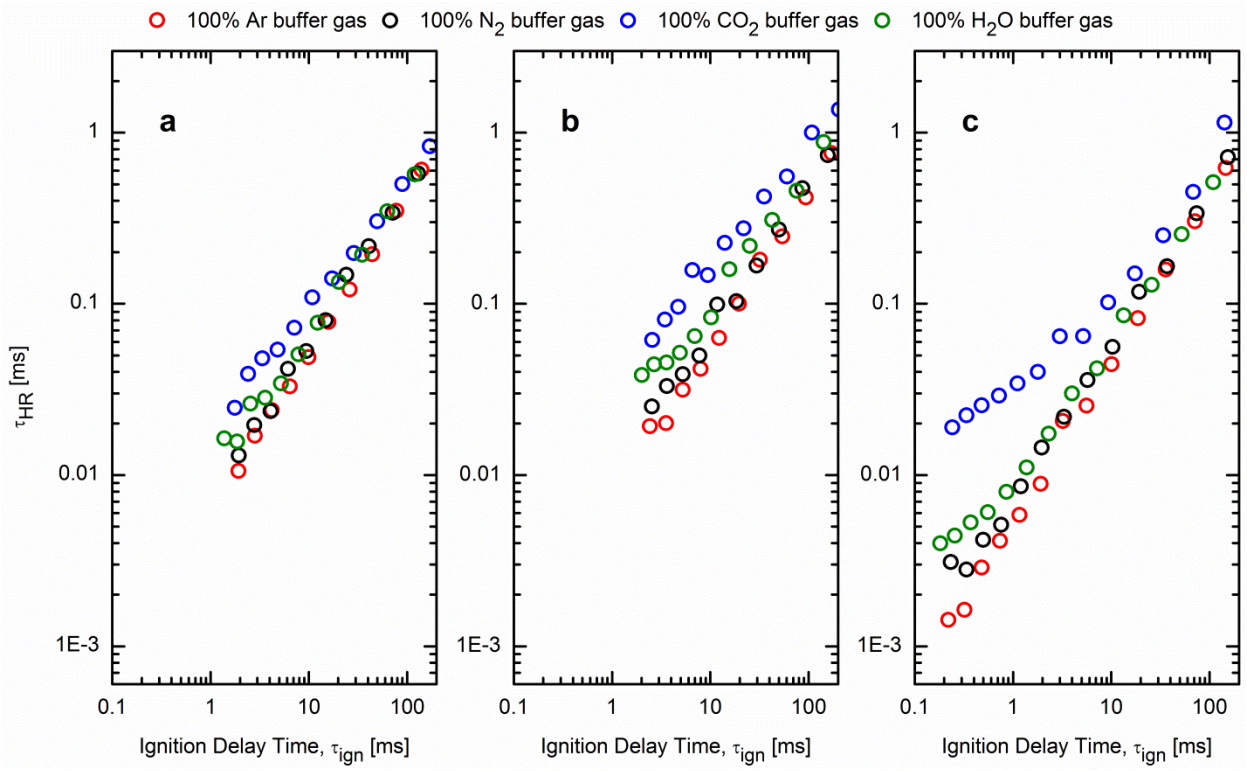

Figure A-12. Simulation results for characteristic times of heat release as a function of ignition delay time for stoichiometric *n*-butanol mixtures at initial conditions of: (a) P = 3.2 atm, buffer gas:O_2 = 3.76, (b) P = 3.2 atm, buffer gas:O_2 = 5.63, (c) P = 60.0 atm, buffer gas:O_2 = 5.63.

Appendix B

Phenyl Oxidation Thermochemistry

Table B-1. Thermochemical properties for phenyl oxidation mechanism.[a]

Species	$\Delta H_{f,298K}$ [cal/mol]	$H_{298K}-H_{0K}$ [cal/mol]	T_{low} [K]	T_{high} [K]	c_0	c_1	c_2	c_3	c_4	d
Kr	0.000e0	1.481e3	1000	5000	2.499e0	6.396e0	-2.023e4	2.504e07	-1.091e10	4.385e0
C_6H_5	8.059e4	3.391e3	500	3000	3.108e1	-2.754e4	1.509e7	-4.787e09	6.603e11	-1.644e2
C_6H_5I	3.894e4	4.323e3	500	3000	3.407e1	-2.826e4	1.518e7	-4.758e09	6.500e11	-1.764e2
$C_{12}H_{10}$	4.357e4	5.832e3	500	3000	6.408e1	-5.939e4	3.516e7	-1.235e10	1.873e12	-3.650e2
I	2.515e4	1.481e3	300	2000	2.828e0	-1.533e3	2.707e6	-2.121e9	6.193e11	4.831e0
o-C_6H_4	1.103e5	3.423e3	300	2000	2.824e1	-2.426e4	1.362e7	-4.518e9	6.534e11	-1.460e2
H	5.210e4	1.481e3	500	3000	2.499e0	6.476e0	-1.037e4	6.717e6	-4.890e08	-4.352e1
C_6H_6	1.989e4	3.393e3	500	4500	3.407e1	-3.156e4	1.759e7	-5.597e9	7.690e11	-1.871e2
H_2	0.000e0	2.024e3	500	3000	4.581e0	-3.018e3	3.174e6	-1.493e9	2.597e11	-1.244e1
C_4H_2	1.096e5	3.426e3	800	2500	1.662e1	-1.206e4	7.913e6	-3.038e9	4.768e11	-7.345e1
C_2H_2	5.457e4	2.393e3	500	3000	1.096e1	-9.759e3	7.559e6	-3.134e9	5.143e11	-4.544e1
HI	6.348e3	2.069e3	500	3000	4.712e0	-2.244e3	1.717e6	-6.342e8	9.304e10	-3.778e0
C_6H_5O	1.471e4	4.034e3	500	3000	3.448e1	-2.933e4	1.788e7	-6.361e9	9.768e11	-1.825e2
c-C_5H_5	6.292e4	3.622e3	500	3000	2.833e1	-2.653e4	1.711e7	-6.377e9	1.000e12	-1.460e2

CO	-2.642e4	2.072e3	500	3000	4.608e0	-1.959e3	1.452e6	-5.282e8	7.759e10	-4.056e0
C_3H_3	8.401e4	3.255e3	500	3000	1.615e1	-1.313e4	8.957e6	-3.424e9	5.340e11	-7.101e1
C_4H	1.932e5	4.371e3	500	3000	1.360e1	-8.809e3	5.632e6	-2.126e9	3.296e11	-5.189e1
C_4	2.471e5	3.135e3	500	3000	1.189e1	-9.336e3	7.241e6	-2.956e9	4.744e11	-3.928e1
C_2H	1.359e5	2.523e3	500	3000	8.010e0	-5.457e3	3.975e6	-1.467e9	2.117e11	-2.406e1
C_8H_6	7.843e6	3.990e3	500	3000	4.057e1	-3.675e4	2.195e7	-7.857e9	1.203e12	-2.200e2
H_2O	-5.780e4	2.374e3	500	3000	7.334e0	-7.547e3	7.214e6	-3.228e9	5.491e11	-2.454e1
HO_2	2.939e3	2.391e3	500	3000	7.623e0	-6.557e3	5.898e6	-2.676e9	4.702e11	-2.068e1
p-$C_6H_4O_2$	-2.903e4	4.502e3	500	3000	3.446e1	-2.928e4	1.744e7	-6.181e9	9.455e11	-1.808e2
H_2O_2	-3.248e4	2.668e3	500	3000	9.984e0	-8.508e3	6.811e6	-2.868e9	4.789e11	-3.505e1
O	5.955e4	1.607e3	500	3000	2.509e0	7.743e1	3.206e4	-2.784e7	5.783e9	5.135e0
O_2	0.000e0	2.075e3	500	3000	4.919e0	-2.595e3	2.338e6	-1.084e9	1.965e11	-5.277e0
OH	8.915e3	2.106e3	500	3000	4.646e0	-2.966e3	3.065e6	-1.411e9	2.418e11	-6.439e0
C_5H_4O	1.320e4	3.575e3	500	3000	2.840e1	-2.626e4	1.638e7	-5.908e9	9.029e11	-1.474e2
c-C_5H_6	3.210e4	3.235e3	500	3000	3.149e1	-3.497e4	1.937e7	-6.995e9	1.073e12	-1.709e2

[a] $[H°(T)-H°(0)]/RT = c_0 + c_1/T + c_2/T^2 + c_3/T^3 + c_4/T^4$

[a] $-[G°(T)-G°(0)]/RT = c_0(1-\ln(T)) + c_1/T + c_2/(2T^2) + c_3/(3T^3) + c_4/(4T^4) - d$

Appendix C

Linear Hexene Isomer Supporting Information

Table C-1. Summary of experimental conditions and results for 1-hexene autoignition. All mixture data are provided on a mole fraction basis.

ϕ	Inert:O_2	Test Gas Composition					P_{eff}	T_{eff}	τ_{ign}
		$\chi(1\text{-}C_6H_{12})$ [%]	$\chi(O_2)$ [%]	$\chi(N_2)$ [%]	$\chi(Ar)$ [%]	$\chi(CO_2)$ [%]	[atm]	[K]	[ms]
0.99	7.50	1.28	11.61	67.65	0.00	19.45	10.8	847	49.2
0.99	7.50	1.28	11.61	67.65	0.00	19.45	11.0	849	46.5
0.99	7.49	1.28	11.62	67.66	0.00	19.43	11.4	856	41.3
0.99	7.50	1.28	11.62	82.63	0.00	4.46	10.5	890	29.3
0.99	7.49	1.28	11.62	79.92	0.00	7.17	11.0	890	27.1
0.99	7.49	1.28	11.63	82.63	0.01	4.46	10.8	892	26.2[a]
0.99	7.51	1.28	11.61	82.64	0.00	4.47	11.0	892	26.1
0.99	7.50	1.28	11.62	82.63	0.00	4.47	10.9	893	23.9[a]
0.99	7.50	1.28	11.62	82.63	0.00	4.47	11.0	894	25.1[a]
0.99	7.47	1.28	11.65	82.62	0.01	4.44	11.0	895	23.6[a]
0.99	7.50	1.28	11.62	82.64	0.00	4.46	11.0	895	24.2[a]
0.99	7.50	1.28	11.61	82.64	0.00	4.47	10.6	896	25.4
0.99	7.50	1.28	11.61	82.63	0.00	4.47	11.2	896	22.5[a]
0.99	7.46	1.28	11.67	78.24	0.00	8.80	10.5	897	25.4
0.99	7.50	1.28	11.62	82.64	0.00	4.46	11.2	898	21.7[a]
0.99	7.49	1.28	11.63	82.62	0.00	4.46	11.1	899	22.8[a]
0.99	7.49	1.28	11.62	82.62	0.00	4.47	11.2	899	21.7[a]
0.99	7.50	1.28	11.62	78.26	0.00	8.84	10.8	900	22.5
0.99	7.49	1.28	11.62	82.63	0.00	4.46	11.0	900	23.5
1.00	7.51	1.28	11.60	82.63	0.00	4.48	11.2	900	21.3
0.99	7.50	1.28	11.62	82.63	0.00	4.47	11.3	901	20.5
0.99	7.50	1.28	11.62	82.64	0.00	4.46	11.5	903	19.3

0.99	7.49	1.28	11.62	82.63	0.00	4.47	11.5	905	18.7
0.99	7.49	1.28	11.63	87.08	0.00	0.00	10.9	948	10.4
0.99	7.49	1.28	11.63	87.08	0.00	0.00	11.1	954	9.4
0.99	7.49	1.28	11.62	74.65	12.44	0.00	10.7	999	5.1
0.99	7.49	1.28	11.62	74.65	12.44	0.00	11.4	1012	3.9
0.99	7.50	1.28	11.62	63.86	23.24	0.00	11.2	1062	2.0
0.99	7.49	1.28	11.62	63.87	23.22	0.00	11.8	1077	1.7

[a] Gas samples were acquired during the ignition delay period for analysis of stable intermediates.

Table C-2. Summary of experimental conditions and results for *trans*-2-hexene autoignition. All mixture data are provided on a mole fraction basis.

ϕ	Inert:O_2	Test Gas Composition					P_{eff}	T_{eff}	τ_{ign}
		$\chi(2\text{-}C_6H_{12})$ [%]	$\chi(O_2)$ [%]	$\chi(N_2)$ [%]	$\chi(Ar)$ [%]	$\chi(CO_2)$ [%]	[atm]	[K]	[ms]
0.99	7.50	1.28	11.61	67.50	0.00	19.60	10.5	839	43.5
0.99	7.47	1.28	11.66	67.55	0.01	19.51	11.1	849	34.5
0.99	7.50	1.28	11.62	78.10	0.00	9.00	10.8	897	19.4
0.99	7.49	1.28	11.62	78.10	0.00	9.00	10.9	901	16.8
0.99	7.49	1.28	11.62	82.49	0.00	4.61	11.3	901	17.5[a]
0.99	7.50	1.28	11.62	82.48	0.00	4.62	11.0	903	17.4[a]
0.99	7.49	1.28	11.63	82.48	0.00	4.61	11.4	903	16.4[a]
0.99	7.49	1.28	11.62	82.48	0.00	4.61	11.4	904	16.0
1.00	7.50	1.28	11.61	82.48	0.00	4.62	11.4	905	16.0[a]
0.99	7.50	1.28	11.62	82.48	0.00	4.62	11.3	907	16.4[a]
1.00	7.50	1.28	11.61	82.48	0.00	4.62	11.6	909	14.8
0.99	7.50	1.28	11.61	82.48	0.00	4.62	11.6	911	14.6
0.99	7.50	1.28	11.62	82.48	0.00	4.62	11.6	911	14.0[a]
0.99	7.49	1.28	11.62	86.94	0.00	0.15	10.9	953	8.6
0.99	7.49	1.28	11.63	86.94	0.01	0.15	11.1	956	8.1
0.99	7.50	1.28	11.62	74.89	12.21	0.00	11.3	1010	3.9
0.99	7.50	1.28	11.62	74.89	12.21	0.00	11.6	1016	3.2
0.99	7.49	1.28	11.62	64.09	23.00	0.00	11.4	1067	1.8
0.99	7.50	1.28	11.62	64.08	23.02	0.00	12.1	1086	1.4

[a] Gas samples were acquired during the ignition delay period for analysis of stable intermediates.

Table C-3. Summary of experimental conditions and results for *trans*-3-hexene autoignition. All mixture data are provided on a mole fraction basis.

ϕ	Inert:O_2	Test Gas Composition					P_{eff}	T_{eff}	τ_{ign}
		$\chi(3\text{-}C_6H_{12})$ [%]	$\chi(O_2)$ [%]	$\chi(N_2)$ [%]	$\chi(Ar)$ [%]	$\chi(CO_2)$ [%]	[atm]	[K]	[ms]
0.99	7.49	1.28	11.63	67.52	0.01	19.56	10.5	837	50.2
0.99	7.49	1.28	11.63	67.52	0.00	19.57	10.8	844	43.1
0.99	7.49	1.28	11.62	82.49	0.00	4.61	10.5	885	22.1
0.99	7.50	1.28	11.62	82.48	0.00	4.62	11.0	895	17.8[a]
0.99	7.48	1.28	11.64	82.47	0.01	4.61	11.0	895	17.6[a]
0.99	7.50	1.28	11.62	82.49	0.00	4.61	11.0	895	17.0[a]
1.00	7.51	1.28	11.61	78.10	0.00	9.01	10.8	896	17.9
0.99	7.49	1.28	11.63	82.48	0.00	4.61	11.1	899	16.7[a]
0.99	7.47	1.28	11.66	82.48	0.00	4.58	11.2	899	16.7[a]
0.99	7.49	1.28	11.62	78.10	0.00	8.99	11.0	901	15.7
0.99	7.49	1.28	11.62	82.48	0.00	4.61	11.4	903	14.8[a]
0.99	7.49	1.28	11.63	82.48	0.01	4.60	11.4	903	14.6[a]
0.99	7.49	1.28	11.63	86.95	0.00	0.14	10.8	950	8.4
0.99	7.50	1.28	11.61	86.96	0.00	0.14	11.3	960	6.9
1.00	7.50	1.28	11.61	74.87	12.23	0.00	11.3	1011	3.9
0.99	7.47	1.28	11.65	74.89	12.18	0.00	11.4	1014	3.7
0.99	7.50	1.28	11.62	64.08	23.02	0.00	11.2	1063	2.1
0.99	7.49	1.28	11.63	64.10	23.00	0.00	11.9	1077	1.6

[a] Gas samples were acquired during the ignition delay period for analysis of stable intermediates.

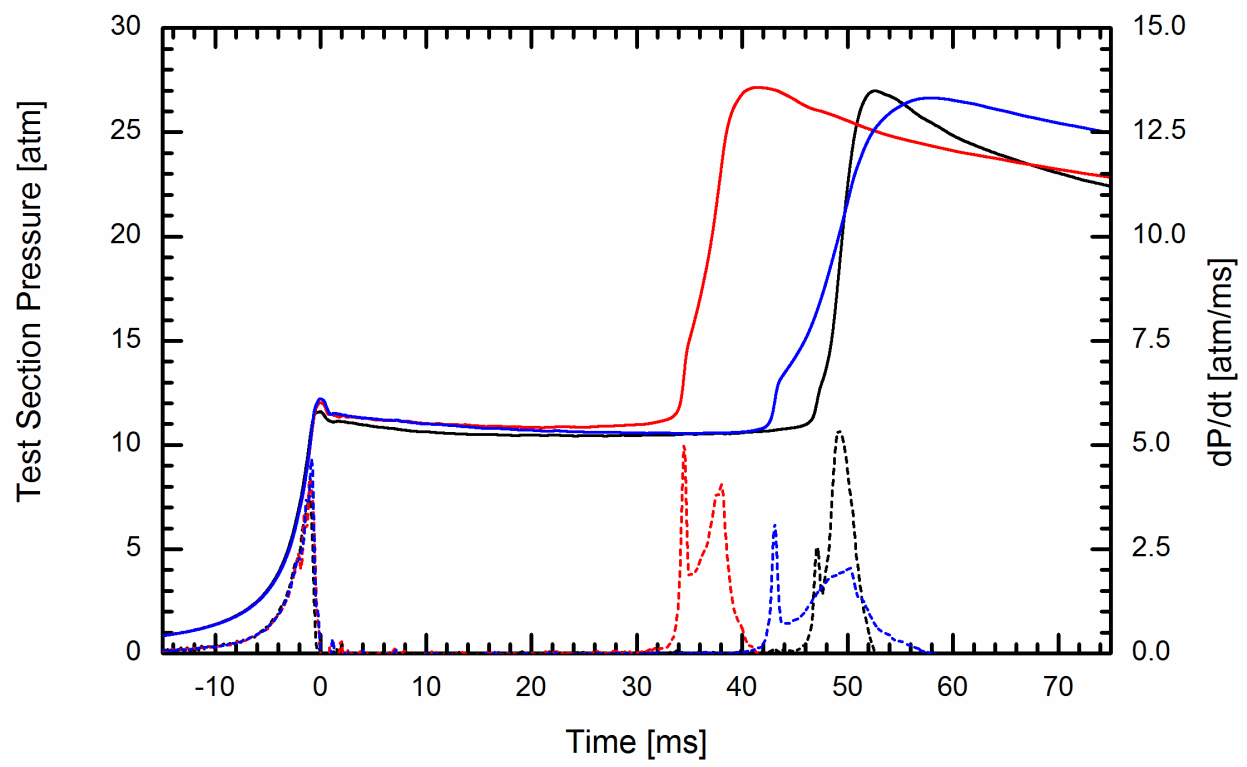

Figure C-1. Pessure and pressure derivative time histories for the three linear hexene isomers at the onset of non-Arrhenius conditions. Experimental conditions for all three isomers are ϕ = 1.0, buffer gas:O2 = 7.5. 1-hexene (black lines): P_{eff} = 10.8 atm, T_{eff} = 847 K, τ_{ign} = 49.2 ms. *trans*-2-hexene (red lines): P_{eff} = 11.1 atm, T_{eff} = 849 K, τ_{ign} = 34.5 ms. *trans*-3-hexene (blue lines): P_{eff} = 10.8 atm, T_{eff} = 844 K, τ_{ign} = 43.1 ms.

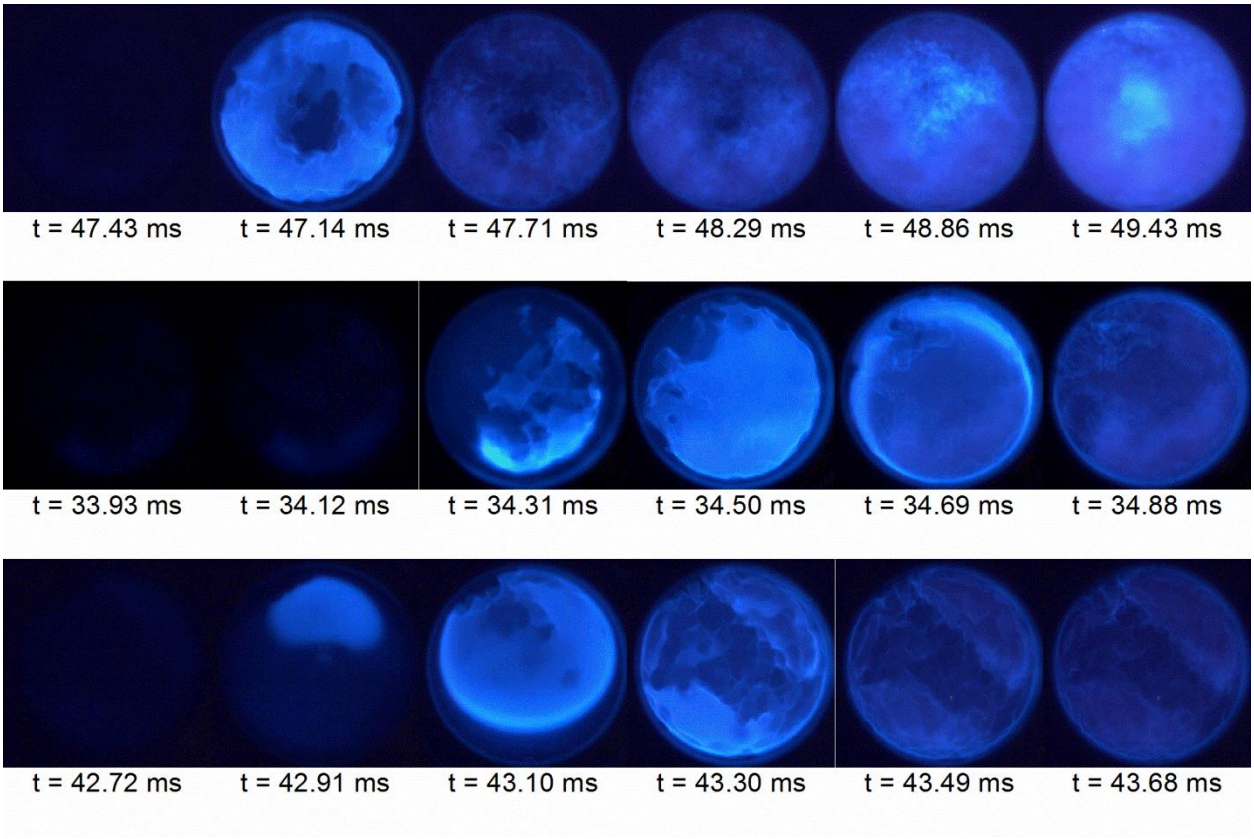

Figure C-2. Still images from the high speed imaging of the UM RCF experiments presented in Figure C-1. Row 1, 1-hexene. Row 2, *trans*-2-hexene. Row 3, *trans*-3-hexene.

Table C-4. Summary of liquids/gases, species purities, and suppliers used during calibrations for the gas chromatography analysis.

Name	Species	Purity	Supplier
nitrogen	N_2	99.999%	Cryogenic Gases
oxygen	O_2	99.994%	Cryogenic Gases
carbon dioxide	CO_2	99.995%	Cryogenic Gases
1-hexene	1-C_6H_{12}	≥99%	Sigma Aldrich
trans-2-hexene	2-C_6H_{12}	97%	Sigma Aldrich
trans-3-hexene	3-C_6H_{12}	≥99%	Sigma Aldrich
hydrogen	H_2	99.99%	Cryogenic Gases
carbon monoxide	CO	99.99%	Cryogenic Gases
methane	CH_4	99.99%	Cryogenic Gases
methanol	CH_3OH	≥99.9%	Sigma Aldrich
ethane	C_2H_6	99.0%	Cryogenic Gases
ethene	C_2H_4	99.5%	Cryogenic Gases
ethyne	C_2H_2	99.6%	Cryogenic Gases
ethanol	C_2H_5OH	≥99.9%	Decon Labs, Inc.
ethanal	CH_3CHO	98.5%	Alfa Aesar
propane	C_3H_8	99.5%	Cryogenic Gases
propene	C_3H_6	99.5%	Cryogenic Gases
propanal	C_2H_5CHO	> 95%	TCI America
1-butene	1-C_4H_8	99.0%	Cryogenic Gases
trans-2-butene	2-C_4H_8	≥99%[a]	Sigma Aldrich
cis-2-butene	2-C_4H_8	≥99%[a]	Sigma Aldrich
1,3-butadiene	1,3-C_4H_6	99.0%	Cryogenic Gases
1-pentene	1-C_5H_{10}	≥98.5%	Sigma Aldrich
trans-2-pentene	2-C_5H_{10}	≥99%[b]	Sigma Aldrich
cis-2-pentene	2-C_5H_{10}	≥99%[b]	Sigma Aldrich
trans-1,3-pentadiene	1,3-C_5H_8	>95%	TCI America
1,4-pentadiene	1,4-C_5H_8	99%	Sigma Aldrich
pentanal	C_4H_9CHO	97%	Sigma Aldrich
1,5-hexadiene	1,5-C_6H_{10}	98%	Alfa Aesar

[a] Mixture of *trans*-2-butene and *cis*-2-butene

[b] Mixture of *trans*-2-pentene and *cis*-2-pentene

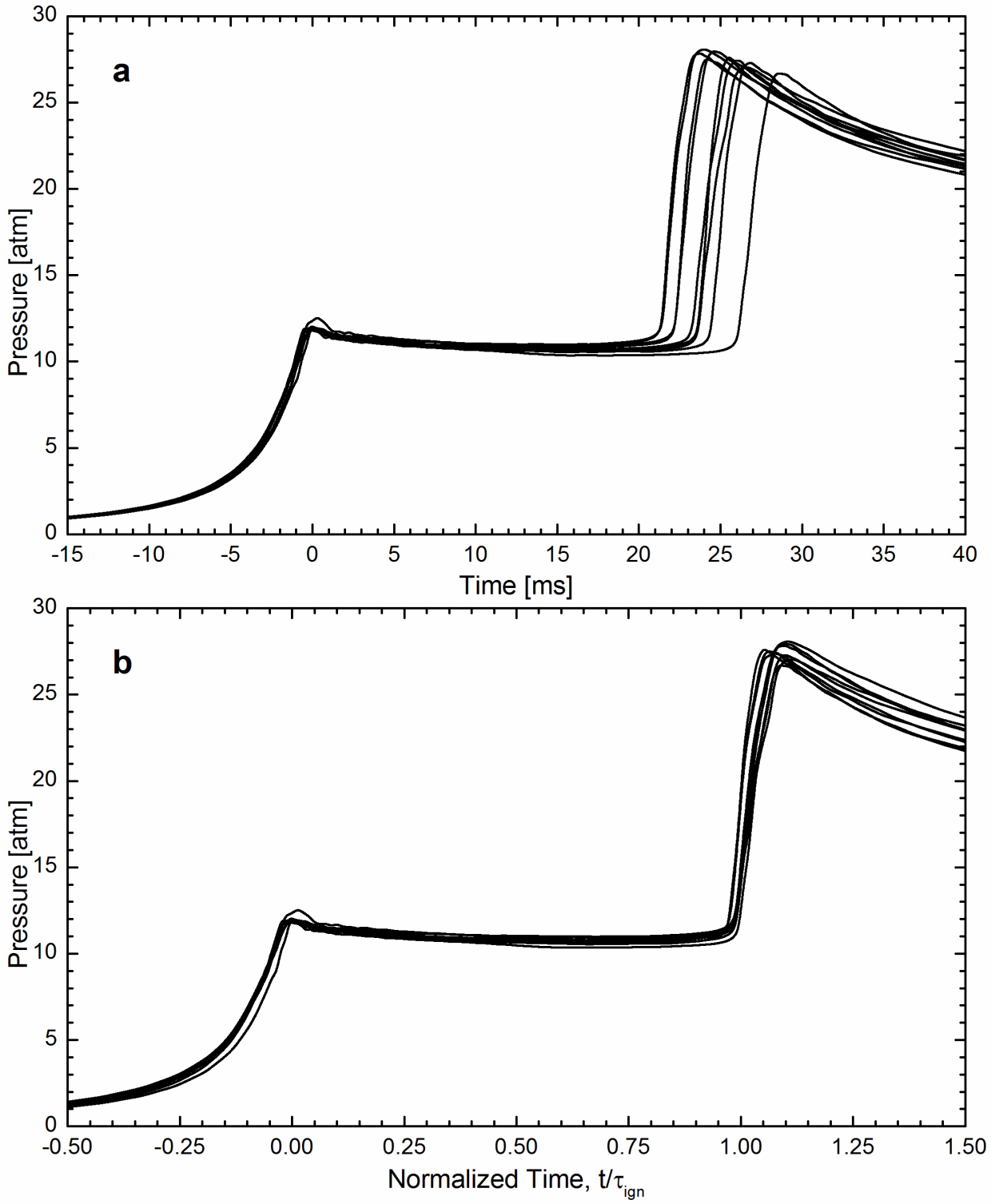

Figure C-3. (a) Pressure time histories for UM RCF speciation experiments of 1-hexene at conditions of ϕ = 1.0, buffer gas:O_2 = 7.5, P_{eff} = 11.1±0.2 atm, T_{eff} = 896±3 K. (b) Normalized pressure time histories, EOC = 0 and τ_{ign} = 1.

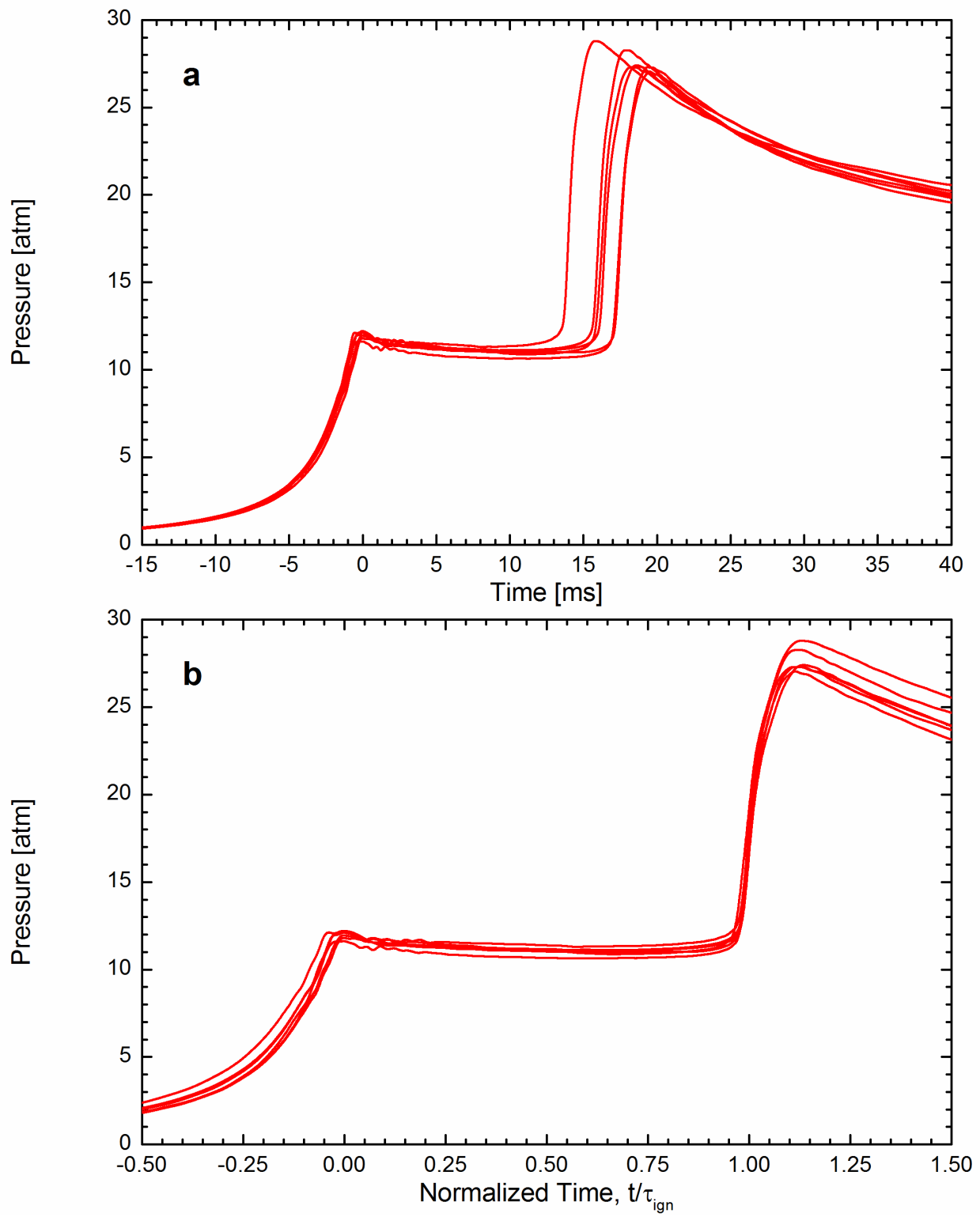

Figure C-4. (a) Pressure time histories for UM RCF speciation experiments of *trans*-2-hexene at conditions of ϕ = 1.0, buffer gas:O_2 = 7.5, P_{eff} = 11.3±0.2 atm, T_{eff} = 905±4 K. (b) Normalized pressure time histories, EOC = 0 and τ_{ign} = 1.

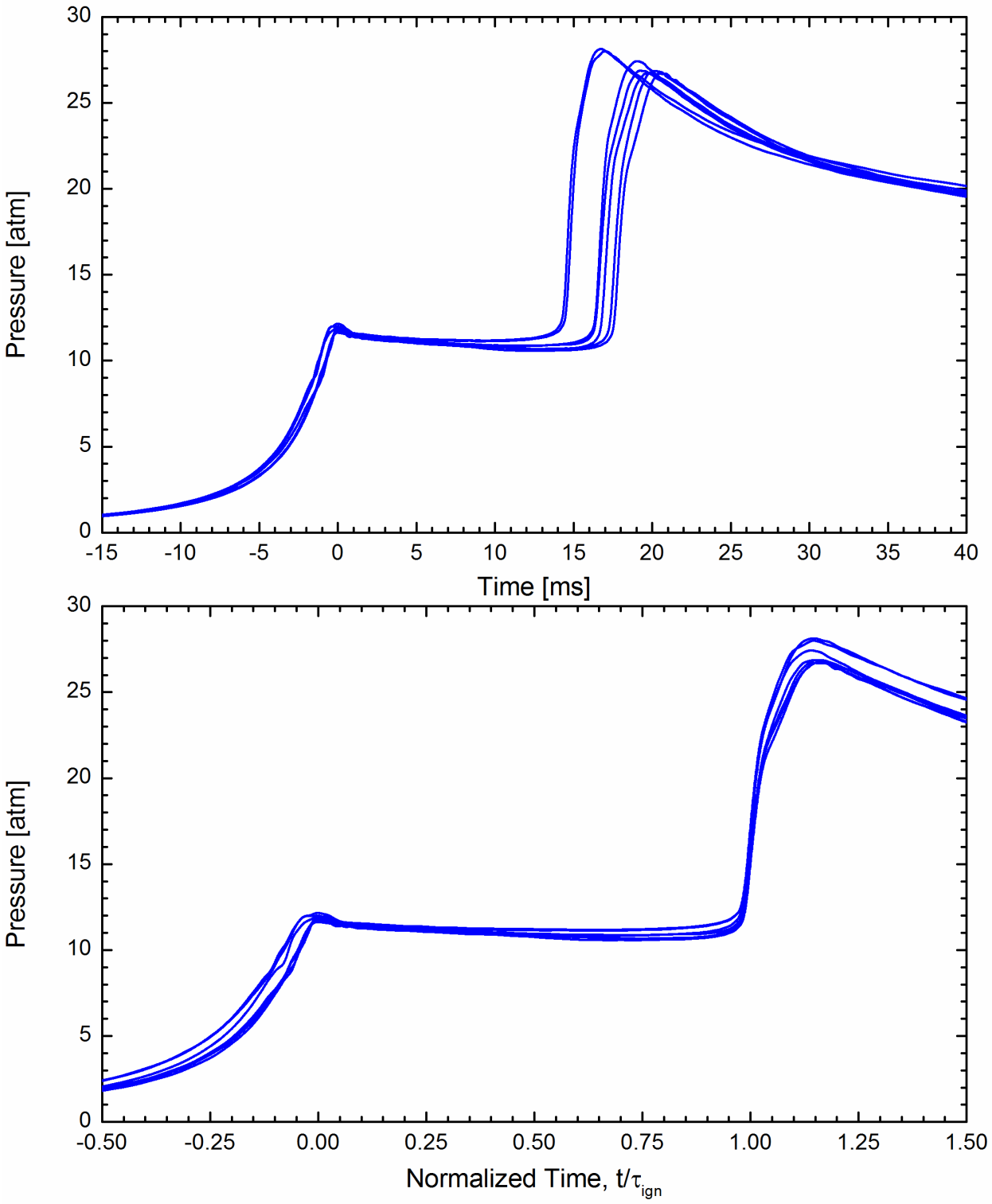

Figure C-5. (a) Pressure time histories for UM RCF speciation experiments of *trans*-3-hexene at conditions of ϕ = 1.0, buffer gas:O_2 = 7.5, P_{eff} = 11.2±0.2 atm, T_{eff} = 899±4 K. (b) Normalized pressure time histories, EOC = 0 and τ_{ign} = 1.

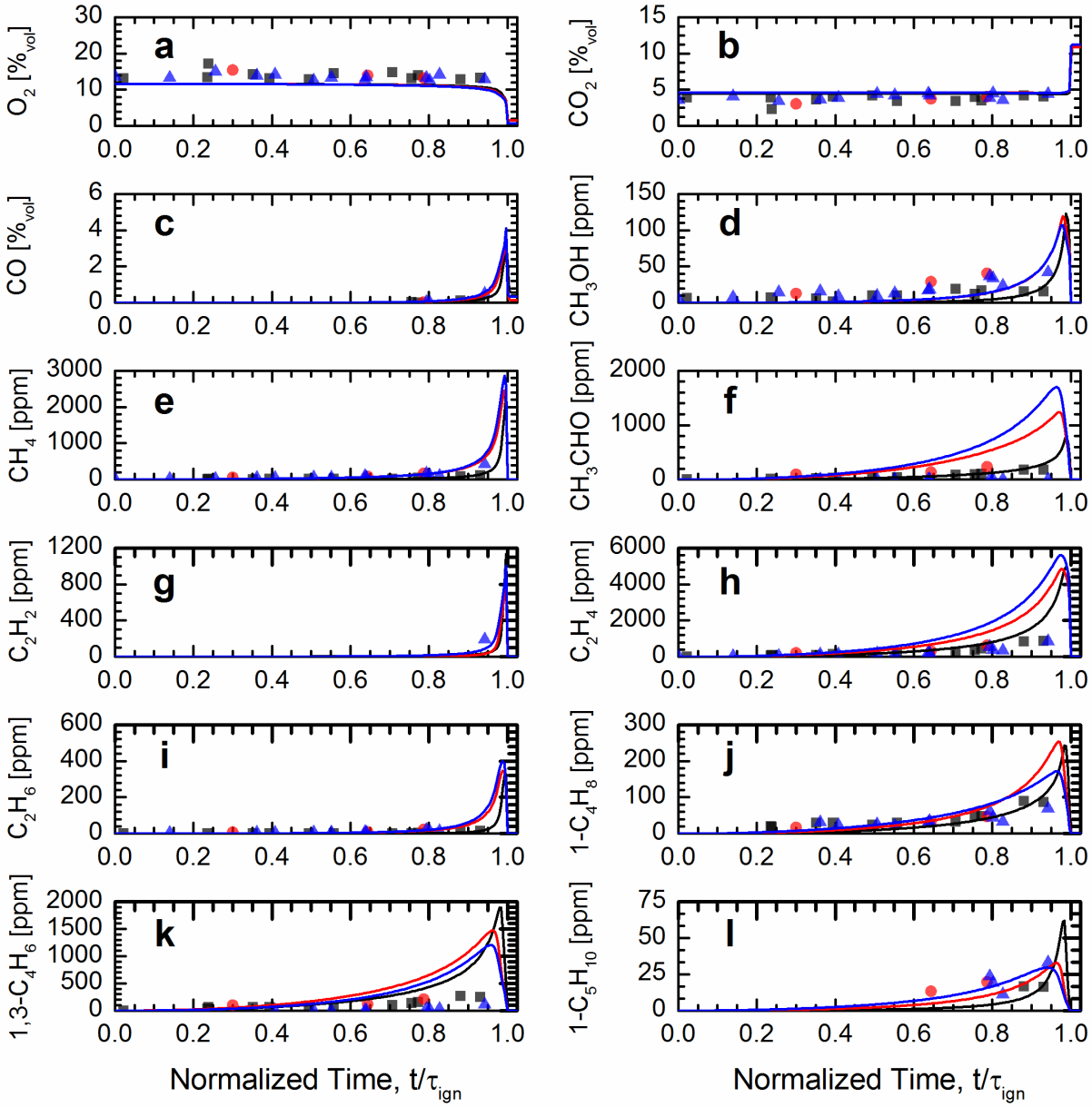

Figure C-6. Stable intermediate time histories (mole fraction) during hexene autoignition: a) O_2, b) CO_2, c) CO, d) CH_3OH, e) CH_4, f) CH_3CHO, g) C_2H_2, h) C_2H_4, i) C_2H_6 j) 1-C_4H_8 k) 1,3-C_4H_6 l) 1-C_5H_{10}. Experimental results of the current work are represented as symbols (black denotes 1-hexene, red denotes *trans*-2-hexene, blue denotes *trans*-3-hexene) and the solid lines are the results from the simulations with the Mehl et al. [92] mechanism.

Bibliography

[1] U.S. Energy Information Administration, Annual Energy Outlook, April 2013.

[2] U.S. Energy Information Administration, International Energy Outlook, July 2013.

[3] Clean Air Act of 1970, 42 USC 7401, December 1970.

[4] Kyoto Protocol to the United Nations Framework Convention on Climate Change, December 1997.

[5] J. Hill, E. Nelson, D. Tillman, S. Polasky, D. Tiffany, Proc. Natl. Acad. Sci. U.S.A 103 (2006) 11206-11210.

[6] A. Haines, A.J. McMichael, K.R. Smith, I. Roberts, J. Woodcock, A. Markandya, B.G. Armstrong, D. Campbell-Lendrum, A.D. Dangour, M. Davies, N. Bruce, C. Tonne, M. Barrett, P. Wilkinson, Lancet 374 (2010) 2104-2114.

[7] R. Warren, J. VanDerWal, J. Price, J.A. Welbergen, I. Atkinson, J. Ramirez-Villegas, T.J. Osborn, A. Jarvis, L.P. Shoo, S.E. Williams, J. Lowe, Nature Clim. Change 3 (2013) 678-682.

[8] A. Starikovsky, N. Aleksandrov, Prog. Energy Combust. Sci. 39 (2013) 61-110.

[9] M.P.B. Musculus, P.C. Miles, L.M. Pickett, Prog. Energy Combust. Sci. 39 (2013) 246-283.

[10] C.K. Westbrook, Annu. Rev. Phys. Chem. 64 (2013) 201-219.

[11] G. Knothe, Prog. Energy Combust. Sci. 36 (2010) 364-373.

[12] S. Blakely, L. Rye, C.W. Wilson, Proc. Combust. Inst. 33 (2011) 2863-2885.

[13] J. Zádor, C.A. Taatjes, R.X. Fernandes, Prog. Energy Combust. Sci. 37 (2011) 371-421.

[14] D.C. Horning, D.F. Davidson, R.K. Hanson, J. Propul. Power 18 (2002) 363-371.

[15] N. Ladommatos, S.M. Abdelhalim, H. Zhao, Z. Hu, Proc. Inst. Mech. Eng. 212 (1998) 25-42.

[16] M. Sjöberg, J.E. Dec, W. Hwang, SAE Technical Paper 2007-01-0207, 2007.

[17] H. Machrafi, S. Cavadias, P. Guibert, Combust. Flame 155 (2008) 476-489.

[18] K. Al-Qurashi, A.D. Lueking, A.L. Boehman, Combust. Flame 158 (2011) 1696-1704.

[19] M. Sjöberg, J.E. Dec, Proc. Combust. Inst. 33 (2011) 3031-3038.

[20] D.F. Davidson, R.K. Hanson, Int. J. Chem. Kinet. 36 (2004) 510-523.

[21] J. Würmel, E.J. Silke, H.J. Curran, M.S. Ó Conaire, J.M. Simmie, Combust. Flame 151 (2007) 289-302.

[22] J. Würmel, J.M. Simmie, H.J. Curran, Int. J. Vehicle Des. 44 (2007) 84-106.

[23] H.S. Shen, J. Vanderover, M.A. Oehlschlaeger, Combust. Flame 155 (2008) 739-755.

[24] S.W. Wagnon, M.S. Wooldridge, Combust. Flame 161 (2014) 898-907.

[25] O. Herbinet, W.J. Pitz, C.K. Westbrook, Combust. Flame 154 (2008) 507–528.

[26] O. Herbinet, W.J. Pitz, C.K. Westbrook, Combust. Flame 157 (2010) 893-908.

[27] S.K. Hoekman, A. Broch, C. Robbins, E. Ceniceros, M. Natarajan, Renew. Sus. Energy Rev. 16 (2012) 143-169.

[28] E.M. Fisher, W.J. Pitz, H.J. Curran, C.K. Westbrook, Proc. Combust. Inst. 28 (2000) 1579-1586.

[29] S.M. Walton, M.S. Wooldridge, C.K. Westbrook, Proc. Combust. Inst. 32 (2009) 255-262.

[30] B.I. Parsons, C.J. Hinshelwood, J. Chem. Soc. (1956) 1799-1803.

[31] D.E. Hoare, L. Ting-Man, A.D. Walsh, Proc. Combust. Inst. 11 (1967) 879-887.

[32] S. Gaïl, M.J. Thomson, S.M. Sarathy, S.A. Syed, P. Dagaut, P. Diévart, A.J. Marchese, F.L. Dryer, Proc. Combust. Inst. 31 (2007) 305-311.

[33] S. Gaïl, S.M. Sarathy, M.J. Thomson, P. Diévart, P. Dagaut, Combust. Flame 155 (2008) 635-650.

[34] S.M. Sarathy, S. Gaïl, S.A. Syed, M.J. Thomson, P. Dagaut, Proc. Combust. Inst. 31 (2007) 1015-1022.

[35] W.K. Metcalfe, S. Dooley, H.J. Curran, J.M. Simmie, A.M. El-Nahas, M.V. Navarro, J. Phys. Chem. A 111 (2007) 4001-4014.

[36] A. Farooq, D.F. Davidson, R.K. Hanson, L.K. Huynh, A. Violi, Proc. Combust. Inst. 32 (2009) 247-253.

[37] S. Dooley, H.J. Curran, J.M. Simmie, Combust. Flame 153 (2008) 2-32.

[38] M.H. Hakka, H. Bennadji, J. Biet, M. Yahyaoui, B. Sirjean, V. Warth, L. Coniglio, O. Herbinet, P.A. Glaude, F. Billaud, F. Battin-Leclerc, Int. J. Chem. Kin. 42 (2010) 226-252.

[39] B. Akih-Kumgeh, J.M. Bergthorson, Energy Fuels 24 (2010) 2439-2448.

[40] K. Hadjali, M. Crochet, G. Vanhove, M. Ribaucour, R. Minetti, Proc. Combust. Inst. 32 (2009) 239-246.

[41] A. Osmont, M. Yahyaoui, L. Catoire, I. Gökalp, M.T. Swihart, Combust. Flame 155 (2008) 334-342.

[42] A.M. El-Nahas, M.V. Navarro, J.M. Simmie, J.W. Bozzelli, H.J. Curran, S. Dooley, W. Metcalfe, J. Phys. Chem. A 111 (2007) 3727-3739.

[43] L.K. Huynh, K.C. Lin, A. Violi, J. Phys. Chem. A 112 (2008) 13470-13480.

[44] L.K. Huynh, A. Violi, J. Org. Chem. 73 (2008) 94-101.

[45] C.J. Hayes, D.R. Burgess Jr., Proc. Combust. Inst. 32 (2009) 263-270.

[46] S.M. Walton, D.M. Karwat, P.D. Teini, A.M. Gorny, M.S. Wooldridge, Fuel 90 (2011) 1796-1804.

[47] C.K. Lin, J. Y. W. Lai, A. Violi, Fuel 92 (2012) 16-26.

[48] G. Dayma, S. Gaïl, P. Dagaut, Energy & Fuels 22 (2008) 1469-1479.

[49] G. Dayma, C. Togbé, P. Dagaut, Energy & Fuels 23 (2009) 4254-4268.

[50] P.A. Glaude, O. Herbinet, S. Bax, J. Biet, V. Warth, F. Battin-Leclerc, Combust. Flame 157 (2010) 2035-2050.

[51] M.H. Hakka, P.A. Glaude, O. Herbinet, F. Battin-Leclerc, Combust. Flame 156 (2009) 2129-2144.

[52] W. Wang, S. Gowdagiri, M.A. Oehlschlaeger, Energy & Fuels 27 (2013) 5527-5532.

[53] S. Bax, M.H. Hakka, P.A. Glaude, O. Herbinet, F. Battin-Leclerc, Combust. Flame, 157 (2010) 1220–1229.

[54] C.K. Westbrook, C.V. Naik, O. Herbinet, W.J. Pitz, M. Mehl, S.M. Sarathy, H.J. Curran, Combust. Flame 158 (2011) 742-755.

[55] K. Zhang, C. Togbé, G. Dayma, P. Dagaut, Combust. Flame 161 (2014) 818-825.

[56] S.W. Wagnon, D.M.A. Karwat, M.S. Wooldridge, C.K. Westbrook, "On the Ignition Chemistry of Methyl *trans*-3-hexenoate," submitted to Fuel, June 2014.

[57] B. Shukla, A. Susa, A. Miyoshi, M. Koshi, J. Phys. Chem A 112 (2008) 2362-2369.

[58] B. Shukla, M. Koshi, Combust. Flame 158 (2011) 369-375.

[59] A. Comandini, T. Malewicki, K. Brezinsky, J. Phys. Chem. A 116 (2012) 2409-2434.

[60] R.S. Tranter, S.J. Klippenstein, L.B. Harding, B.R. Giri, X. Yang, J.H. Kiefer, J. Phys. Chem A 114 (2010) 8240-8261.

[61] S.H. Dürrstein, M. Olzmann, J. Aguilera-Iparraguirre, R. Barthel, W. Klopper, Chem. Phys. Lett. 513 (2011) 20-26.

[62] P. Frank, J. Herzler, Th. Just, C. Wahl, Proc. Combust. Inst. 25 (1994) 833-840.

[63] T. Yu, M.C. Lin, J. Am. Chem. Soc. 116 (1994) 9571-9576.

[64] S.S. Kumaran, J.V. Michael, "Phenyl Radical Thermolysis and Rate Constants for Phenyl + O_2" Int. Symp. Shock Waves 21 (1997).

[65] P.H. Cribb, J.E. Dove, S. Yamazaki, Combust. Flame 88 (1992) 186-200.

[66] S.W. Wagnon, K.Y. Lam, C.J. Annesley, R.S. Tranter, "A Shock Tube Investigation of Phenyl + O_2," manuscript in preparation.

[67] F. Battin-Leclerc, Prog. Energy Combust. Sci. 34 (2008), 440–498.

[68] P. Dagaut, M. Cathonnet, Prog. Energy Combust. Sci. 32 (2006), 48–92.

[69] W.J. Pitz, C.J. Mueller, Prog. Energy Combust. Sci. 37 (2011), 330–350.

[70] L. Coniglio, H. Bennadji, P.A. Glaude, O. Herbinet, F. Billaud, Prog. Energy Combust. Sci. 39 (2013), 340–382.

[71] B. Heyberger, N. Belmekki, V. Conraud, P.A. Glaude, R. Fournet, F. Battin-Leclerc, Int. J. Chem. Kinet. 34 (2002) 666-677.

[72] S. Saxena, M.S.P. Kahandawala, S.S. Sidhu, Combust. Flame 158 (2011) 1019-1031.

[73] Z. Qin, H. Yang, W.C. Gardiner, Combust. Flame 124 (2001) 246-254.

[74] C. Saggese, A. Frassoldati, A. Cuoci, T. Faravelli, E. Ranzi, Combust. Flame 160 (2013) 1168-1190.

[75] W.K. Metcalfe, S. Dooley, F.L. Dryer, Energy & Fuels 25 (2011) 4915-4936.

[76] G. Vanhove, M. Ribaucour, R. Minetti, Proc. Combust. Inst. 30 (2005) 1065-1072.

[77] M. Mehl, G. Vanhove, W.J. Pitz, E. Ranzi, Combust. Flame 155 (2008) 756-772.

[78] M. Yayaoui, N. Debaili-Chaumeix, C.-E. Paillard, S. Touchard, R. Fournet, P.A. Glaude, F. Battin-Leclerc, Proc. Combust. Inst. 30 (2005) 1137-1145.

[79] M. Yahyaoui, N. Debaili-Chaumeix, P. Dagaut, C.-E. Paillard, S. Gail, Combust. Flame 147 (2006) 67-78.

[80] R. Bounaceur, V. Warth, B. Sirjean, P.A. Glaude, R. Fournet, F. Battin-Leclerc, Proc. Combust. Inst. 32 (2009) 387-394.

[81] S. Tanaka, F. Ayala, J.C. Keck, J.B. Heywood, Combust. Flame 132 (2003) 219-239.

[82] M. Mehl, W.J. Pitz, C.K. Westbrook, K. Yasunaga, C. Conroy, H.J. Curran, Proc. Combust. Inst. 33 (2011) 201–208.

[83] S.W. Wagnon, M.S. Wooldridge, "Autoignition and Speciation Studies of *trans*-Hexene Isomers in a Rapid Compression Facility," manuscript in preparation.

[84] M.T. Donovan, X. He, B.T. Zigler, T.R. Palmer, M.S. Wooldridge, A. Atreya, Combust. Flame 137 (2004) 351-365.

[85] S.W. Walton, X. He, B.T. Zigler, M.S. Wooldridge, A. Atreya, Combust. Flame 150 (2007) 246-262.

[86] D.M.A. Karwat, S.W. Wagnon, M.S. Wooldridge, C.K. Westbrook, Combust. Flame 160 (2013) 2693-2706.

[87] R.S. Tranter, B.R. Giri, Rev. Sci. Instrum. 79 (2008) 094103.

[88] P.T. Lynch, C.J. Annesley, C.J. Aul, X. Yang, R.S. Tranter, J. Phys. Chem. A 117 (2013) 4750-4761.

[89] J.H. Kiefer, The Laser Schlieren Technique in Shock Tube Kinetics, Shock Waves in Chemistry (1981) 219-277.

[90] J.H. Kiefer, M.Z. Al-Alami, J-C. Hajduk, Appl.Opt. 20 (1981) 221-230.

[91] Reaction Design CHEMKIN Release 10113 (x64), 2012.

[92] M. Mehl, W.J. Pitz, C.K. Westbrook, H.J. Curran, Proc. Combust. Inst. 33 (2011) 193-200.

[93] G. Black, H.J. Curran, S. Pichon, J.M. Simmie, V. Zhukov, Combust. Flame 157 (2010) 363-373.

[94] H.J. Curran, P. Gaffuri, W.J. Pitz, C.K. Westbrook, Combust. Flame 129 (2002) 253-280.

[95] H.J. Curran, P. Gaffuri, W.J. Pitz, C.K. Westbrook, Combust. Flame 114 (1998) 149-177.

[96] C.J. Aul, W.K. Metcalfe, S.M. Burke, H.J. Curran, E.L. Petersen, Combust. Flame 160 (2013) 1153-1167.

[97] P. Dagaut, S.M. Sarathy, M.J. Thomson, Proc. Combust. Inst. 32 (2009) 229-237.

[98] N. Donato, C. Zinner, H. Curran, G. Bourque, C. Aul, E. Petersen, J. Eng. Gas Turbines Power 132 (2010) 051502 p1-9.

[99] S.M. Villano, L.K. Huynh, H.H. Carstensen, A.M. Dean, J. Phys. Chem. A 115 (2011) 13425–13442.

[100] S.M. Villano, L.K. Huynh, H.H. Carstensen, A.M. Dean, J. Phys. Chem. A 116 (2012) 5068–5089.

[101] X. He, M.T. Donovan, B.T. Zigler, T.R. Palmer, S.M. Walton, M.S. Wooldridge, A. Atreya, Combust. Flame 142 (2005) 266–275.

[102] X. He, B.T. Zigler, S.M. Walton, M.S. Wooldridge, A. Atreya, Combust. Flame 145 (2006) 552–570.

[103] D.M.A. Karwat, S.W. Wagnon, P.D. Teini, M.S. Wooldridge, J. Phys. Chem. A 115 (2011) 4909–4921.

[104] H.K. Ciezki, G. Adomeit, Combust. Flame 93 (1993) 421–433.

[105] D.F. Davidson, D.R. Haylett, R.K. Hanson, Combust. Flame 155 (2008) 108–117.

[106] A.K. Oppenheim, Philos. Trans. R. Soc. Lond. Ser. A 315 (1985) 471–508.

[107] S.M. Walton, X. He, B.T. Zigler, M.S. Wooldridge, Proc. Combust. Inst. 31 (2007) 3147–3154.

[108] A.B. Mansfield, M.S. Wooldridge, Combust. Flame (2014) "High-pressure Low Temperature Ignition Behavior of Syngas Mixtures" in press DOI: 10.1016/j.combustflame.2014.03.001.

[109] A.G. Gaydon, The Spectroscopy of Flames, Wiley, New York, 1957.

[110] B.J. McBride, S. Gordon, M.A. Reno, Thermodynamic Data Base, NASA Technical Memorandum 4513, 1993.

[111] S.M. Walton, Ph.D. Dissertation, 2008, "Experimental Investigation of the Auto-Ignition Characteristics of Oxygenated Reference Fuel Compounds," University of Michigan.

[112] W. Gardiner, Y. Hidaka, T. Tanzawa, Combust. Flame 40 (1981) 213-219.

[113] K.P. Birch, J. Opt. Soc. Am. A 8 (1991) 647-651.

[114] R. Sivaramakrishnan, personal communication, November 6, 2013.

[115] J.V. Michael, Prog. Energy Combust. Sci. 18 (1992) 327-347.

[116] L.V. Moskaleva, M.C. Lin, J. Comp. Chem. 21 (2000) 415-425.

[117] E. Goos, A. Burcat, B. Ruscic, "Extended Third Millenium Ideal Gas Thermochemical Database with Updates from Active Thermochemical Tables," <http://burcat.technion.ac.il/dir> mirrored at <http://garfield.chem.elte.hu/Burcat/burcat.html>; accessed November 13, 2013.

[118] W. Gardiner, B. Walker, C. Wakefield, "Mathematical Methods for Modeling Chemical Reactions in Shock Waves," in Shock Waves in Chemistry, A. Lifshitz, ed. M. Dekker: New York, 1981.

[119] J. Wurmel, E.J. Silke, H.J. Curran, M.S. O Conaire, J.M. Simmie, Combust. Flame 151 (2007) 289-302.